Time-lapse techniques for surface velocity, front position and calving rate measurement of a fast-flowing tidewater glacier in Svalbard

Master of Science Thesis
Quaternary Geology and Palaeoclimatology

Department of Earth Science
University of Bergen

Department of Arctic Geology
University Centre in Svalbard

Silje Smith-Johnsen

May 2015

Abstract

Calving is the mechanical loss of icebergs from tidewater glaciers, responsible for 70% of the annual transfer of mass from the cryosphere to the ocean (van der Veen 1998a, 2002). To be able to correctly predict future global sea level changes it is important to understand calving processes and incorporate them into the models.

The aim of this thesis is to investigate surface velocities, front positions and calving rates of a fast flowing tidewater glacier in Svalbard using an automatic oblique terrestrial time-lapse camera. The camera took pictures every 30 min from May 1st to September 16th 2014 resulting in 6600 images. The project forms part of the ConocoPhillips-Lundin Northern Area Program project CRIOS (Calving Rates and Impact on Sea Level) program whose overall aim is to develop better calving-process models.

Mean velocities of Kronebreen increased from 3 m/day in May and reached a peak in mid-July of 5.3 m/day, with a velocity pattern showing increasing velocities towards the front and the centreline. Velocity results were filtered, sensitivity tested, averaged both spatially and temporally and fit well with previous results. Results suggest that velocity has a forcing from air temperature and rain events due to water inputs in the glacier system.

Mean front positions showed a total retreat of 320 m, and calving rates reached a peak in early August of 11 m/day. Different parts of the front showed different styles of retreat, and therefore calving styles. Inter-meltwater-plume areas were dominated by infrequent large calving events, and plume areas were dominated by continuous calving. Mean calving rates may be atmospherically controlled, but internal dynamics, melt-water plumes and fjord temperatures may also play a role.

The high resolution both spatially and temporally gained using this method makes it possible to investigate the nature of calving and the evolution of surface velocity patterns in more detail than satellite derived results. These data are required for improving the understanding of calving dynamics to develop sea level rise models.

Acknowledgements

This thesis forms part of the CRIOS (Calving Rates and Impact on Sea level) project funded by The ConocoPhillips Lundin Northern Area Program. I would like to thank Professor Doug Benn at the Arctic Geology department at UNIS for letting me join his project, and for supervising me through my master programme. I also appreciated his invitation to the CASS (Calving and Surging Glaciers in Svalbard) workshop in Utrecht funded by Svalbard Science Forum. Thanks to Heidi Sevestre, Penelope How and Dr Nick Hulton for the best fieldwork in Ny Ålesund. Particularly thanks to Dr Nick Hulton and Penelope How for teaching me everything and helping me on every step of the way, and for good times in both Edinburgh and the IGS conference in Iceland. I would like to thank my other supervisor Professor Atle Nesje at Department of Earth Science at University of Bergen for helping me, and for a fantastic excursion across Norway. Thanks to Professor Adrian Luckman from the Glaciology Group, Swansea University for access to his TerraSAR-X results. Thanks to Alexandra Messerli and Aslak Grinsted at Centre for Ice and Climate, Niels Bohr Institute, University of Copenhagen for a helpful toolbox. In addition, I would like to thank the Jan Christensen Scholarship for financial support when living in Longyearbyen.

I would especially like to thank my family for supporting my glaciologist dream since I was 13 years old. Tusen takk Pappa for at du reddet meg i siste liten! Thanks to Ingunn Farsund, the best roommate and office buddy, for always being there for me! Thanks to Alexander Hovland for entertainment at UNIS, Spitra and Sletten. Thanks to the masterstudent group for cabin trips and coffee breaks. Thanks to Chris Borstad for nice trips and MATLAB help. Thanks to the handymen at logistics for great times at work and the pub. Most of all, thanks to the good old guide group in Longyearbyen, for constantly reminding me that there is a world outside UNIS. Lastly, I would like to thank 'Stålpuzen' for all the adventures during our 4 fantastic winters together in the wild.

Silje S Johnsen

Longyearbyen, May 2015

Table of contents

1 Introduction

Sea level rise is a potentially damaging effect of climate change; it can submerge low-lying populated coastal areas and pollute coastal groundwaters (Benn and Evans 2010). The Greenland ice sheet has a volume of 2.60 million km^3, equivalent to a global sea level rise of 6.5m. An ice loss rate from the period 2002-2011 of 215 Gt /year is equivalent to a global sea level rise of 0.59 mm/year (IPCC 2013).

Four huge fast–flowing marine-terminating outlet glaciers named Petermann, Jakobshavn, Kangerdlugssuaq and Helheim Glaciers, drain 22 percent of the Greenland ice sheet collectively (Nick et al. 2013). A contribution to sea level rise from these outlet glaciers in a mid-range future warming scenario, is calculated to be between 19 and 30 mm by year 2200 (Nick et al. 2013).

The late Quaternary Svalbard-Barents Sea Ice sheet was largely marine-based, and it has been suggested that the collapse was due to sea level rise that in turn led to large scale calving. Thus in order to both predict the future of present ice sheets, and to understand past behaviour, it is important to understand the dynamic interactions between ocean systems and glacial systems (Ingólfsson and Landvik 2013).

Calving is the mechanical loss of icebergs from tidewater glaciers, an important though not well understood ablation process, responsible for 70% of the annual transfer of mass from the cryosphere to the ocean (van der Veen 1998a, 2002). All calving events occur when tensile stresses close to glacier margin are large enough to propagate fractures through the ice (Benn and Evans 2010). The size of ice blocks detached range from small bits and pieces to large tabular ice bergs (van der Veen 2013), the breakup of Larsen B ice shelf from the Antarctic Peninsula (Rignot et al. 2004) and a huge calving event at Petermann glacier in Greenland in 2012 are two extreme examples.

Introduction

The Fifth Assessment report from the International Panel on Climate Change (IPCC) stresses the fact that mass loss from iceberg calving is not yet comprehensively assessed. Even though the spatio-temporal distribution of flow on fast-flowing Arctic glaciers is important in determining the reaction of these glaciers to climate changes, the knowledge about them is still limited, particularly when the glaciers are calving (Kääb et al. 2005).

To be able to correctly predict future global sea level changes it is important to understand calving processes and incorporate them into the models. van der Veen (2013) finishes the chapter about fractures with the clear message: "…the lack of fundamental understanding of the calving process should be of concern to the glaciological community". Sundal (2013) stresses the importance of high spatial and temporal resolution observations of ice flow and calving-front positions as a validation of modelling results and to capture rapid dynamic changes.

As a way of better comprehending glacier and calving both ice velocity and front positions of glaciers have been measured using terrestrial time-lapse photogrammetry in the past (Ahn and Box 2010; Eiken and Sund 2012; T. D. James et al. 2014; R.M. Krimmel and Rasmussen 1986; O'Neel et al. 2003; Sund et al. 2011), but only for short periods of time (1-2months) and with a temporal resolution of max 2h interval. O'Neel et al. (2003) highlight that the focus on calving rates has mainly been directed towards annual time-scales (e.g. Brown et al. 1982; Meier and Post, 1987; Van der Veen, 1996), with less attention given to seasonal changes. Luckman et al. (in review) found a strong correlation with calving rates and sub-surface sea temperatures, but mention that other factors may have an influence over shorter timescale. This project aims to increase the length of the observation period and the temporal resolution to gain a better and more detailed insight in the nature of calving on a diurnal to seasonal scale.

In this study, the behaviour of the calving front of Kronebreen has been investigated by using high temporal resolution terrestrial time-lapse techniques. Fluctuations in velocity, front positions and calving rates throughout the melt season from May to September 2014 are analysed, and results compared to processed Terra SAR-x/TanDEM-x data to validate

the method. An additional validation will be comparing results from two different terrestrial cameras. The aim of this thesis is to:

- Develop the most suitable automated time-lapse techniques related to glacier observation.
- Calculate ice velocity at the snout area, front position and calving rate of Kronebreen from May-September 2014 on a diurnal to biweekly scale.

Kronebreen in Kongsfjorden in North West Svalbard was chosen as the research area for several reasons (**Figure 1.1**). The location close to the research settlement of Ny Ålesund makes it easily-accessible for logistical support. The glacier is continuously fast flowing (~700m/year (Liestøl 1988)) which makes it an excellent candidate for time-lapse velocity investigations and a good analogue for Greenland outlet glaciers. Due to the risk of travelling on the heavily crevassed glacier front, terrestrial time-lapse photogrammetry is preferred as a safer alternative.

Figure 1.1 *Map of the Svalbard archipelago with the location of Kronebreen and Ny-Ålesund, shown in detail in* **Figure 2.6.**

2 Theoretical Background

2.1 Calving dynamics

Calving is a complex sporadic process and calving glaciers are very diverse. Calving glaciers terminate in a proglacial lake or in the sea, with either floating or grounded margins (Chapuis and Tetzlaff 2014). Calving glaciers terminating in the sea are called tidewater glaciers. The calving process interacts with glacier dynamics and it is necessary to understand subglacial hydrology, basal motion, ice fracture and energy exchanges between the ice and ocean to be able to develop proper general models (Benn and Evans 2010).

2.1.1 Calving processes

Despite the chaotic nature of calving, four scenarios that generate calving can be considered (Benn et al. 2007a):

- Longitudinal stretching associated with large-scale velocity gradients
- Steep stress gradients at ice cliffs or floating ice fronts
- Ice cliff undercutting by melting at or below the waterline
- Bending forces at buoyant glacier margins

Calving glaciers tend to speed up towards the terminus, as the glacier becomes thinner and basal drag is reduced when the front approaches flotation (Benn and Evans 2010; Vieli et al. 2004). This phenomenon stretches the ice, and as transverse crevasses develop and they may propagate through the ice to trigger calving. Meltwater stored in crevasses can cause them to penetrate even deeper than dry crevasses.

At the frontal cliff of calving glaciers there is an imbalance between outward- and inward directed forces, which leads to large stress gradients (Benn et al. 2007a). Cryostatic pressure increases downwards, and the outward component is not supported by

atmospheric pressure. Thus the net outward-directed force is largest at the base of the subaerial ice cliff (Benn and Evans 2010). The subaqueous part of the calving front has some opposing components from the backward-directed hydrostatic forces, but they will always be smaller at a grounded ice front (Benn et al. 2007a).

Thermo-erosional subaqueous undercutting of ice cliffs can develop a notch that induces a force imbalance and leads to collapse of the undercut pillars. This process usually follows seasonal cycles, and ceases when sea ice is present. In addition, the undercutting is dependent on water circulation to transfer the energy (Benn et al. 2007a; Vieli et al. 2002).

If a grounded terminus is subject to surface melting to the degree where it thins to less than the flotation thickness, it becomes subject to net upward buoyant forces and can fracture catastrophically. An ice foot can develop if the subaerial part of the ice cliff is calved off, and which can then shoot up because of the buoyant forces acting on it. O'Leary and Christoffersen (2013) modelled the effect of undercutting on calving, and concluded that water temperatures near the base of the glacier front are likely to have the greatest effect on calving, and not the sea surface temperatures.

Calving rate can be defined as the volume of ice that breaks off per unit time and per unit vertical area at the glacier terminus, and is equal to the difference between glacier velocity at the terminus and glacier length over time:

$$U_c = U_t - \delta L/\delta t \qquad \textbf{Eq. 2.1}$$

Where U_c is calving rate, U_t is the glacier velocity at the terminus, L is glacier length and t is time (Benn and Evans 2010). Calving rate is closely linked to ice velocity at the front, and it is important to have in mind which external factors affect the velocity of calving glaciers. As mentioned, submarine melting can amplify calving, and is an important factor that can be included into the U_c term. A more correct terminology for calving rate would be *frontal ablation rate* (Luckman et al. in review).

Basal drag ceases if the glacier margin thickness is less than a critical floatation thickness, $H_{f,}$ and the glacier can then accelerate:

$$H_f = \frac{pW}{pI} D_w \qquad \textbf{Eq. 2.2}$$

Where pW is density of the water it terminates in, pI is the density of the glacier ice and D_w is water depth (van der Veen 2013). On Columbia Glacier a correlation between velocity fluctuations at the front and tidal cycles has been demonstrated to exist, with the highest velocities occurring at low tide (Robert M. Krimmel and Vaughn 1987; Meier and Post 1987). The subglacial drainage system plays an important part in the velocity, and this can be shown by comparing velocity records with air temperature, ablation rates, rainfall-data and water levels in bore holes (Robert M. Krimmel and Vaughn 1987; Meier et al. 1994; Vieli et al. 2004).

2.1.2 Surveying calving glaciers

O'Neel et al. (2003) used time-lapse photography to determine the position of the terminus of LeConte Glacier on a sub-daily basis. They measured ice motion and terminus position at 2-8 hour intervals nearly continuously between 2 May and 4 June 1999, and by measuring the ice thickness at the front they calculated calving flux. Data from external factors that might affect glacier motion and calving were collected, like tidal data, surface ablation, precipitation and air temperature. In addition, they recorded the timing and magnitude of calving events during the day, using a subjective scale from 1-10. One conclusion was "Neither the visual nor the photogrammetric calving time series show evidence that changes in ice velocity are related to calving events", and "there is little or no correlation between semi-diurnal tidal fluctuations and calving".

As part of the Extreme Ice Survey, Ahn and Box (2010) installed digital cameras by some of the huge outlet glaciers of Western-Greenland. Images were taken from May-June 2007. They had a loss of 15-20% of image data due both internal (timer failure) and external factors (wild animals, poor visibility). Images taken at midday were used to calculate velocity. The offset measurement, displacement, was calculated using area-based image matching, but before this the images are enhanced several different ways, resulting in 5 new images in addition to the original.

James et al. (2014) investigated calving and ice flow velocity by using time lapse techniques at Helheim glacier in 2010 and 2011, both stereoscopically (until power failure) and monoscopically. They developed DEMs from the stereoscopic dataset. The authors discovered a front advance and lifting prior to three major calving events, based on terrestrial photogrammetry without converting pixel values to real world coordinates.

Additionally, remote sensing from satellites is used to monitor glacier velocities and front positions (Kääb et al. 2005). Radar satellite imagery from e.g. the TerraSAR-X is independent of weather conditions and light (dark season in Svalbard), but will have a maximum temporal resolution of 11 days and a spatial resolution of 2m. Many tidewater glaciers in Svalbard are monitored like this, including Kronebreen (**Figure.2.1**) (Luckman et al. in review).

2.1.3 Changes in front positions of calving glaciers

There are several controls on tidewater glacier terminus position, including ice velocity, calving rate, bed topography (Vieli et al. 2001), water depth and ice thickness. The front position of calving glaciers appear to go through cycles of very slow and long-lasting periods of advance, and shorter periods of rapid retreat (Meier and Post 1987), without any obvious climatic control on this (van der Veen 2013; Benn et al. 2007a; Vieli et al. 2001).

2.1.4 Calving rate and velocity relationship

It has long been discussed whether calving loss is the driver of glacier flow acceleration, or *vice versa* (Benn et al. 2007a). On one side, calving can trigger dynamic changes upstream in the glacier which in turn can lead to increased velocities and other dynamic changes (Meier and Post 1987). This makes the calving process the driving force, or the 'master'. On the other side, calving can be regarded as the 'slave', which acts passively to dynamic changes like flow acceleration or thinning (Benn et al. 2007a). Both ideas have support from the comprehensive Columbia Glacier dataset.

Glacier velocity variations in both space and time control the depth of surface crevasses and rates of dynamic thickness change. This means that longitudinal and transverse velocity gradients determine the behaviour of calving glacier meaning they act as a fundamental control on where and when calving occurs, but there is not a straightforward correlation to calving rates (Benn et al. 2007a).

Figure 2.1 *The heavily crevassed surface of Kronebreen*

2.2 Photogrammetry

Measuring glacier velocity from terrestrial photograph sequences was done already in 1983 by Krimmel and Rasmussen (1986) on Columbia glacier, and O'Neel et al. (2003) further improved the method. Time-lapse movies are also a good way to reach out to the public, explaining glacier dynamic and climatic change effects on glaciers in a very visual way (**Figure 2.2**).

Figure 2.2 *Time lapse camera set up on the nunatak Steindolpen looking down at Kronebreen*

2.2.1 Camera structure

Digital single lens reflex cameras (SLR) produce digital images, which consist of an array of *pixels*. The total *image size* is the product of the number of rows and columns in the array, i.e. the number of pixels in the image. For each pixel the camera sensor (Charge Coupled Device or CCD) registers a separate RGB (red green blue) intensity value. These values build up an image that humans can observe. The *sensor size* is the product of the horizontal and vertical length of the sensor in the camera, often measured in mm. The raw size of each pixel on the CCD is calculated by dividing *image size* (pixels) by *sensor size* (mm). *Focal length* is the distance from the optical centre (where the light rays converge) to the sensor in the camera, see **Figure 2.4 B**.

The *principal point* is the perpendicular intersection point of the *principal axis* and the image plane, defined by pixel coordinates. The principal axis is the horizontal line from the camera centre, see **Figure 2.3**.

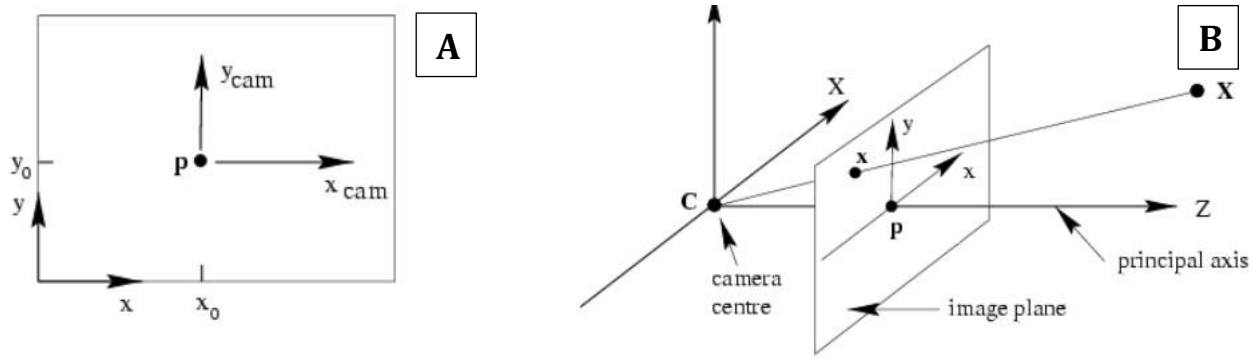

Figure 2.3 *The image plane (A) with the position of the principal point. The principal point is the intersection of the principal axis and the image plane (B)*

The *spatial resolution* describes how many metres in real life one pixel in the image represents, which varies with distance from the object measured to the camera. The focal length and size of object in the image ratio corresponds to distance to object and size of object in real world ratio, shown in **Figure 2.4** (Svanem 2010).

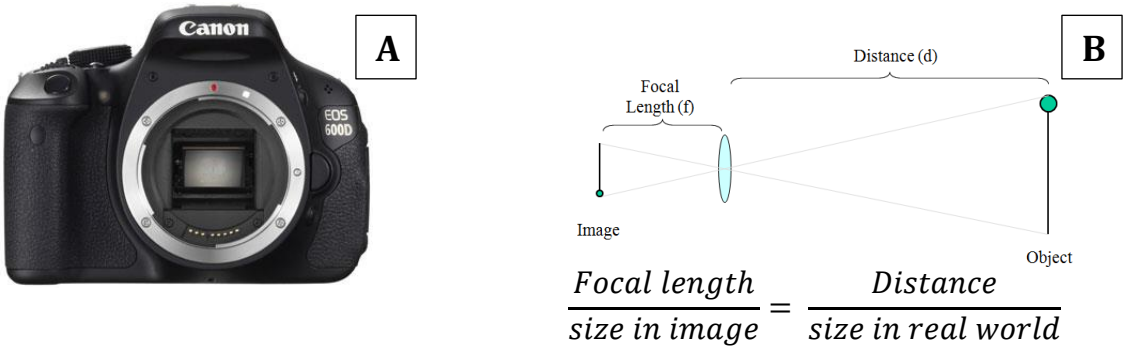

Figure 2.4 *Camera with the sensor (A) and the how the spatial resolution varies with distance to camera (B).*

Internal camera parameters specified by the manufacturers may deviate from actual parameters in different cameras. To know the exact values, a *camera calibration* is necessary. Many computer software packages can perform this operation, for example the Camera Calibration App in the Computer Vision System toolbox in MATLAB, as used in this thesis.

Lens distortion is the phenomenon where straight lines in the real world appear curved in the 2D image plane, and this can result in errors in photogrammetry. By calibrating the camera, the various distortion coefficients can be found and distortion accounted for, thus reducing errors.

External camera parameters are the camera position in real world coordinates and the view direction. The position of the camera is typically found in the field by the use of a GPS, and was in this study. The view direction is defined by three variables; yaw, pitch and roll. Yaw is the rotation about the vertical, z axis. Pitch is the up/down angle of the camera, and roll is the horizontal tilt.

A camera on a tripod will never be 100 % stable, due to external factors like wind gusts, wildlife (**Figure 2.5**), temperature changes and ground movement due to freezing and thawing. This results in minor changes in camera view direction through time and therefore also the image sequence (Eiken and Sund 2012). Camera motion can either be corrected for before or after the feature tracking process. Both methods use the apparent movement of static features, e.g. mountains, as a basis. If it is performed before the feature tracking, one reference frame is chosen and all the other frames in the sequence are oriented according to this using computer software. If it is done after, the apparent movement of static features in the image is subtracted from the measured feature track.

Figure 2.5 *Suspicious wildlife in front of time lapse camera 5 that may result in camera motion.*

2.3 Study area

Svalbard is an archipelago located at the NW limit of the European continental shelf in the High Arctic between 74°- 81° N 10°-35° E, and comprises an area of about 61.022 km^2. The largest island is Spitsbergen, followed by Nordaustlandet, Edgeøya, Barentsøya and Kvitøya (Moholdt 2010). Kronebreen is situated at the head of Kongsfjorden, 15 km east of Ny-Ålesund, see **Figure 2.6.** Kongsfjorden is a SE-NW trending fjord, approximately 27 km long and 3–5 km wide, with water depths of around 100 m in the inner fjord (Svendsen et al. 2002) to a maximum of 428 m (Glasser and Hambrey 2001). Kongsfjorden also has an unrestricted connection to the warm West-Spitsbergen Current (Luckman et al. in review). Close to 80% of the fjord drainage basin area is glaciated, mostly by tidewater glaciers (Glasser and Hambrey 2001).

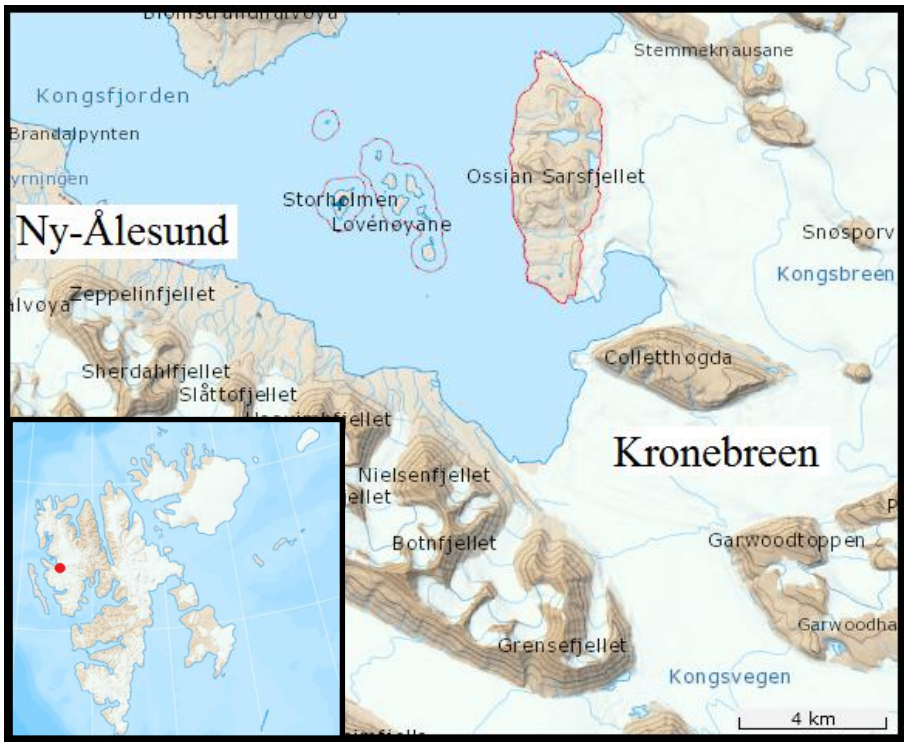

Figure 2.6 *Location of Kronebreen and Ny-Ålesund.*

2.3.1 Climate

Due to its location, Svalbard is extremely sensitive to climatic changes (Humlum et al. 2003). The Svalbard climate is relatively mild for its latitude due to the northward Atlantic current that brings warm water to the west coast of Spitsbergen (Moholdt 2010, Hagen et al. 1993). Winter temperature variations are bigger than the more stable summer temperatures. The mean annual air temperature of western Spitsbergen is -6°C, with July as the warmest month with an average of 5-6°C and the coldest period is Jan-March with an average of -15°C (Hagen et al. 1993). The Sverdrup meteorological research station in Ny-Ålesund has a continuous weather record from July 1974 to the present day. **Figure 2.7** shows the mean air temperature for June, July and August the last 20 years (NMI 2015).

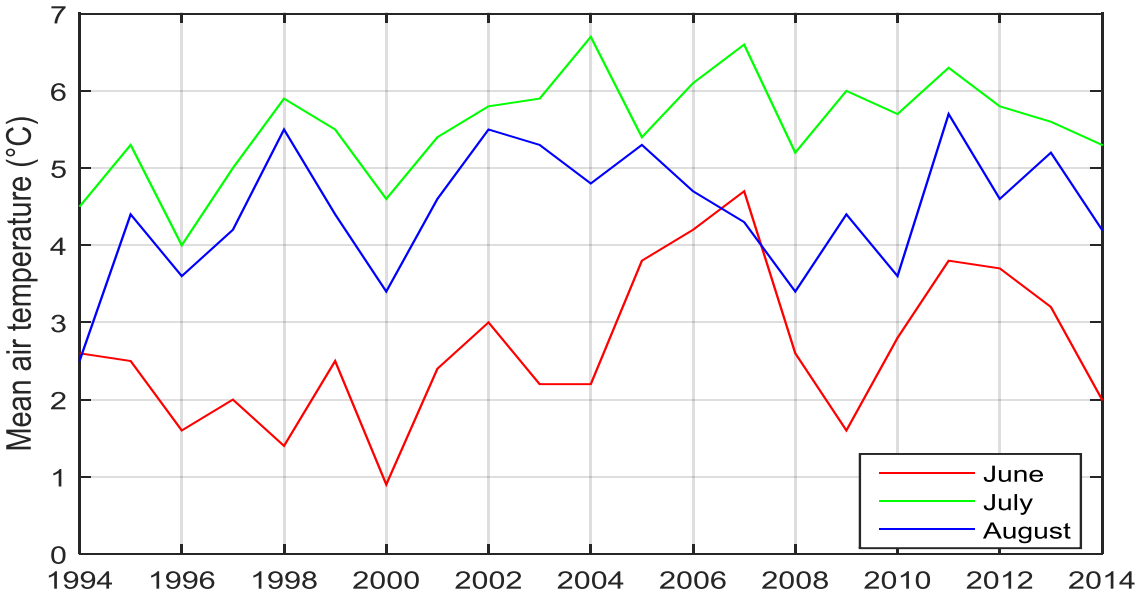

Figure 2.7 *Mean air temperature for June, July and August from 1994 to 2014 (NMI 2015).*

Precipitation in the Arctic is low because air masses are usually stably stratified and contain only small amounts of water vapour. Local gradients in precipitation occur, for example the normal annual precipitation at Svalbard airport from 1961 to 1990 was 190mm, which is one third of the precipitation in Barentsburg for the same period (Førland and Hanssen-Bauer 2003). Sand et al. (2003) concluded that the East coast of Spitsbergen receives 40% more snow, in water equivalents, than the west coast, and the southern part of the island receives twice as much winter precipitation than the northern part.

2.3.2 Geology

The mountains surrounding Kronebreen consist mostly of horizontal Carboniferous and Permian beds of sandstone, shale and coal. The famous pyramid shaped Tre Kroner peaks; Svea, Nora and Dana, located east of Kronebreen, have a top of Carboniferous and Permian strata, with gently folded Devonian rock underneath. Steindolpen nunatak consists of mostly gneiss, from lower to middle Proterozoic time (Hjelle 1993).

On the northern margin the glacier erodes red sandstone of Carboniferous age from Collethøgda (**Figure2.8**), and transports large quantities of sediments with the meltwater into Kongsfjorden giving it a red colour and the bay is therefore named Raudvika (Nuth et al. 2015). The discharge of melt water is very dynamic, and changes location through time. Subglacial discharges have developed a huge grounding line fan, and based on this Trusel et al. (2010) calculated a sediment yield of 1.4 x 10^3 tonnes/km^2/year for Kronebreen and the tributaries, which represents an effective erosion rate of 0.56 mm/year.

Figure 2.8 *Kronebreen enters Kongsfjorden and the mountain Collethøgda*.

2.3.3 Glaciology

About 59 % of the Svalbard archipelago is covered by glaciers which represents an area of approximately 35 528 km^2 (Nuth et al. 2015). The size ranges from huge ice caps like Autsfonna (8357 km^2) and Vestfonna (2402 km^2) at Nordaustlandet, to smaller cirque glaciers in the alpine terrain of western Spitsbergen (Nuth et al. 2015).

The 'Little Ice Age' glacier maximum in Svalbard occurred later than on mainland Norway, ending around 100 years ago, and most of the glaciers have retreated since (Blaszczyk et al. 2009). The overall net balance of glaciers in Svalbard is calculated to be -4.5 km^3± 1km^3 /year (Hagen et al. 2003b).

The temperature regime of Svalbard's glaciers is mostly polythermal, with the base frozen to the ground in the terminal zones and ice at the pressure melting point in the accumulation area (Hagen et al. 2003a). Land terminating glaciers have typical surface velocities of ~10 m/year, and tidewater glaciers up to an order of magnitude higher (Hagen et al. 2003a). Around 33% of the glaciers in Svalbard are surge type (Blaszczyk et al. 2009), meaning they shift between a short and rapid phase, *surge phase*, and a slower and longer phase, *quiescent phase* (Benn and Evans 2010).

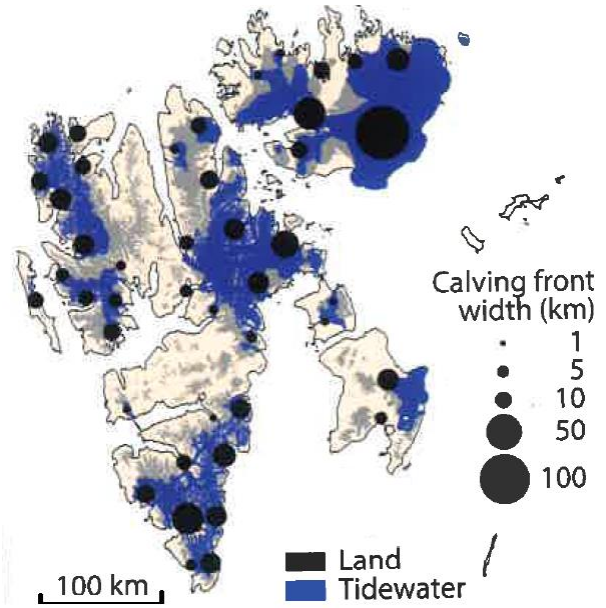

Figure 2.9 D*istribution of land-terminating and tidewater glaciers in Svalbard (Nuth et al. 2015).*

Two thirds of the glaciated area is drained by tidewater glaciers (**Figure 2.9**) (Nuth et al. 2015). 60 % of the Svalbard glaciers terminate in tidewater and are thus subject to calving dynamics (Sund 2011). The total length of calving ice fronts in Svalbard is about 860 km (Blaszczyk et al. 2009) and all margins are grounded (Dowdeswell 1989) or at least not currently able to maintain a stable floating termini (Sund 2011). Austfonna is the biggest ice cap in the Eurasian Arctic, and situated in Nordaustlandet, in North East Svalbard. This ice cap loses 2.5 km^3 ice annually due to calving alone, representing 45% of the calving flux from the whole Svalbard Archipelago (Dowdeswell et al. 2008). The annual total runoff from Svalbard glaciers is 800 mm ±150mm /year, where calving represents 16% (Hagen et al. 2003a).

During the last 40 years, Svalbard glaciers excluding Austfonna, have contributed to global sea level rise with a rate of 0.026 mm/year (Nuth et al. 2010). An increase in the calving flux for Svalbard's glaciers is currently anticipated, which will lead to many tidewater glaciers retreating eventually terminating on land (Blaszczyk et al. 2009).

2.3.4 Kronebreen

Kronebreen is a grounded polythermal tidewater glacier situated in Kongsfjorden (**Figure 2.10**). The glacier trunk drains a 390 km^2 area comprising the ice masses Holtedalsfonna, Dovrebreen and the smaller cirque contributory glacier Infantfonna (Nuth et al. 2012). The whole glacier system is 50 km long with an elevation range from 1400 m.a.s.l. to sea level (Nuth et al. 2012), and the bed is located down to 80m below sea level at some parts between the front and 7 km upstream (Kääb et al. 2005; Lefauconnier et al. 1994; Sund et al. 2011). The calving front is grounded at a water depth of about ~70 m (Luckman et al. in review) and the cliff height varies from 10-60 m (Sund et al. 2011).

Figure 2.10 T*wo glaciologists looking down on the heavily crevassed Kronebreen.*

Velocities and front positions

Kronebreen is one of the fastest moving glaciers in Svalbard, with annual velocities of up to 300-800 m/year at the front, or 1-2 m/day (Kääb et al. 2005; Nuth et al. 2012). Liestøl (1988) reported velocities up to 4 m/day. Kääb et al. (2005) calculated maximum speeds of more than 800m/year (2.2 m/day) just above the calving front around July 2001 (**Figure 2.11**).

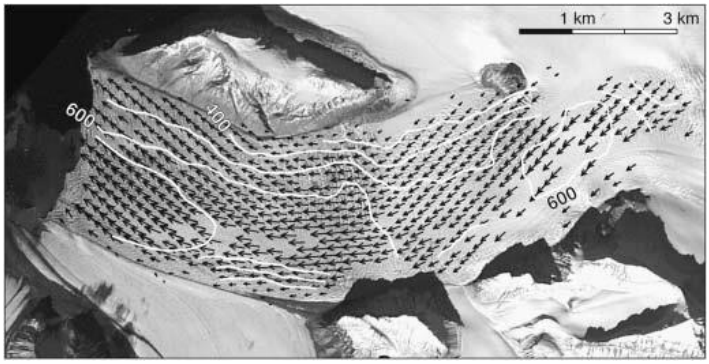

Figure 2.11 *The surface velocity field for the lower part of Kronebreen, derived from aster imagery of June 26th and August 6th 2001. The isolines are speed in metres per year* (Kääb et al. 2005).

Rolstad and Norland (2009) used ground-based radar and measured velocities of 2.5 m/day in August/September. Using feature tracking on Terra-SAR-x imagery, Luckman et al. (in review) found winter velocities from 1.5-2 m/day and summer peaks of 3 – 4 m/day. Velocities of Kronebreen have been measured using terrestrial photogrammetry before. Velocities in May were calculated to be around 2.5 m/day and peak velocities occurred in mid-July and August with values around 5 m/day (Svanem 2010).

5 km upstream from its calving front, Kronebreen joins the surge type glacier Kongsvegen, separated by a pronounced medial moraine (**Figure 2.11**). Kongsvegen is now in its quiescent phase, and flows with velocities of 1.4 -3.6 m/year, reflected by a smooth surface relative to the heavily crevassed Kronebreen (Melvold and Hagen 1998; Trusel et al. 2010). Kronebreen has never been observed to surge, but according to Liestøl (1988) based on Loven's expedition, it surged in 1869. Kongsvegen surged in 1948, and this is reflected in a shift of the medial moraine observed in photos by Kääb et al. (2005).

Kronebreen has a 175 year history of documented front positions (Sund et al. 2011). Receding rates of Kronebreen have been measured from zero to 300 m/year, with an average of 200m/year (Lefauconnier et al. 1994). Since 1998 the joint front of Kronebreen and Kongsvegen has retreated more than 4 km (Kääb et al. 2005). During winter Kronebreen advances modestly, and has a net annual retreat during summer of about 350m.

Calving

Kronebreen has a 3 km long calving front, and is among the 10 largest contributors to the total calving flux of the Svalbard archipelago. The calving rate and flow velocity of the front of Kronebreen have been measured using ground-based radar based in August/September 2007. The results show that calving events do not influence the speed further up-glacier, but an increase within 30m from the front happens before the calving event, and it goes back to normal after the event (Rolstad and Norland 2009).

The nature of single-event calving at Kronebreen was investigated by continuous visual observations of the front (Chapuis and Tetzlaff 2014). The events were described with type, location, time and size. No significant correlations with external factors like temperature and tide and calving activity were found. It has been concluded that the local geometry and water depth around Kronebreen are controlling the strain rates, crevasse patterns and ultimately the calving activity (Chapuis 2011). In addition, Sund et al. (2011) concluded that that they found no clear relationship between calving activity and their velocity record of Kronebreen, and that major calving events occurred randomly.

Köhler et al. (2011) identified calving activity at Kronebreen using seismic recordings 1 km from the front. They found an increase in calving related seismicity, when the glacier slowed down in autumn (2009 and 2010).

Luckman et al. (in review) referred to the terminal frontal ablation rate instead of calving rate, because of the significance and importance of submarine undercutting that is going on at the terminus. They measured frontal ablation rate peaks of ~8m/day (**Figure 2.12**). The maximum rates occur in September and October, and the authors concluded a strong correlation (r^2=0.84) between the seasonal pattern of frontal ablation and the mean annual cycle of sub-surface temperature. The frontal ablation rate pattern was similar for several glaciers in Svalbard, despite different dynamic behaviour.

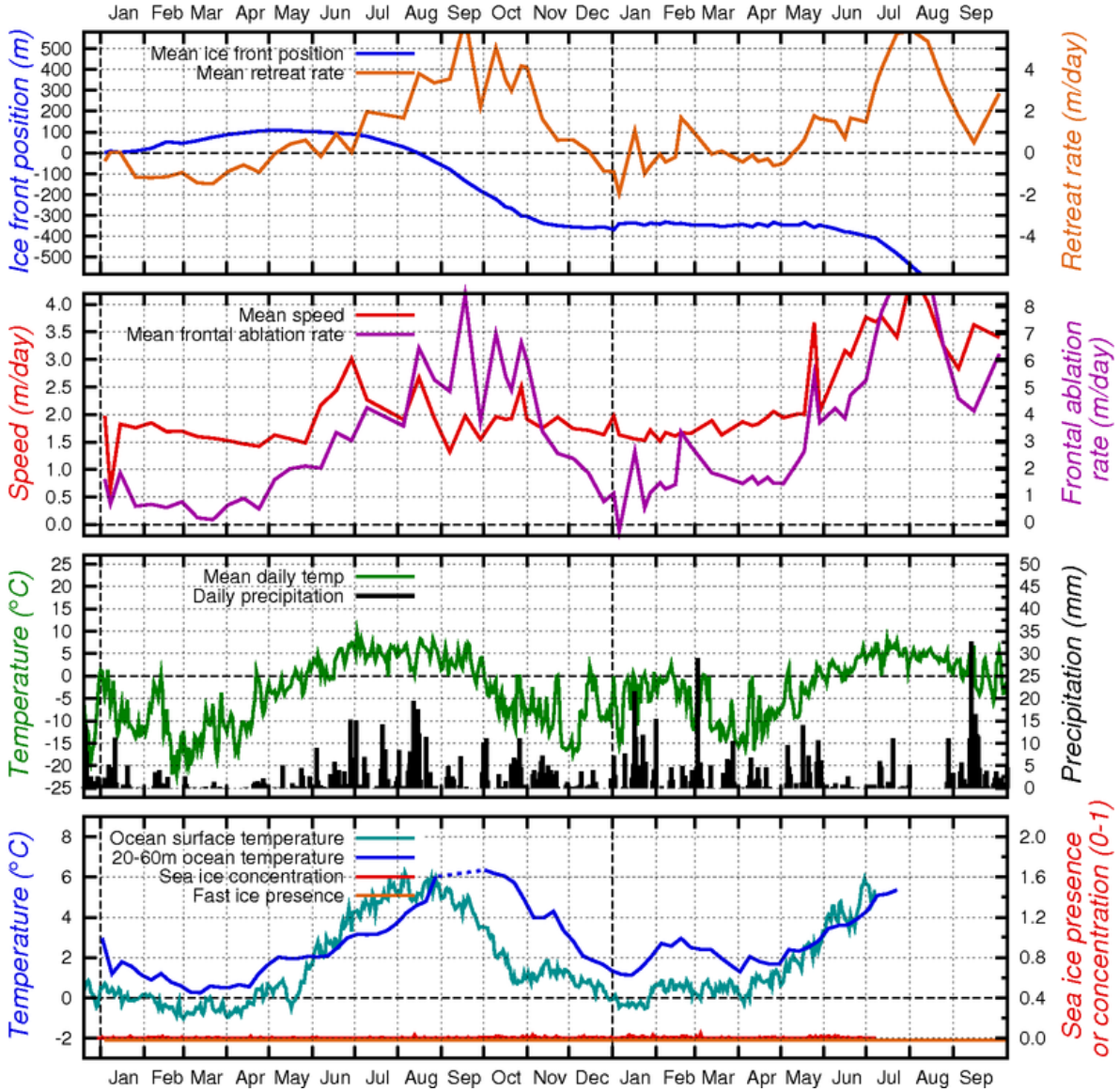

Figure 2.12 *Ice front positions, retreat rates, velocities and frontal ablation rates for Kronebreen during 2013 and 2014 based on TerraSAR-x imagery, from Luckman et al. (in review).*

3 Data and methods

3.1 Camera platform

In May 2014 the CRIOS team flew out with 7 time-lapse cameras and installed them on the mountains above Kronebreen's margin (**Figure 3.1**). The camera platforms (**Table 3.1**) were pre-made and ready before the team went out, to minimize the time in the field and helicopter expenses. All the cameras were programmed to take photos every 30 min simultaneously, and the midnight sun allows images to be taken 24h a day during the period. In the last field operation, a precise measurement of the camera position was computed using a dual-band (L1-L2) differential GPS.

Figure 3.1 *Wires connected to bolts drilled into bedrock made sure of a stable camera platform.*

Table 3.1 *The camera platform*

Camera	Canon Eos 600D
Focal length	20/24 mm
Image format	3456 x 5184 pixels
Timer	Digisnap2700, Harbortronics
Enclosure	Modified Peli Storm case
Power	Sealed lead-acid batteries powered by solar panels
Support	Tripod, steel wire guys and expansion rock bolts
Camera location	UTM: 447906 8759453 Height: 387 m.a.s.l.

3.2 Data

3.2.1 Imagery

In September 2014, the memory cards were collected, and showed that the cameras had worked perfectly resulting in around 6600 images each. These images are used as data for this thesis. The weather around Kronebreen is not always sunny; around 30% of the daily images taken at 12:00 are lost due to poor visibility (**Figure 3.2**; **Figure 3.3**; **Figure 3.4**).

Figure 3.2 *May 28th had too poor visibility to be used in the thesis.*

Figure 3.3 *July 12th also had too poor visibility to be used in the thesis.*

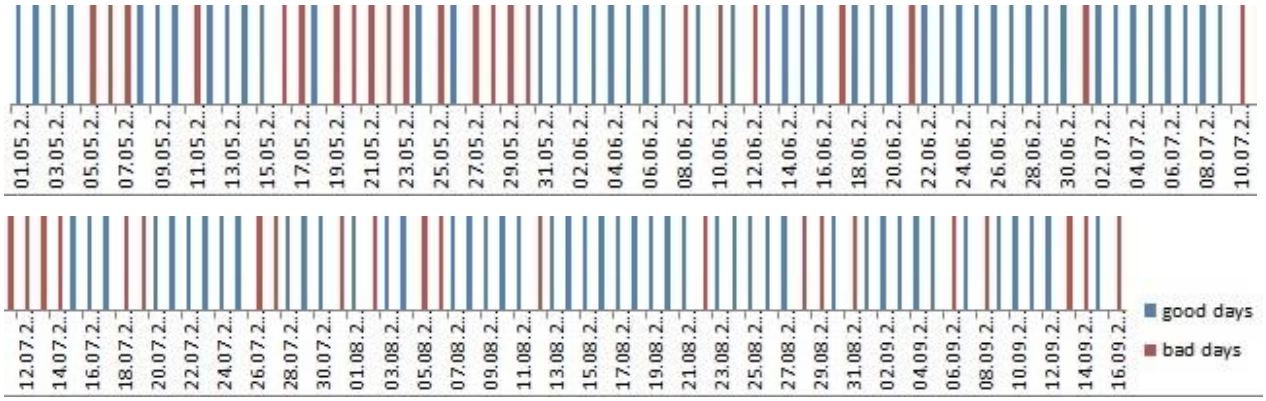

Figure 3.4 *Overview of poor visibility days (shown in red) and good visibility days (shown in blue) from images taken daily at 12:00.*

3.2.2 Additional data

In addition to data collected from the fieldwork the following datasets are used:

- 4 aerial photos taken in 2009 by Norwegian Polar Institute (NPI)(**Table 3.2**).
- A digital elevation model (DEM) developed by Jack Kohler (NPI) from a UAV in 2008 with a cell size of 50 x 50m and an extent (UTM-WGS 84 Zone 33X) from E 431750- 470000, N 8747950- 8768000.
- A TanDEM-X DEM from 2013 with a cell size of 10 x 10m, extent (UTM- WGS 84 Zone 33X) of E 446000- 460000, N 8753000- 8761800 provided by Adrian Luckman (Swansea University).
- Data on velocity and calving rates of Kronebreen from the same period as our time-lapse data, calculated from TerraSAR-X data (every 11 day) by Adrian Luckman.
- Air temperature and precipitation data from the meteorological station in Ny-Ålesund (NMI 2015).

Table 3.2 *ID of the four aerial photos (NPI)*

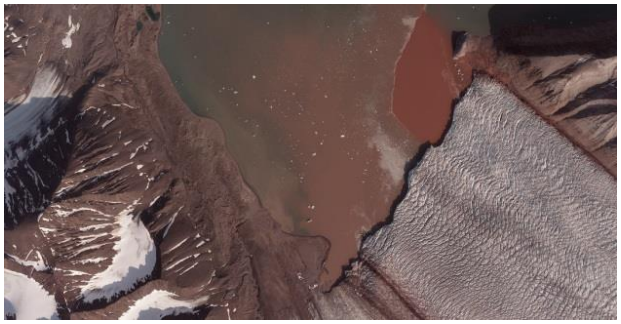
s2009_13822_00784_l3_rep_RGB

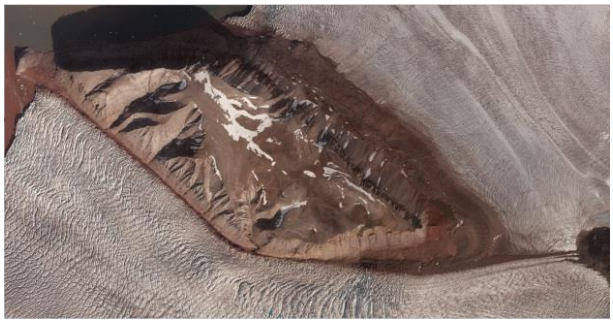
s2009_13822_00793_l3_rep_RGB

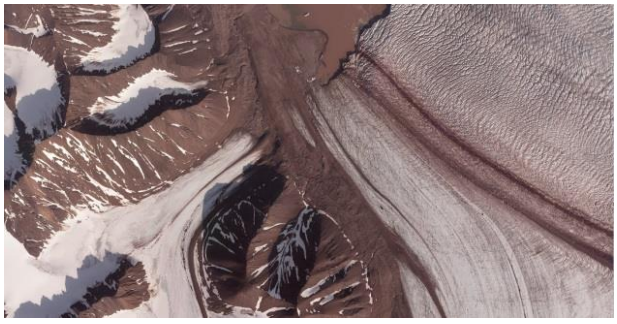
s2009_13822_00786_l3_rep_RGB


s2009_13822_00791_l3_rep_RGB

3.3 Methods

3.3.1 Finding the optimum software

Several software packages were evaluated based on how user-friendly and automated they were, in addition to how many inputs they required (**Table 3.3**). The software needed to conduct camera calibration, feature detection, feature tracking, account for camera motion and georectification.

Table 3.3 *Overview of the softwares evaluated to find the most suitable one.*

Software	Features	Author	Ref.
Cias	Feature tracking	Andreas Kääb	*Kääb A. (2013). Image correlation software CIAS. http://www.mn.uio.no/icemass.*
PRACTISE	Georectification	Stefan Härer	*Härer, S., Bernhardt, M., Corripio, J. G., and Schulz, K.: PRACTISE – Photo Rectification And ClassificaTIon SoftwarE (V.1.0), Geosci. Model Dev., 6, 837-848*
Photo Modeler	Feature tracking	Eos Systems Inc.	*http://www.photomodeler.com*
ImGRAFT	Feature tracking, georectification	Alexandra Messerli Aslak Grinsted	*http://www.imgraft.glaciology.net*
Pointcatcher	Feature tracking	Michael James	*http://www.lancaster.ac.uk/staff/jamesm/software/pointcatcher.htm*
Computer Vision System	Feature tracking, camera calibration	MATLAB	*http://se.mathworks.com/products/computer-vision*

Cias is written in IDL and calculates offsets between image pairs using Normalized cross-correlation (NCC), but input images need to be georectified. PRACTISE is a georectification toolbox in MATLAB that can be used in combination with Cias. PhotoModeler can do both feature tracking and convert the pixel offsets to real world coordinates, but the software is not free of charge. ImGRAFT is a MATLAB toolbox that includes all the functions needed, except feature detection. Pointcatcher can do both feature detection and tracking for image sequences, but not convert the offsets to real world scale. Computer Vision System is a toolbox in MATLAB and can do most of the features required, but is not free of charge, and lacks the georectification part. The conclusion was to use the ImGRAFT toolbox, and the feature detection from Pointcatcher. Additionally the Camera Calibration App from Computer Vision System Toolbox was used to find the camera parameters.

3.3.2 Extracting Ground Control Points

Ground Control Points (GCPs) are points with both known world coordinates (xyz) and pixel coordinates (uv) in the image. Points like these are important pinning points when converting from either 2D (uv)-3D (xyz) or opposite.

The world coordinates in the GCPs are extracted from viewing the DEM in the ArcGIS software *ArcScene* and *ArcMap*, with georeferenced aerial images draped over it (**Figure 3.5**), combined with the digital NPI map from www.toposvalbard.npolar.no. The pixel coordinates are extracted by viewing the images from the time-lapse data in the software MS Paint and locating points that correlate with the DEM points with a precision of 5-10 pixels.

Figure 3.5 *10 m resolution DEM from 2013 with the four aerial photos draped over it. This model was used in combination with the digital Toposvalbard map to find real world coordinates of ground control points in the images in Table 2.*

3.3.3 Camera Calibration

The camera calibration was performed using the Computer Vision System toolbox App called Camera Calibration in MATLAB (**Figure 3.6**). The process includes laying out a printed checkerboard sheet with known size of each square on the floor. The corners are identified automatically by the program in images taken from various distance and angles from the camera on a tripod. By detecting the corners of the checkerboard squares in the different images the program can calculate the inner camera parameters, like focal length, lens distortion, principal point and the sensor size. The values for the camera parameters in addition to the estimated errors are exported as two variables into MATLAB.

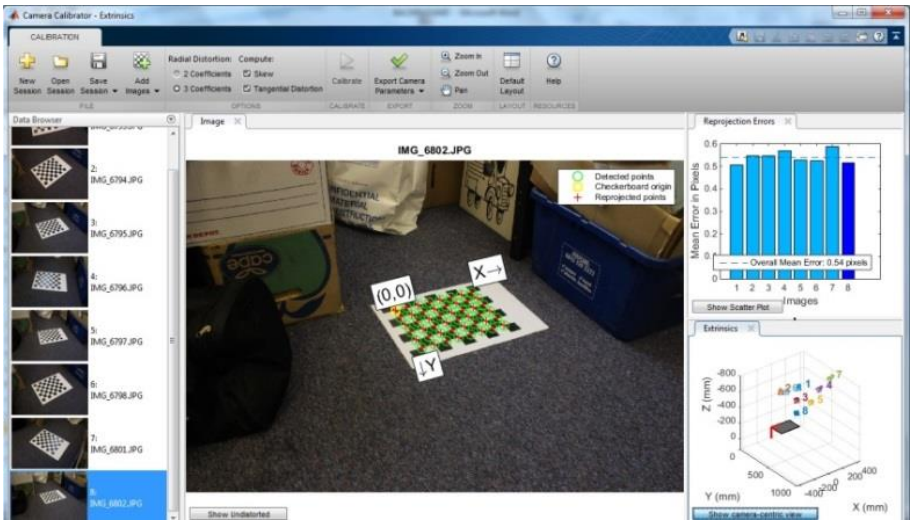

Figure 3.6 *The interface of camera calibration app in matlab, including the images used (left), the reprojection error for each image (upper right corner) and the camera positions relative to the checkerboard sheet (lower right corner).*

In this thesis, a MATLAB script based on the ImGRAFT toolbox was written (**Appendix 3**). ImGRAFT is an open source image georectification and feature tracking toolbox for MATLAB developed by Aslak Grinsted and Alex Messerli (University of Copenhagen) (Messerli and Grinsted 2015). Inputs to the functions are images, a DEM, GCPs and information about the camera position, view direction and internal parameters.

3.3.4 *Optimising camera parameters*

The first ImGRAFT function is to optimise the input camera parameters using the GCPs (**Figure 3.7**). The function tunes the camera so that xyz coordinates results in their uv equivalents(least squares). The following parameters can be optimised: Camera position (xyz coordinates from the DEM), image size (number of pixel rows and columns), view direction of camera (yaw, pitch and roll), focal length in pixel units, camera centre in pixels, radial and tangential distortion. When the camera parameters are solved, they are saved as a 20 element vector called *fullmodel* (Messerli and Grinsted 2015). The *optimizecam* function has a root-mean-square-error output, to indicate how successful the optimisation process is.

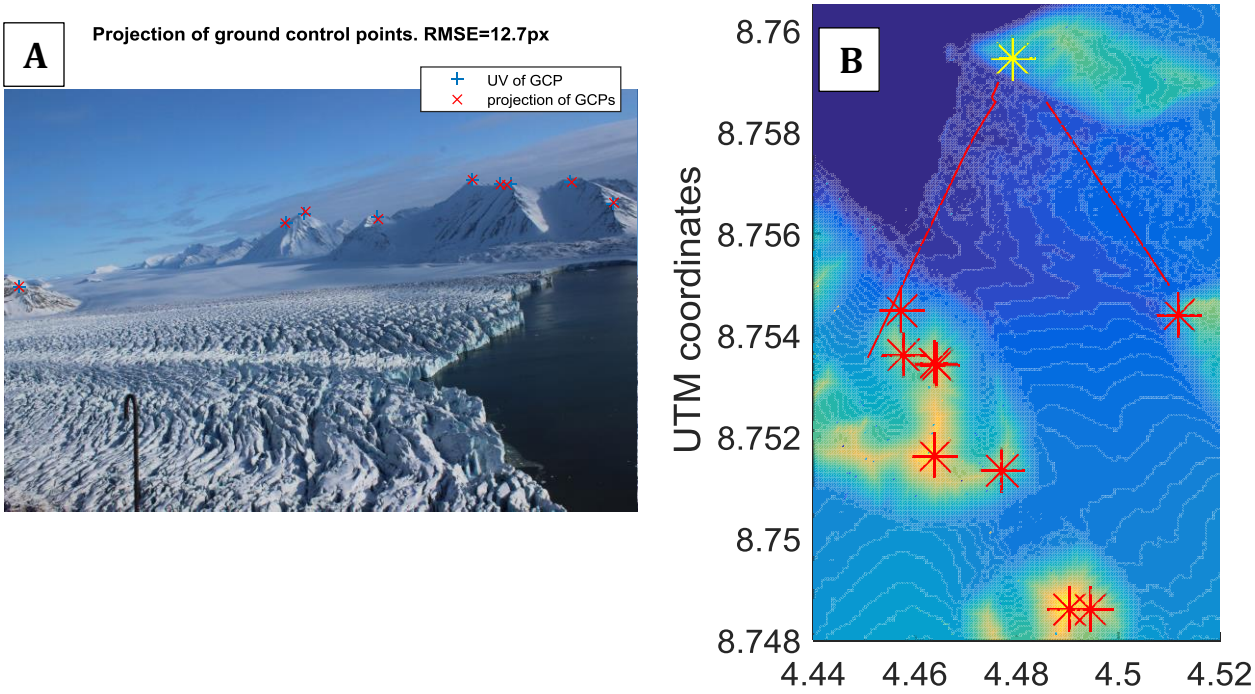

Figure 3.7 *The position of ground control points in uv coordinates, and the projected position of the GCP using the optimised camera model, with a root-mean-square-error (RMSE) of 12.7 pixels (A). Figure B shows the position of the cameras (yellow star), where the most eastern camera is the main camera used. The viewshed of the main camera (red lines), and position of ground control points (red stars) over the DEM from 2008.*

3.3.5 Camera motion

To measure the ice velocity from the time-lapse imagery, it is important to account for the camera rotation between each image in the sequence. Several external factors can affect the camera platform; wind gusts, wild animals, temperature changes, and frost heave due to permafrost. These will all result in pixel displacements in the image sequence, which does not represent glacier movement. This problem was solved by template matching of the static areas of the images, like the mountains in the background (**Figure 3.8**), using the Phase Correlation algorithm (Messerli and Grinsted 2015). All pixel displacement detected represents camera motion, and will be accounted for when tracking the glacier. ImGRAFT calculates the change in view direction (yaw, pitch and roll) for each image in the sequence individually, and develops a new camera model belonging to each frame. The advantage of using camera model is that no pre-processing of the images is necessary. In other studies the images need to be oriented into the same reference frame to account for camera motion (Svanem 2010).

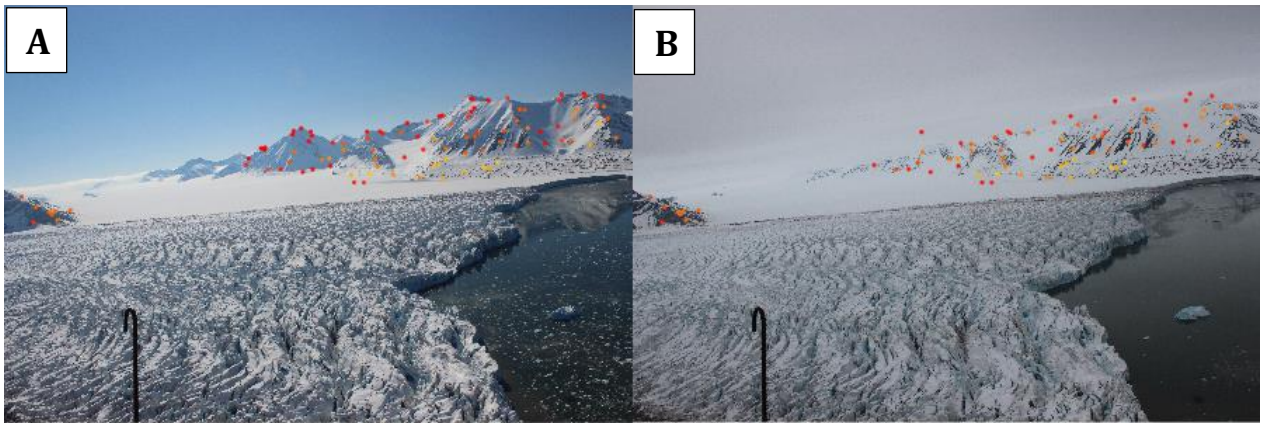

Figure 3.8 *Template matching of static points between two images from June 4th(A) and 5th(B) to account for camera motion. The colour of dots represents the quality of the matching process, where red is bad and yellow good.*

3.3.6 *Detecting Harris features*

To be able to correctly track points on a glacier surface, often referred to as *features*, it is important to detect and select well-functioning, distinct and robust features in the frames. In computer vision several "detectors" have been developed; the *Harris Detector* is one example (Harris and Stephens 1988). The Harris-Stephens algorithm is based on complicated mathematics, but basically detects features with a large change (steep gradient) in the intensity value in at least two directions. An edge will only have a steep gradient in one direction, a corner has in two directions and a dot will have a steep gradient in all directions.

Pointcatcher is MATLAB-based software developed by James (2015) (**Figure 3.9**). The software can both detect and track features over longer image sequences in pixel coordinates, and the output file is an array with pixel coordinates for each point in every image frame. The software was used to detect points in static areas of the image that are easily recognisable in the next frame in the image sequence. Pointcatcher uses Harris corner detection. The user can set the preferred correlation threshold, template size, point detection area and threshold to accept Harris features. When the points of the static areas of the image were detected they were imported into MATLAB and used for template matching to account for the camera motion between images.

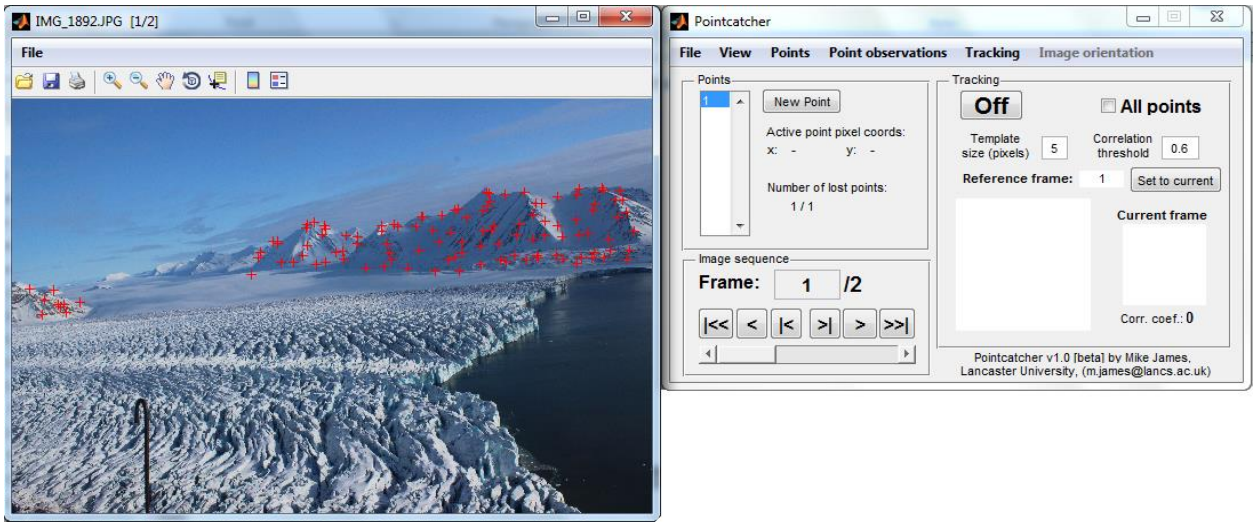

Figure 3.9 *The graphical interface of the MATLAB based software Pointcatcher. Here showing uv coordinates of Harris features detected in the static part of the image.*

3.3.7 Velocity calculations

Defining points on the glacier

Harris corners need to be defined within an area in the 2-D image plane. This causes trouble when it comes to evenly distribute points over the glacier surface in map view. If the corners are evenly distributed in 2-D, they will be much closer close to camera and more scattered in 3-D view. It is then very hard to perform a proper interpolation and to make accurate velocity contour maps.

The solution was to make a grid of points in real world coordinates, and then convert them into 2-D for the template match process. A moving grid is generated in the script, based on the front position of the glacier. This makes sure that the velocity of the glacier surface is calculated right at the front, even though the front is advancing or retreating. Also the moving grid makes sure that no points in the ocean are tracked.

Template matching of points on the glacier

These points are then converted to 2-D image coordinates using the *project* function in ImGRAFT, and only points within the field-of-view of the camera are selected. Template matching defines a template in one frame and locates the same template in the next frame, so as then to calculate the offset between the two (Ahn and Howart 2011; Heid and Kääb 2012). The template matching method used is ImGRAFTs own version of a Normalized Cross Correlation (NCC) algorithm. In the first frame a sub-image around the feature is selected, a *template*. The position of the template is defined by a point at the centre of the template. In the next frame a *search area* is chosen and a *search template* of equal size as the reference template will search within this area (**Figure 3.10**). By using various algorithms (NCC) the similarity between the reference template and the search template is calculated and the best match is chosen.

The size of the reference template should be large enough to maximize signal-to
- noise ratio and make sure it is unique, but any increase in size also increases the computing time. The size of the search area needs to be big enough to cover the displacement distance of the template between the two frames (Debella-Gilo and Kääb 2011; James et al. 2014).

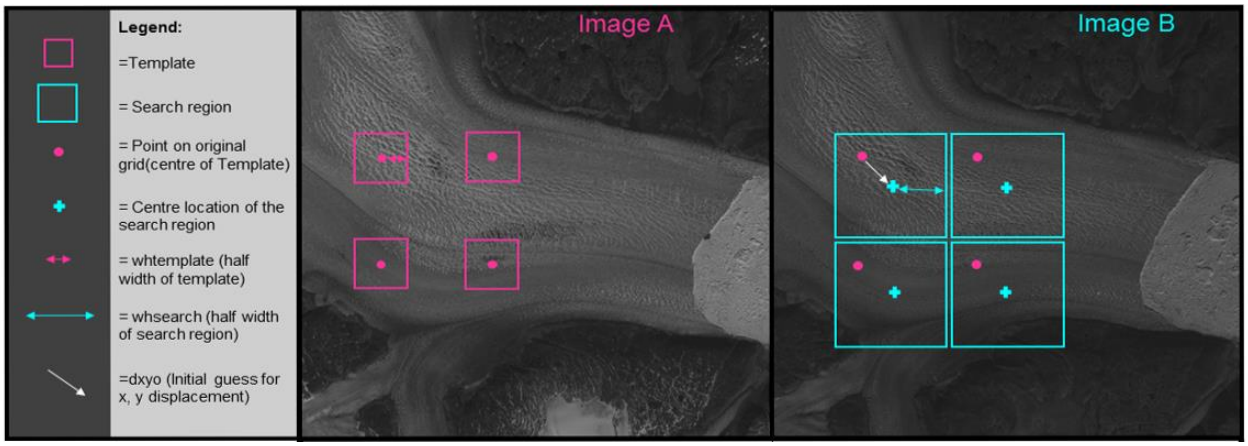

Figure 3.10 *A templatematch example where the of templates are pink and the search regions are blue (www.imgraft.glaciology.net)*

The *templatematch* function calculates the offset (dxy), which means a point A(x, y) in image A has moved to B(x+dx, y+dy) in image B, and the uvB array is equal to uvA + dxy. It is possible to watch the process in MATLAB with pixel offsets displayed, and therefore easier to select the most suitable template and search size (**Figure 3.11**). A super-sampling factor of 3 was used, which resampled the template and search windows. This increases the template match process precision to sub-pixel values (Debella-Gilo and Kääb 2011; Messerli and Grinsted 2015).

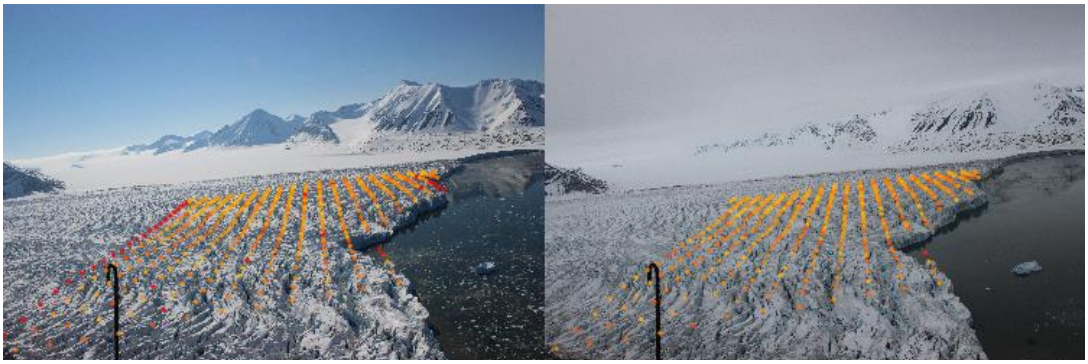

Figure 3.11 *The templatematch process between the images from Figure 3.9 (June 4th and 5th), here with a 75x75 m grid of points. The colour of each point represents the quality of the match, where yellow is good and red bad.*

Another output from the templatematch function is maximum correlation coefficient and average absolute correlation coefficient within the search region. A signal-to-noise ratio can be calculated based on the ratio of these two (Messerli and Grinsted 2015). A filter with a signal-to-noise ratio lower than 2 and a threshold for the correlation coefficient lower than 0.6 was included in the script, to lose "bad" matches.

Coverage of points

To see how well the glacier surface is covered in the image plane, the template size around each point tracked was plotted. In 2D this was done by plotting the converted uvA points onto the image and by adding a square around with same size as the template size (in pixels). **Figure 3.12** shows this, with a 50 pixels template size, and a uv grid of points, converted from a 75x75 m xyz grid of points. This is a rather large template size, and in combination with a rather dense point grid this costs a lot of computational power.

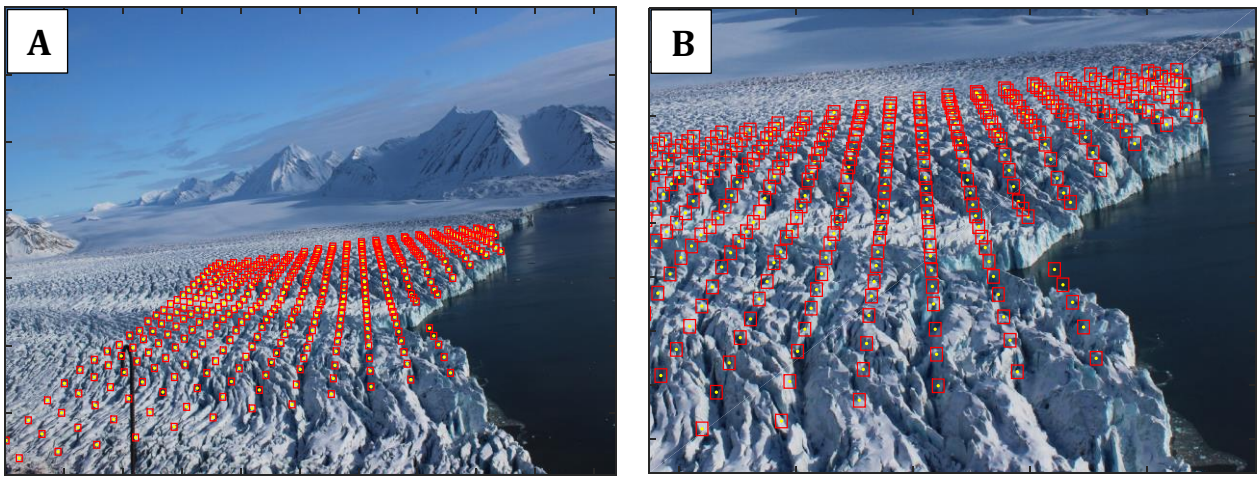

Figure 3.12 *The coverage of the templates in red, and coverage of uv points in yellow. Here the template size is 50 pixels, and the uv grid of points is converted from a 75x75 m xyz grid of points. Image B is a zoomed part of image A.*

Accounting for ablation

The DEM used to convert from 2D to 3D is from 2008. The main difference from this model and the present would be the front position, which does not matter since we know height and position of this from the imagery. The second, and more importantly change, is elevation change of the glacier surface mainly due to ablation and dynamic thinning. The surface lowering rate of Kronebreen was calculated to be around -1 m/year from the period 1990-2007 at the terminus (Nuth et al. 2012), which implies an elevation change around 7m may have occurred in period. This surface lowering could lead to an over-estimation of the velocities, depending on the relative lowering compared to the camera height. The camera is located 387 m above the glacier surface, and a 7 m surface drop leads to 1.8 % over-estimation of velocities. The DEM is thus lowered 7 m in the glacierised areas, so that the estimated ablation is compensated in the velocity calculation.

Georeferencing the tracked points

When the points on the glacier are tracked, pixel coordinates in the first and second image are located and offsets calculated. The points need to be converted from 2-D into real world 3-D velocities, i.e. the points need to be georeferenced. ImGRAFT uses the model camera parameters, the points array that includes the uv coordinates and the DEM as input in the *inverseproject* function for this conversion. This function performs a form of ray tracing to generate the 3-D coordinates of the 2-D points (Messerli and Grinsted 2015).

Calculating real velocities

When the real world coordinates (xyz) of the points tracked are known, the real world velocities can easily be calculated by subtracting position 1 from 2 for each point and then using Pythagoras to calculate the sum offset from the x and y offsets. In other words, this thesis focuses on 2-D velocities, and 3-D velocities that include height differences are not considered.

There will always be outliers when several hundreds of points are tracked. A filter based on a signal-to-noise-ratio threshold value and correlation coefficient lower than 0.6 was used. Another filter used, was based on the direction of the velocity vector. If the velocity direction deviated largely from the mean ice flow direction, the velocity results from this point were deleted. The last filter was a threshold value for the velocity itself. This was used to avoid measuring crevasse openings or ice fall instead of surface velocity, and set to 8 m/day.

Defining 11 areas on the glacier

To investigate both the spatial and temporal evolution of the surface velocity, areas along the front were defined. Flow lines with 100 meter spacing were defined in UTM coordinates, based on the mean direction of the velocity results (see dashed black lines in **Figure 3.13**). The flow lines were static and divide the glacier surface into 11 overlapping areas that extend from the front and 600 m up glacier. The 11 areas are moving as the front is retreating or advancing. More of the front could unfortunately not be investigated due to too large variations in pixel offsets, and lack computational power.

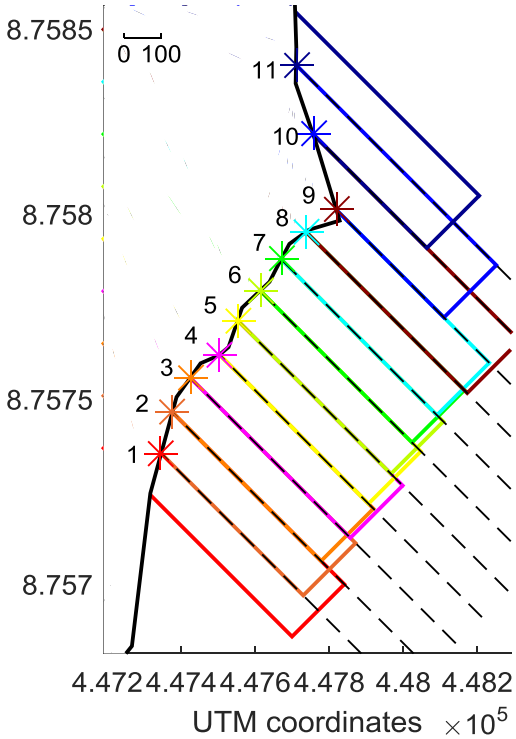

Figure 3.13 *The 11 overlapping areas with different colours, the front position from May 2nd (black), the flow-lines (dashed lines) and the intersection of flow-lines and front positions which equals the front points (stars).Each area is 200x600 m.*

The mean velocity of the points tracked within each area was calculated. The mean of these 11 values was also calculated. All the areas are overlapping 50% with the area next to it, which in turn means that each of the points is used for mean velocity twice. The number of tracked points within each area will vary in both space and time due to illumination changes and position of front. With a successful template matching process and a point grid of 75m x75m the maximum number of points within the 200m x 600m areas is 24. The point grid and the areas are not oriented parallel due to the direction of ice flow.

Choosing optimum time interval between frames

The dataset includes images taken every 30 min throughout the period. The ideal time interval between the images for extracting velocities was based on signal to noise ratio, and by running many test periods with different time interval to choose the best solution. A temporal resolution higher than daily introduces template matching problems (**Figure 3.14**), even though the offsets are large. This is mostly due to changes in Sun position and therefore changes in shadows between the images pair, because the NCC algorithm is sensitive to illumination changes (Messerli and Grinsted 2015).

The solution for the illumination problem was to use images taken at the same time each day, and choose a time which did not lead to any part of the glacier surface covered by shadow from the mountains. This unfortunately excludes the investigation of sub-diurnal velocities, which would be interesting to correlate with tidal data. One solution would be to use overlapping image pairs with a 24 hour interval, every 30 min. **Figure 3.4** shows an overview of images taken at 12:00 lost due to poor visibility. These days were replaced by images taken at different times during the same day. The date and time for the images used is found in Appendix 6.

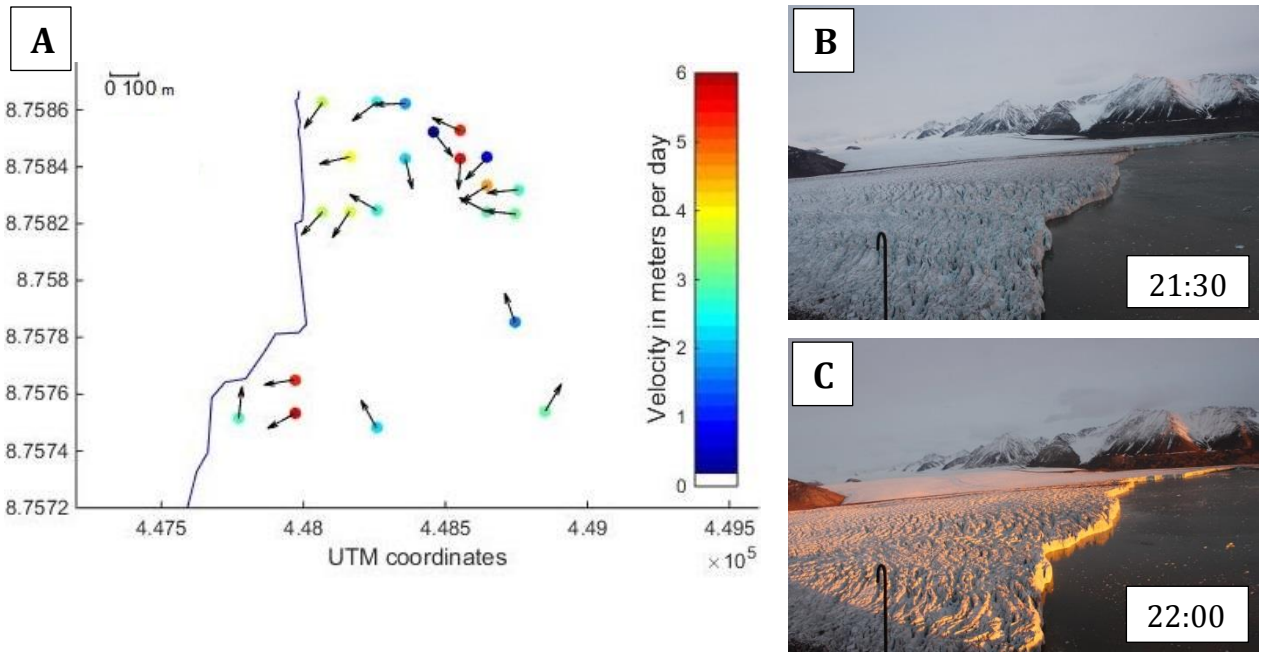

Figure 3.14 *Example of large illumination differences in an image pair with 0.5 hours interval from Sept 2nd(B and C). Colour of points indicates magnitude of velocity, and arrow indicates the direction(A). Most of the points tracked are lost due to filtering based on signal to noise ratio.*

3.3.8 Front positions

The front position of Kronebreen is defined as the intersection of the Kongsfjorden surface plane, and the vertical plane of the glaciers frontal cliff. Pixel coordinates from the front position were manually selected using Pointcatcher (**Figure 3.15 B**) with a precision of 5-10 pixels and converted to real world coordinates using the ImGRAFT *inverseproject* function.

A test was done to see how many metres this error represents in two different areas in the 2D image (**Figure 3.15 A**). A 10 pixels vertical displacement in the furthest-away mapped front represented 6.10 m, and a displacement closer in the image represented 2.30 m. 6.10 m is therefore the maximum uncertainty that might have occurred in the front position mapping.

The intersection of the 11 flow lines and the front positions defined the front point for the corresponding area (see stars in **Figure 3.13**). These front points were used to calculate ice front position through time and front retreat rate through time. The ice front position through time was calculated by subtracting the coordinates of all the front points of day 'n' from the coordinates of the front points from day 1. By using Pythagoras the distance between front 1 and front n was calculated and plotted against time. The front retreat rate was calculated by subtracting front point of day (n) from day (n+1), and dividing by the time interval between.

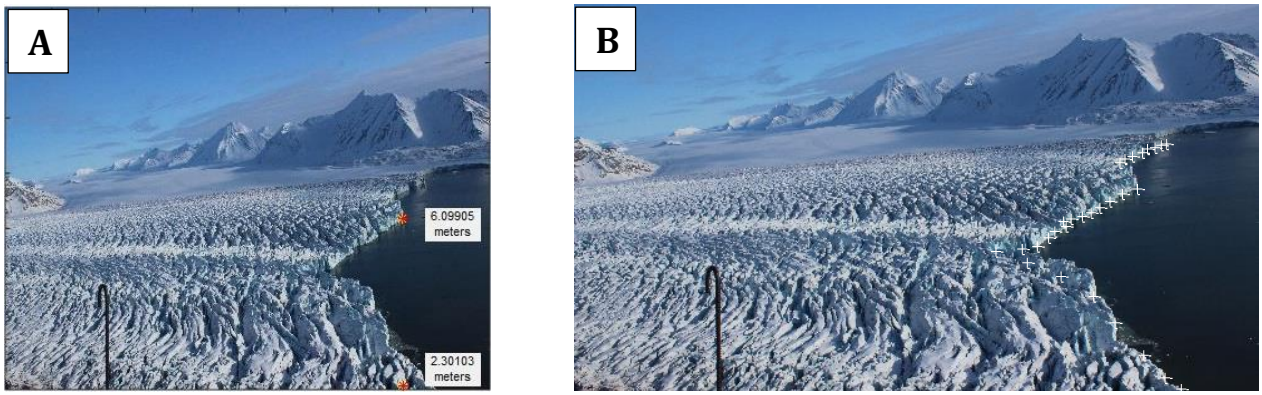

Figure 3.15 *The red and yellow stars in A represent offsets of 10 pixels. The number is how much the vertical pixel displacement represents in real world coordinate. B shows the manual front mapping process, where the white crosses represent uv-coordinates of the ice cliff-fjord intersection*

3.3.9 Calving rate calculations

The calving rate is calculated from the formula:

$$U_c = U_t - \delta L/\delta t \qquad \textbf{Eq. 2.1}$$

Where U_c is calving rate, U_t is the glacier velocity at the terminus, L is glacier length and t is time (Benn and Evans 2010). The velocity and the retreat rate have opposite directed vectors, and therefore the sum of them equals the calving rate. The calving rate was calculated for each of the 11 areas at a daily interval, and then plotted against time.

4 Results

4.1 Velocities

A time-velocity graph was developed by plotting the average daily velocity within each of the 11 areas (**Figure 3.13**) against time (**Figure 4.1**). One data gap at the end of May occurred due poor visibility caused by snow covering the lens.

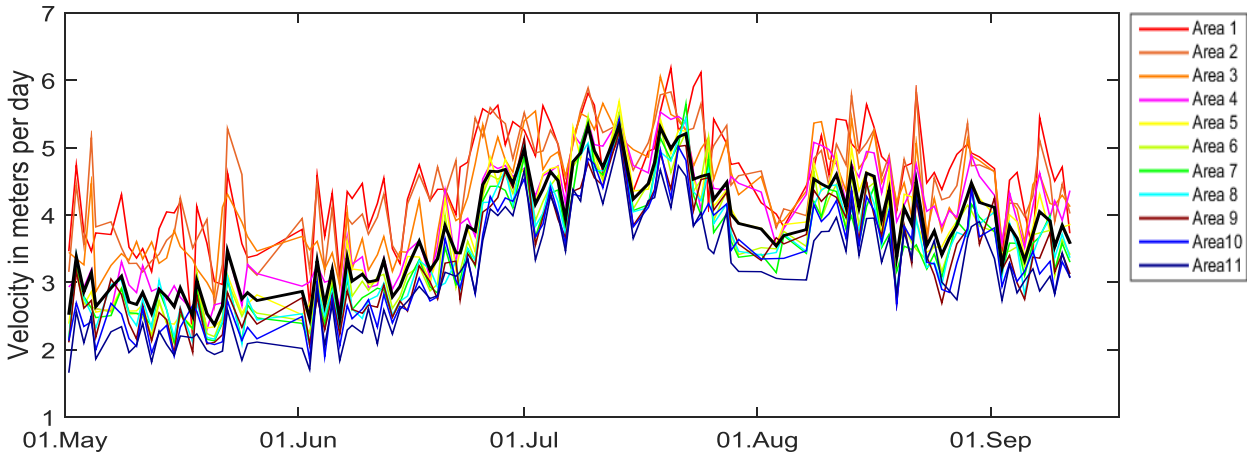

Figure 4.1 *Colour-coded mean velocity for each of the 11 areas (**Figure 3.13**) from May 1st to September 11th. The maximum number of point within each area is 24. The black line is the mean of each of the 11 values. The values are in metres per day, and the temporal resolution is 24 hours.*

4.1.1 Temporal variations

Mean velocities were stable around 3 m/day during May and increase during June up to 4.5 m/day. Peak velocities occurred in mid-July with values up to 5.3 m/day. From mid-July to the beginning of August the velocities slowed down, before they increased again in a new velocity peak at 4.7 m/day. The velocity decreases steadily to the end of the period and end at 3.7 m/day at September 11th. The velocity signal is generally irregular and jagged throughout the period, which may be explained by controls of the short term velocity. One data gap is obvious in late May due to data loss caused by bad visibility (snow).

4.1.2 Spatial variations

All the lines from the 11 areas in **Figure 4.1** follow each other nicely through the measured period, indicating that the variations in the velocity for the 11 areas are similar through time. Areas 1-4 have the highest velocities through the entire period, and these are the areas closest to the centre of the glacier trunk. Velocities here are twice as high as in Area 9-11 in May and June. Areas 9-11 are the slowest areas and closest to the margin towards Collethøgda. Areas 5-7 are close to the mean velocity and also in the middle of the section investigated, see **Figure 3.13**. In early to mid-July all the areas move fast and the velocity range is smaller compared to early and late in the period. The velocity variability is highest in May, where it ranges from less than 2 m/day to 5 m/day between the different areas.

Figure 4.2 shows the spatial distribution of surface velocity on July 15th, where fastest velocities are located closest to the front and closest to the centre line. The slowest velocities occur closest to the margin and up-glacier from the front.

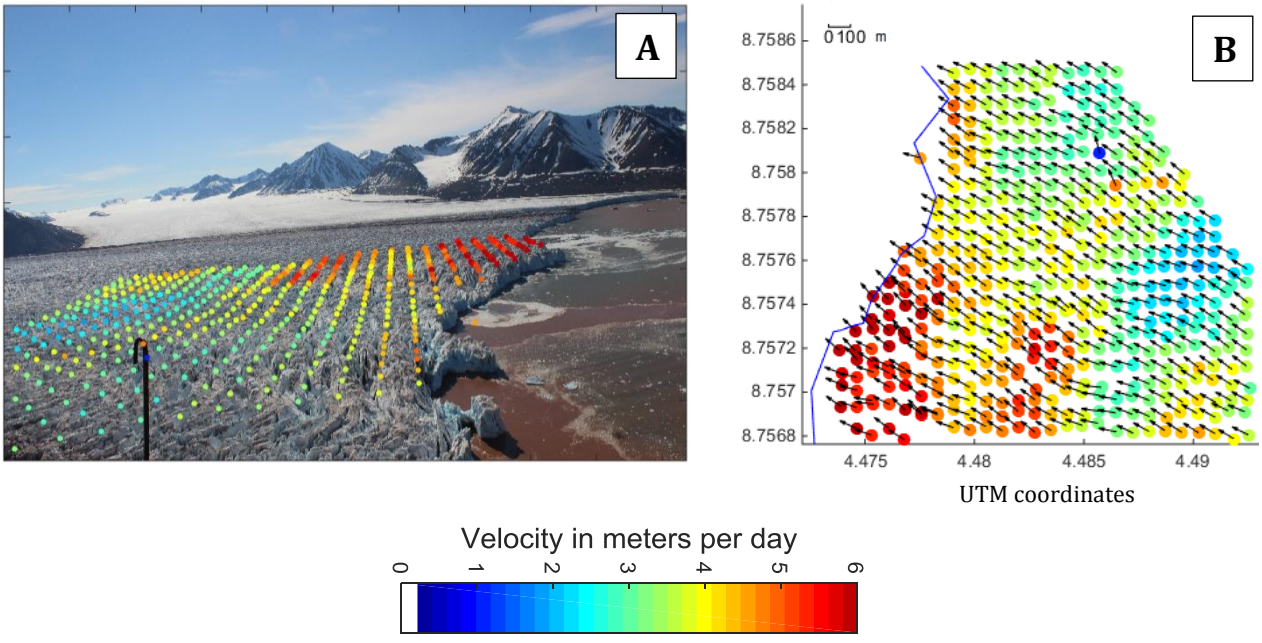

Figure 4.2 *Spatial distribution of surface velocity on Kronebreen July 15th 2014, in image (A) and in UTM-coordinates (B). The position of the template is shown in the image, and the magnitude of the calculated velocities indicated by the colour scale, and the direction is indicated by the black arrows in the figure to the right. Two obvious outliers (blue and orange) in the north-east corner are due to the metal pole in the image.*

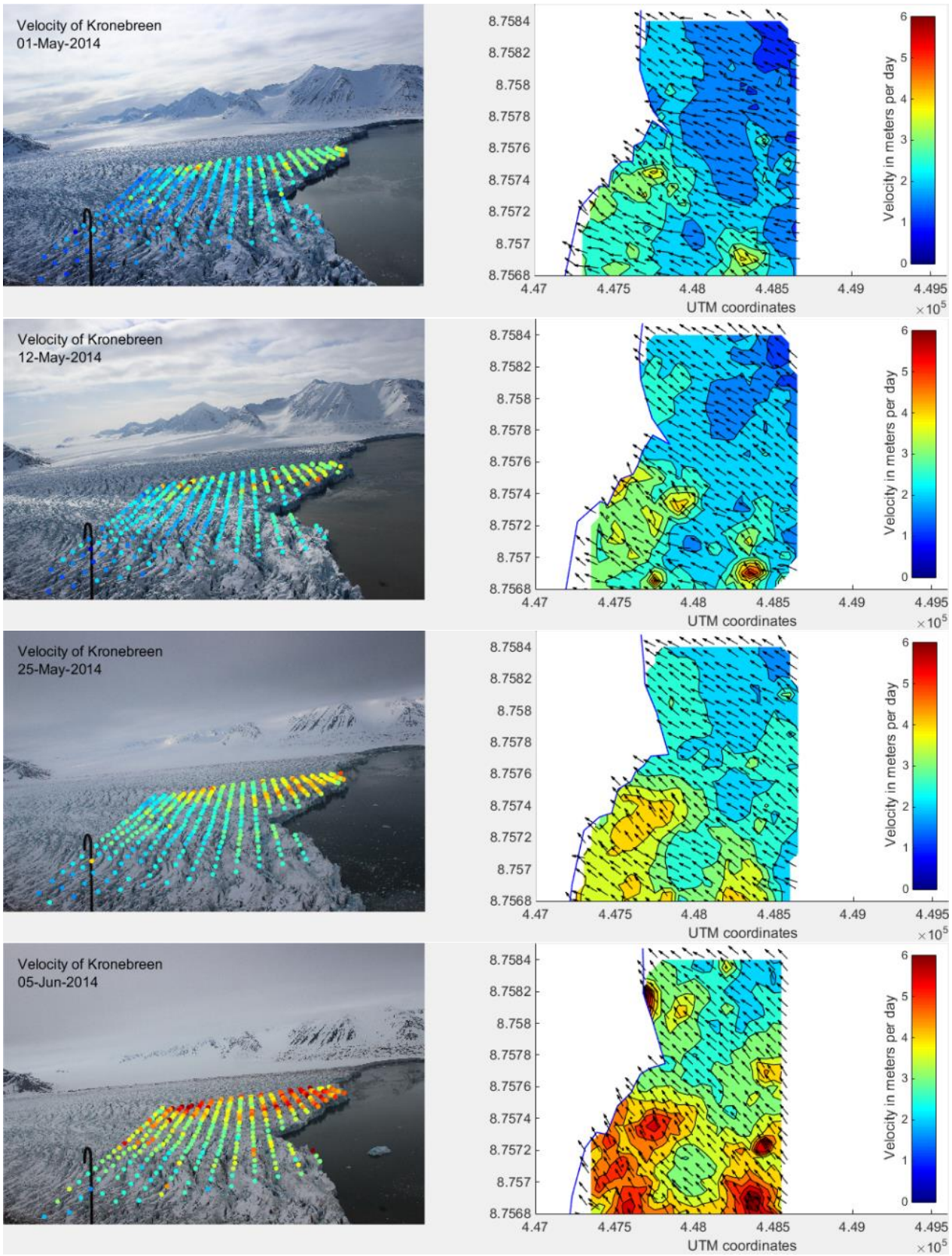
Velocity of Kronebreen
01-May-2014
Velocity of Kronebreen
12-May-2014
Velocity of Kronebreen
25-May-2014
Velocity of Kronebreen
05-Jun-2014
8.7584
8.7582
8.758
8.7578
8.7576
8.7574
8.7572
8.757
8.7568
4.47
4.475
4.48
4.485
4.49
4.495
UTM coordinates
×10^5
Velocity in meters per day
0
1
2
3
4
5
6

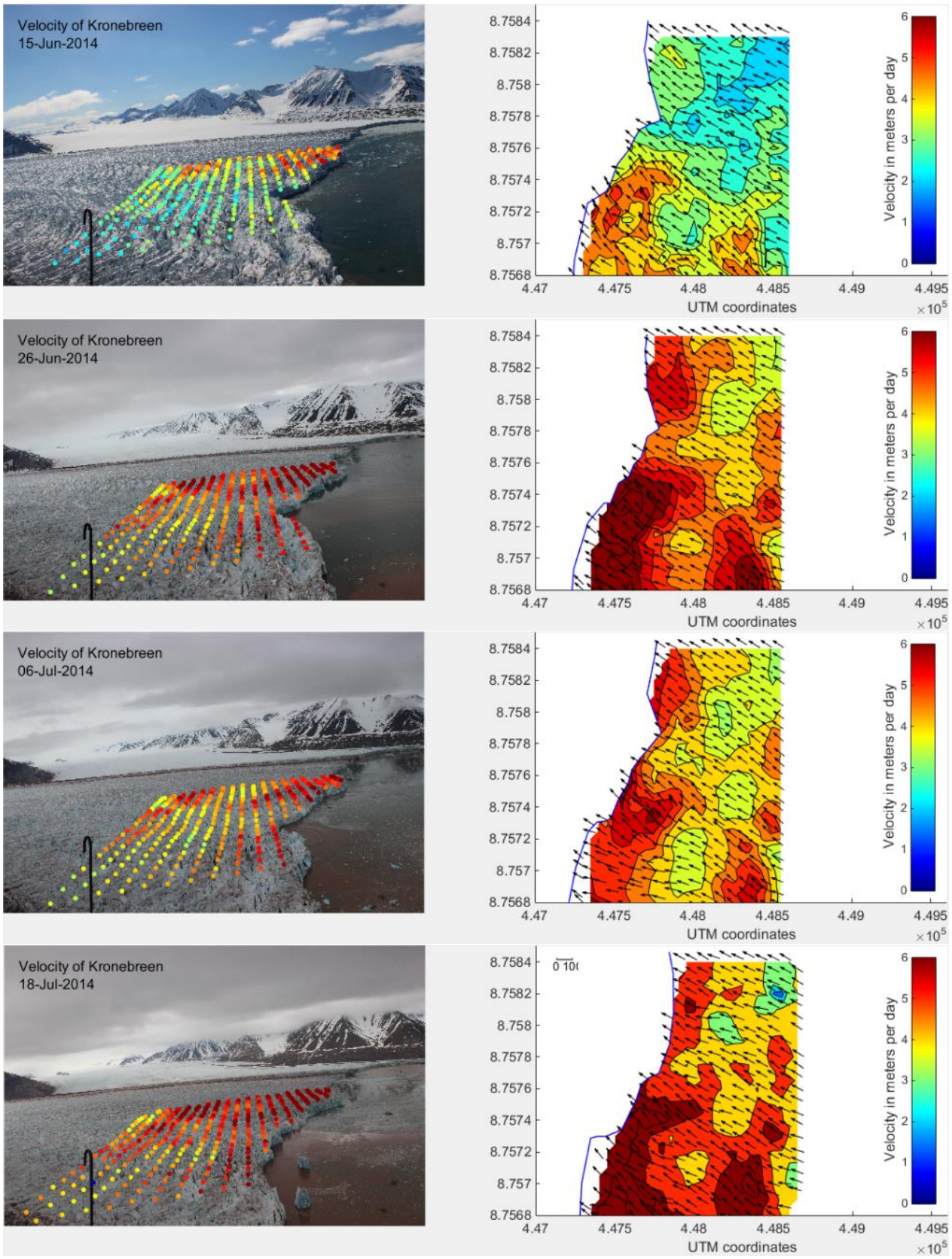
Velocity of Kronebreen
15-Jun-2014
Velocity of Kronebreen
26-Jun-2014
Velocity of Kronebreen
06-Jul-2014
Velocity of Kronebreen
18-Jul-2014
8.7584
8.7582
8.758
8.7578
8.7576
8.7574
8.7572
8.757
8.7568
4.47
4.475
4.48
4.485
4.49
4.495
×10^5
UTM coordinates
Velocity in meters per day
0
1
2
3
4
5
6

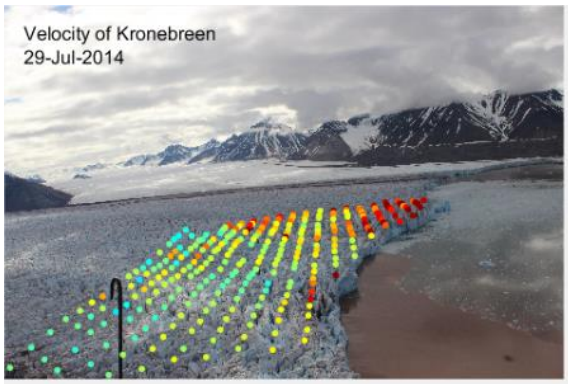
Velocity of Kronebreen
29-Jul-2014

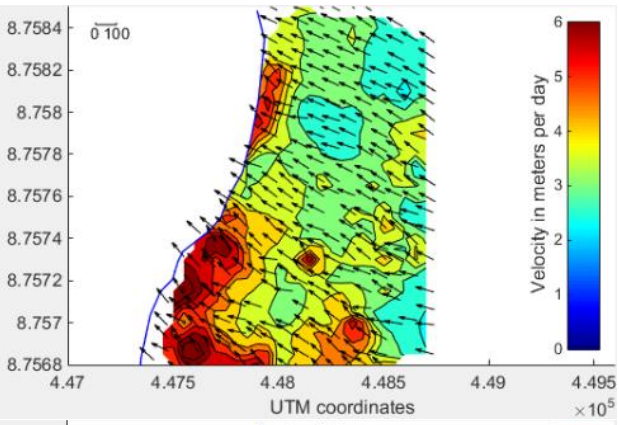
0 100
8.7584
8.7582
8.758
8.7578
8.7576
8.7574
8.7572
8.757
8.7568
4.47
4.475
4.48
4.485
4.49
4.495
×10^5
UTM coordinates
Velocity in meters per day
0
1
2
3
4
5
6

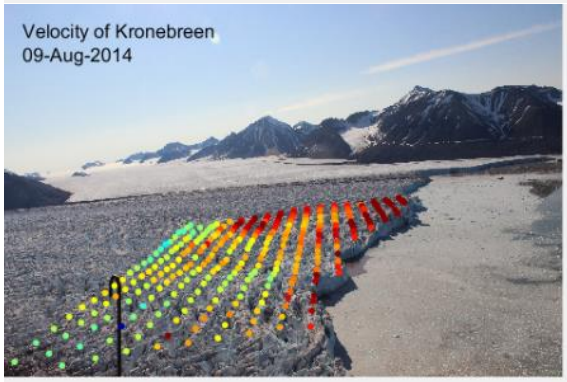
Velocity of Kronebreen
09-Aug-2014

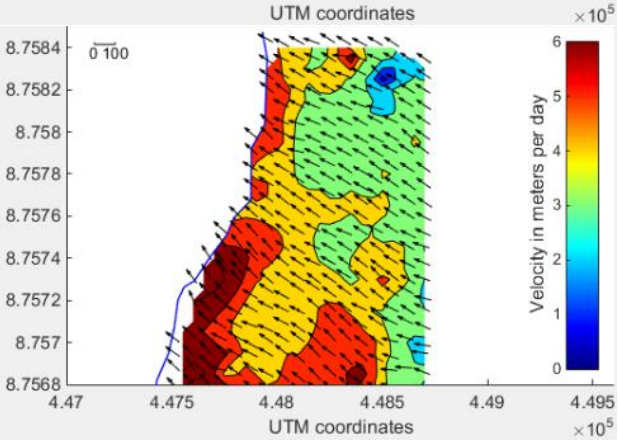
0 100
8.7584
8.7582
8.758
8.7578
8.7576
8.7574
8.7572
8.757
8.7568
4.47
4.475
4.48
4.485
4.49
4.495
×10^5
UTM coordinates
Velocity in meters per day
0
1
2
3
4
5
6

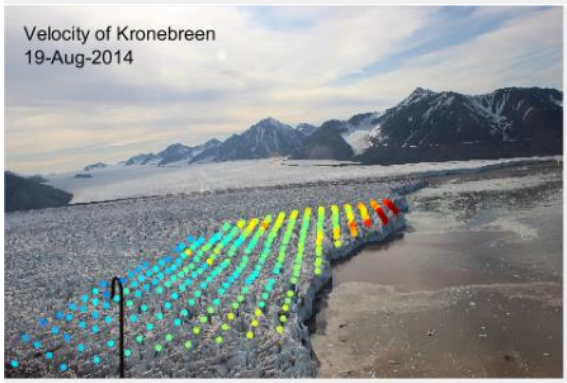
Velocity of Kronebreen
19-Aug-2014

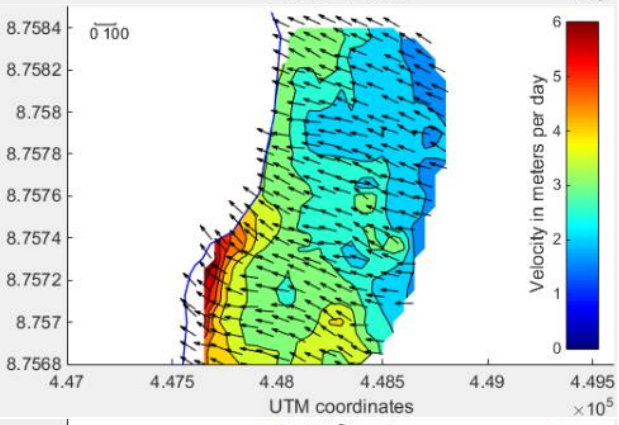
0 100
8.7584
8.7582
8.758
8.7578
8.7576
8.7574
8.7572
8.757
8.7568
4.47
4.475
4.48
4.485
4.49
4.495
×10^5
UTM coordinates
Velocity in meters per day
0
1
2
3
4
5
6

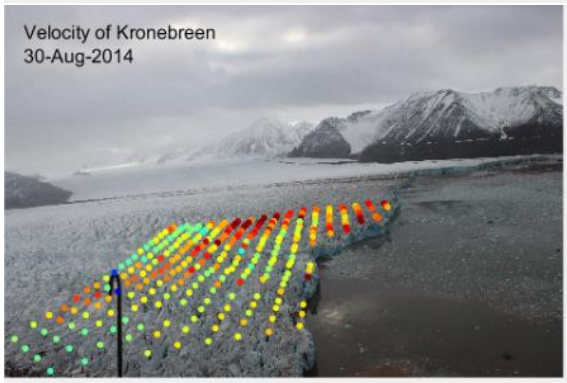
Velocity of Kronebreen
30-Aug-2014

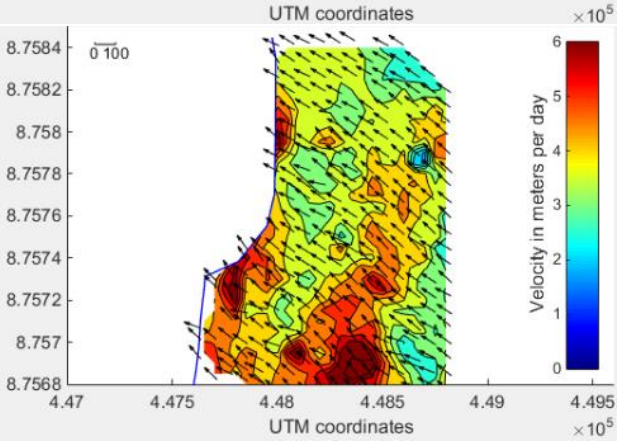
0 100
8.7584
8.7582
8.758
8.7578
8.7576
8.7574
8.7572
8.757
8.7568
4.47
4.475
4.48
4.485
4.49
4.495
×10^5
UTM coordinates
Velocity in meters per day
0
1
2
3
4
5
6

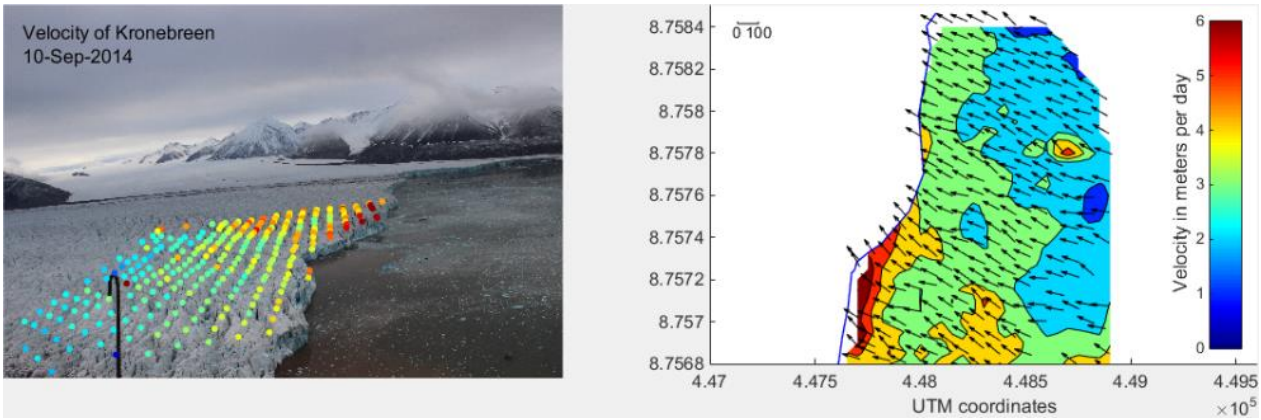

Figure 4.3 *The spatial velocity distribution evolution from May 1st to September 10th 2014 on Kronebreen, calculated from image pairs with 24 hours interval. The coloured dots in the image represent the position of the templates tracked between the two image pairs, and the colour bar represent the magnitude of the calculated velocity. The contour maps (right figures) are based on the real world position of the points tracked. Black arrows indicate the direction of velocity for each point.* All the images are screenshots from the movie attached to this thesis.

Figure 4.3 shows the spatial velocity pattern through the period from May to September 2014. The overall magnitude of velocity increases towards July, but the spatial pattern stays similar through the entire period. The north-west corner is the slowest area. Any transect perpendicular to ice flow show increasing velocities towards the centre line. Any transect parallel to the ice flow show increasing velocities towards the front. A persistent and relatively slow area is found in the middle of the southern part of the tracked area, in all the contour maps. This area is also distinct by the changes in the direction of the velocity arrows. Steep peaks are found in the north-west corner in several maps, indicating apparent steep velocity gradients.

4.1.3 Sensitivity test by changing camera to glacier surface distance

A test to evaluate the sensitivity of the velocity results to a change in DEM surface height and camera height was done by keeping some parameters unchanged and changing others. Pictures taken at 12:00 from June 24th -26th were chosen as data for the test period. During the first run the camera height was set at 387m.a.s.l. and the original DEM was used. In Round 2 the camera height was set to 411m.a.s.l., and the original DEM used. In Round 3 camera height was set to 387m.a.s.l., but the glacier surface of the DEM lowered by 10 metres. During the last round the camera height was set at 387 m and the glacier surface from the DEM raised 10 metres relative to the original. **Table 4.1** shows the result, and the last column calculates the mean % of the four days compared to Round 1.

Table 4.1 *The result from the sensitivity test, and what the parameter values were set to each round.*

Round	Camera height	DEM	Mean velocity June 24	Mean velocity June 25	Mean velocity June 26	Velocity compared to round 1 (24th , 25th , 26th , **mean**) in %			
1	Original	Original	3.09	3.75	4.02	100	100	100	**100**
2	+24 m	Original	3.08	3.71	4.03	99.68	98.93	100.25	**99.62**
3	Original	-10 m	3.22	4.01	3.96	104.2	106.9	98.51	**103.2**
4	Original	+10 m	3.01	3.73	3.86	97.41	99.47	96.02	**97.04**

Figure 4.4 is comparing the velocity contour maps from original DEM to the velocity maps from the raised and lowered DEM surface in the period 24-26 of June. With a lowered DEM the camera-glacier surface distance increases and therefor it is expected that velocities also will increase, and the opposite will happen with a raised DEM surface. This is confirmed by the test, with a lowered DEM surface the velocities increase by 3 % and with a raised DEM surface the velocities decrease by 3 %. A change in camera height of 24 m only affected the velocities by around 0.5 %. The spatial velocity distribution pattern on the glacier surface is still the same during the entire sensitivity test.

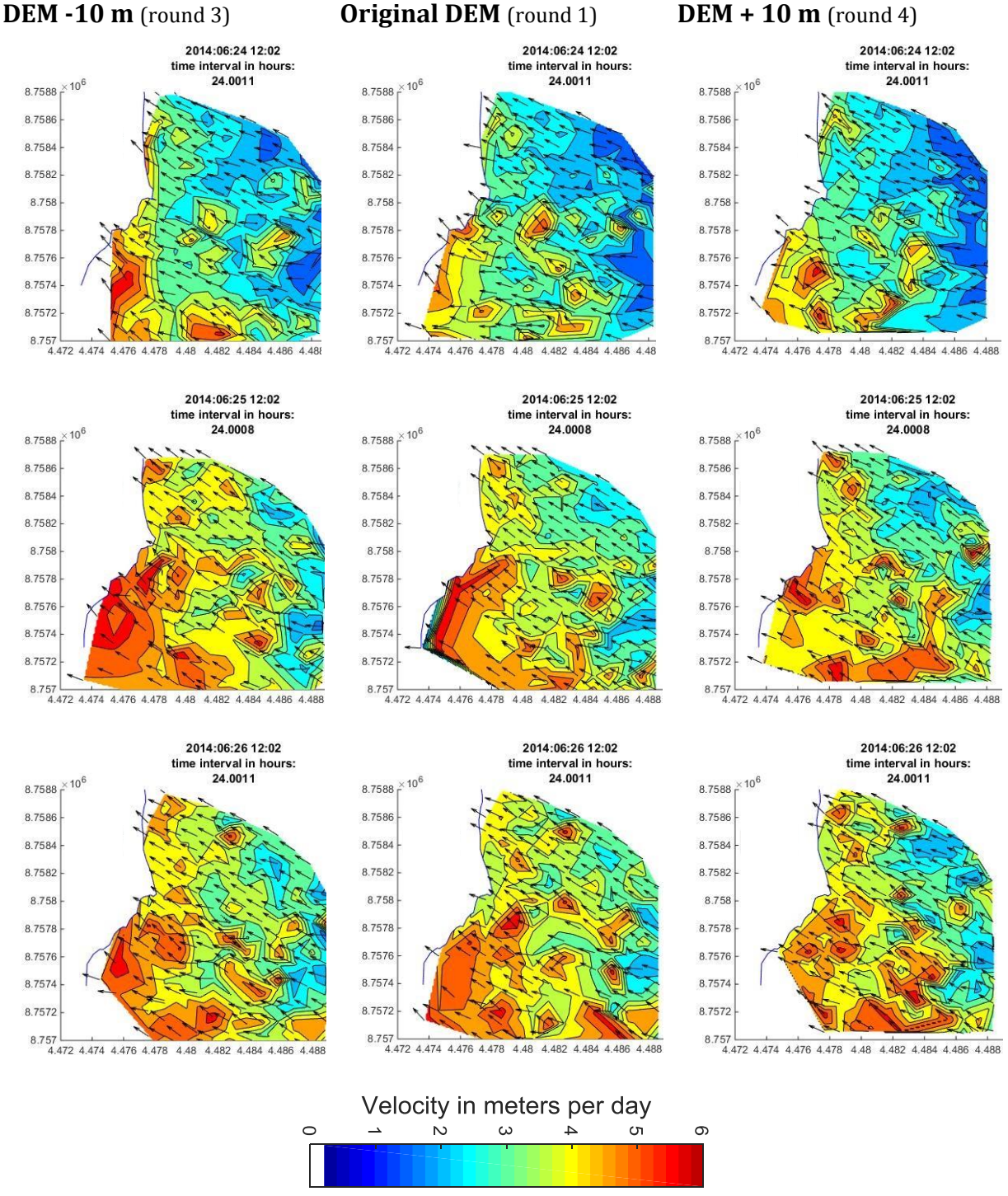

Figure 4.4 *A comparison of velocity contourmaps in UTM units using three different glacier surface DEMs; original, 10 m lowering and 10 m raising. Each row represents a date from June 24th to 26th. Velocity magnitudeis indicated by colour, and direction by arrow.*

4.1.4 Sensitivity test by changing the position of point grid

The points tracked are based on a 75 x 75 metre grid, but how sensitive is the spatial velocity distribution pattern to where the points are located? A test was done to investigate this, by moving the grid 50 m east for test 2 and then 50 m south in test 3 from the same image pairs, and then comparing the results. Pictures taken at 12:00 from June 26-27th were chosen as data for the test period. **Figure 4.5** and **Table 4.2** show the results from the three tests during the two days.

Velocity peaks are recognised in the same location in all the three tests. The distribution of velocity is almost exactly the same in all three tests, with two exceptions (blue velocity lows) in test 2. These two are outliers, and due to the metal pole that is visible in the picture, and affects the feature tracking process. **Table 4.2** shows the mean velocity for each test, compared to the original test and they are all close to 100%.

The conclusion from this sensitivity test is that the method is not sensitive to where the tracked points are located on the glacier, indicating that the well-distributed and relatively dense point grid results in a good representation of the actual velocity pattern on the glacier surface.

Table 4.2 *Comparison of velocities from results from test 1, 2 and 3.*

Test	**Grid position**	**Velocity June 26th**	**Velocity June 27th**	**Compared to Test 1**
Test1	Original	4.07588 m/day	4.5194 m/day	100 % 100%
Test2	Moved 50 m East	4.08339 m/day	4.5122 m/day	100.18% 99.84%
Test3	Moved 50 m South	4.08817 m/day	4.5162 m/day	100.3% 99.93%

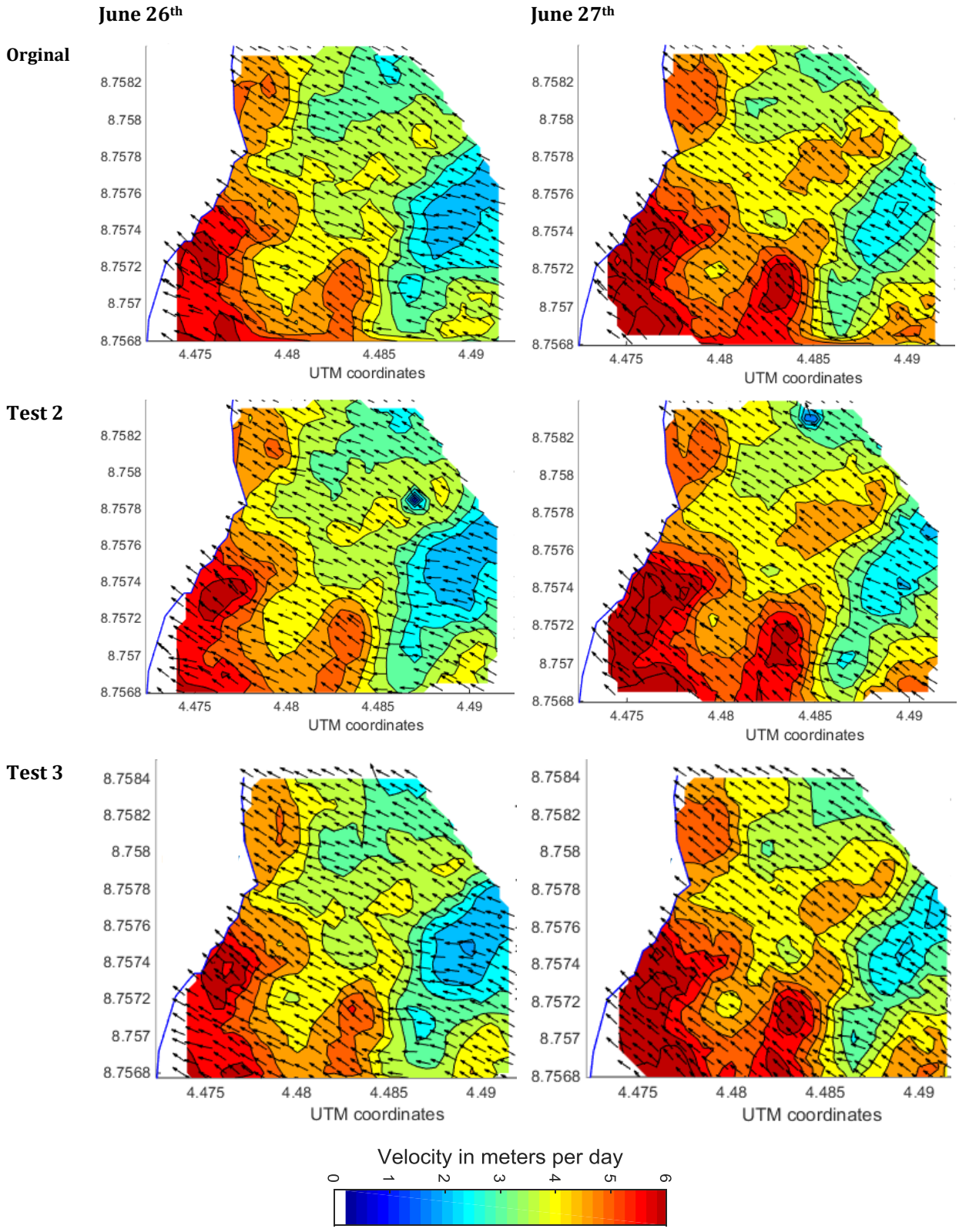

Figure 4.5 *Results from test1 (original)-3. Test1 is the original position of the 75x75 m point grid. In Test2 the grid is moved 50 to the east and in Test3 the grid is moved 50m to the south.*

4.1.5 Comparing to cam1

As another validation of the method, velocity results from the main camera used were compared to results from another camera looking over the calving front. The two cameras have a baseline of approximately 400 m (**Figure 4.6**). May was chosen as the test period. New GCPs were extracted for the new camera, and new parameters were calculated by calibration and using the optimization function in ImGRAFT.

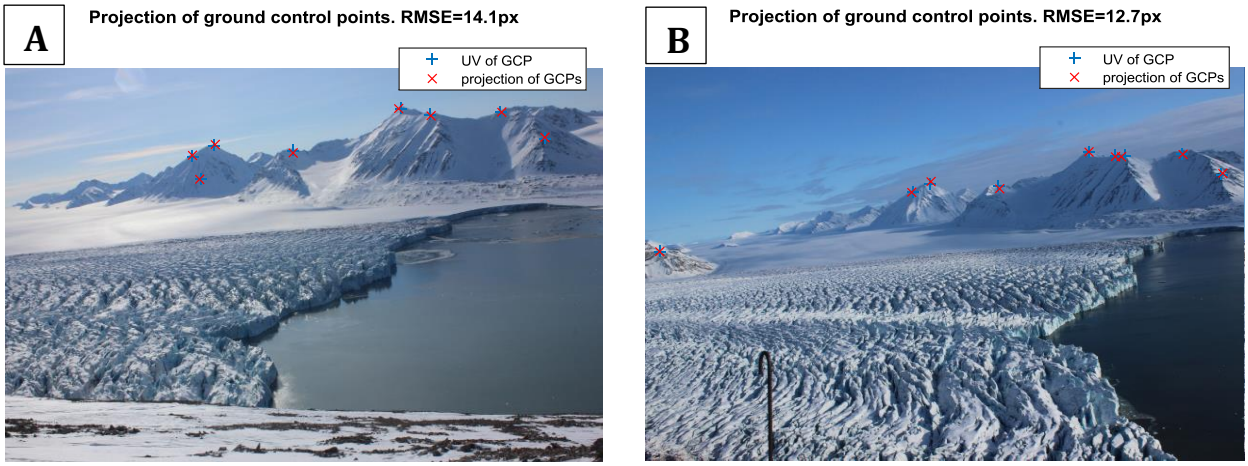

Figure 4.6 *The view from Cam1 (A) and Cam2 (B). Both figures show the position of the uv-coordinates of the GCPs as blue crosses, and the projection of them after optimisation of camera parameters as red stars. The root-mean-square-error of the projection is also plotted.*

Two test days for velocity measurements were chosen, May 2nd and May 8th. Velocities were calculated using the same template size and the same grid size, results are shown in **Figure 4.7**. This figure shows that the spatial velocity pattern is similar, with higher velocity towards the front, and decreasing velocities as one goes from the centre of the glacier to the margin (north). Cam2 covers a larger area of the glacier surface and Cam2s view direction is more perpendicular to ice flow than Cam1. The magnitude of the velocity are not the same, velocities measured from Cam1 are smaller. This shows that the 2-D to 3-D conversion is not correct for one or both of the cameras, most likely due to too few and poorly distributed GCPs in both cases.

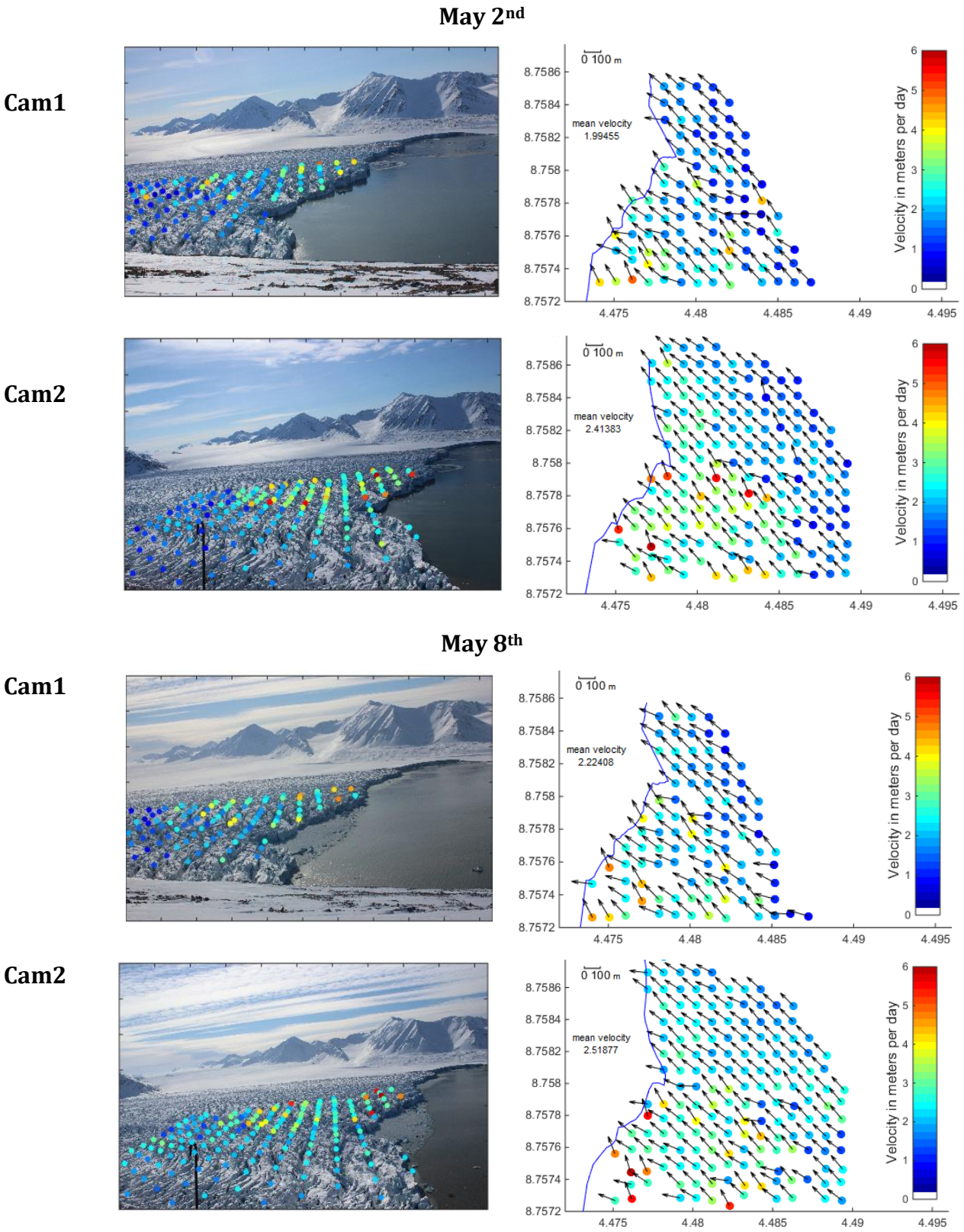

Figure 4.7 *A comparison of velocity results from cam1 and cam2 from May 2nd and May 8th.*

4.1.6 Comparing DEM to TanDEM-x DEM

Most of the results in this thesis were derived using a DEM from a UAV in 2008 with grid cell size of 50x50m. Another DEM was accessible from TanDEM-X imagery in 2013 with grid cell size of 10x10m. Due to this high resolution, the glaciated part of the DEM was smoothed using a Gaussian filter big enough to bridge the crevasses (Messerli and Grinsted 2015) to avoid measuring the wrong distance when converting from 2-D to 3-D (**Figure 4.8**).

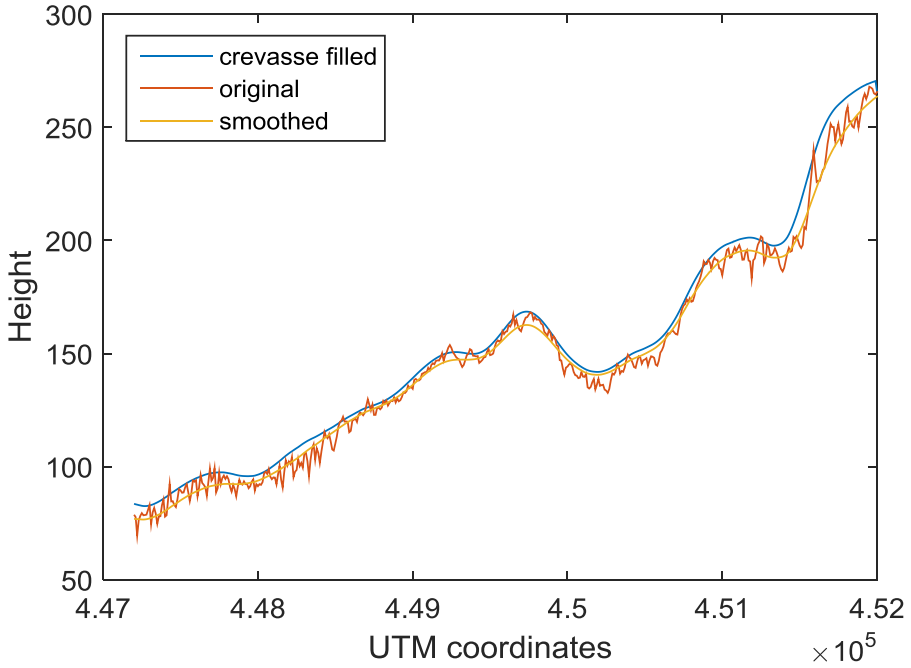

Figure 4.8 *A transect up glacier showing the difference in the DEM surface before and after the crevasses are filled.*

15th, 17th and 18th of July were chosen as the test period. The TanDEM-X DEM results show fewer obvious outliers, and a better resolution and fewer lost points, most likely due to the smoothing of the surface. Velocity magnitudes are very similar. The front positions are not the same, indicating differences in the 2-D to 3-D conversion due to lack of GCPs. This test shows that a higher resolution DEM with filled crevasses will produce better and denser velocity patterns (**Figure 4.9)** and that the method is very dependent on good GCPs to be able to convert properly. For an even better comparison, the UAV-DEM needs to be smoothed.

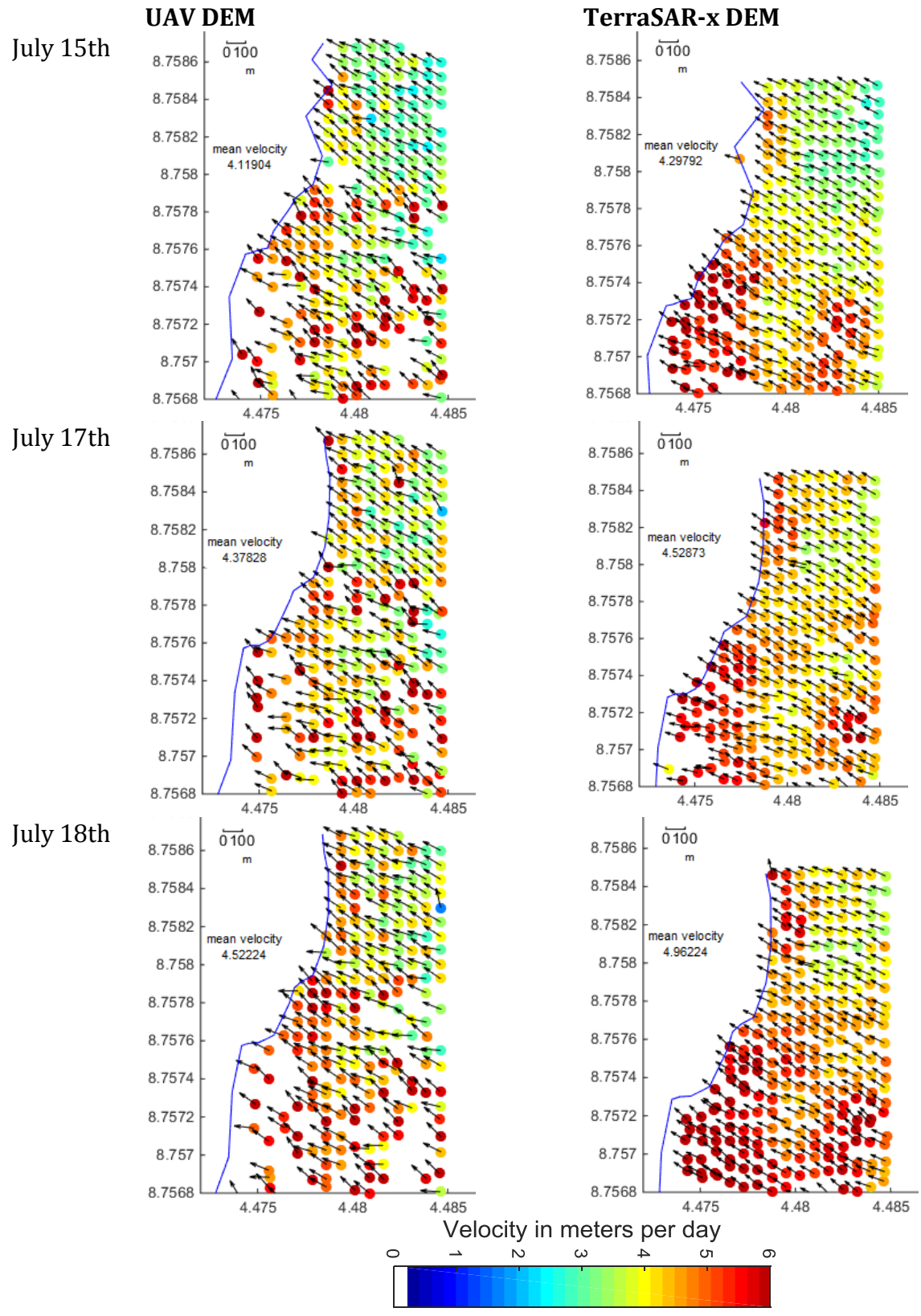

Figure 4.9 *Comparison between velocities derived from two different DEMs; UAV-DEM with a grid cell size of 50x50m and TanDEM-x DEM with a grid cell size of 10x10 m.*

4.2 Front positions

Daily front positions manually plotted in 2D are shown in **Figure 4.10 A**. These front positions were converted into real world coordinates and plotted in a UTM map projection, see **Figure 4.10 B**.

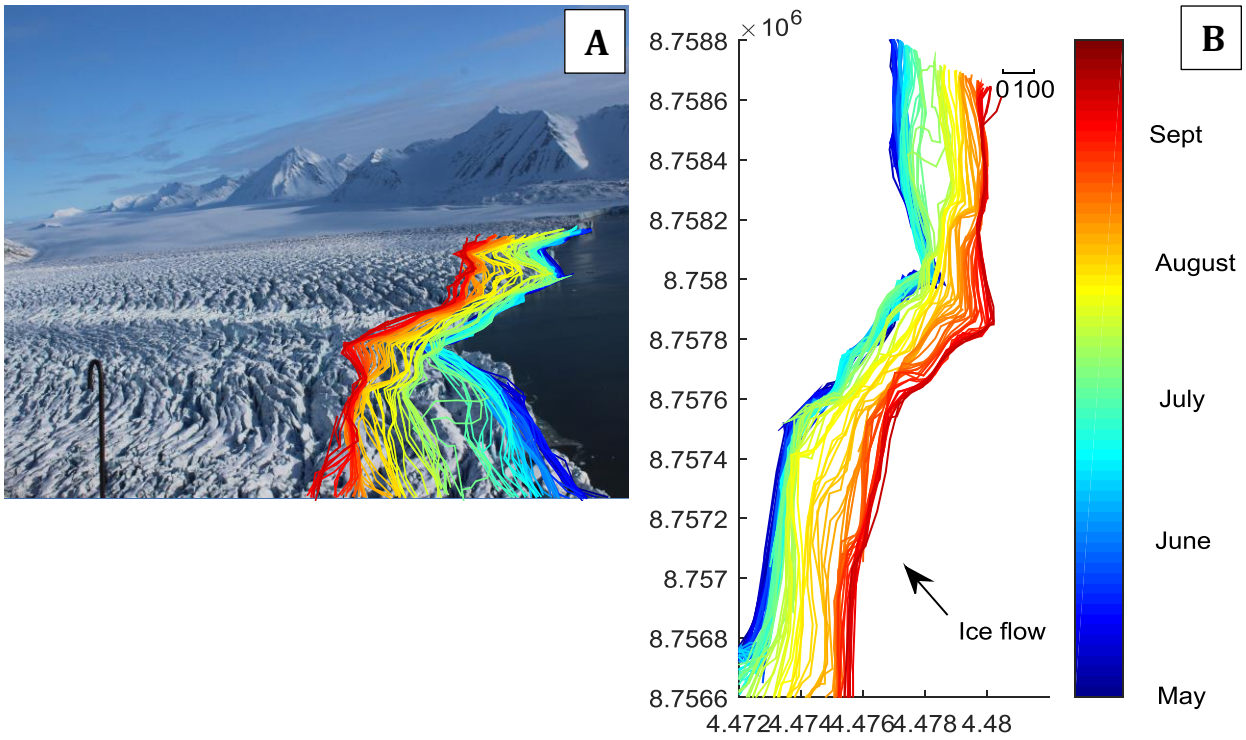

Figure 4.10 *The front positions of Kronebreen at 12:00 close to daily from May 1st to September 15t in image (A) and in UTM coordinates (B). The colours indicate the approximate dates of each front.*

The colours indicate the approximate date for each front position, so as to be able to see the retreat pattern from May 1st to September 15th. The results show a retreat through the entire period, with the exception of an advance in the embayment during June. Bigger calving events are visible as gaps between the lines, seen close to the camera in July. The fastest retreat occurs in late July to the beginning of August. The front positions of the first half of September lie closely together, indicating that the retreat rate has slowed down.

To be able to use the calving front positions for any calculations, points along the front had to be defined. The points were defined as the intersection between a flow line and the front position, shown as stars in **Figure 3.13**. These 11 front points were plotted for each day from May to September colour-coded by the corresponding rectangle (**Figure 4.11)**.

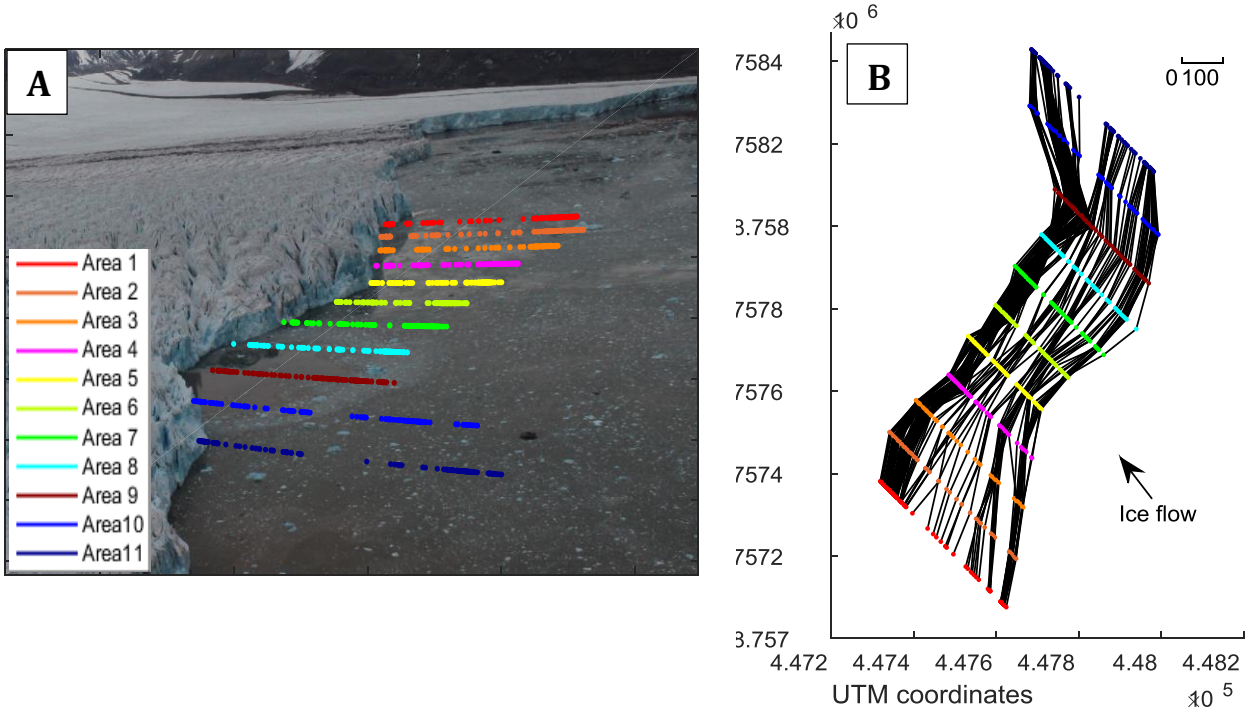

Figure 4.11 *A shows the front points from the 11 areas through the period from May to September plotted onto the last image of the sequence. B shows the plotted front points for each of the 11 areas I UTM coordinates. Larger gaps indicate large calving events.*

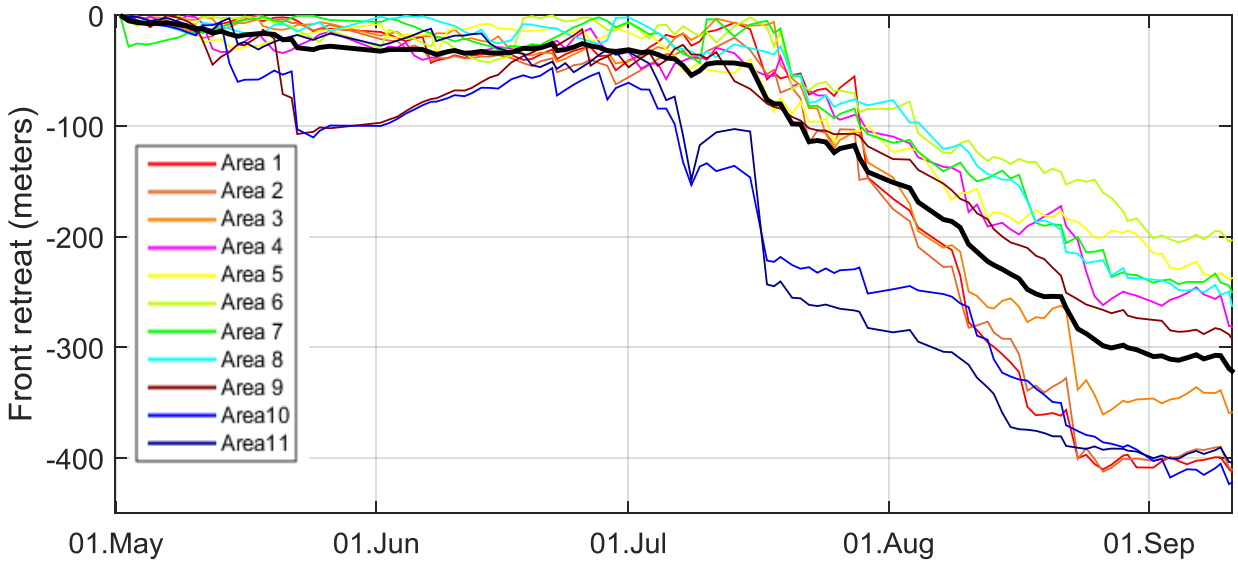

Figure 4.12 *Ice front position for each of the 11 areas from May to September from* ***Figure 3.13.*** *The black line indicates the mean of the 11 values. The blue lines follow a trend of few but larger steps, but most lines have many smaller steps, indicating continuous calving through the period.*

It was then possible to plot the front positions in a time-distance diagram; **Figure 4.12** shows the ice front position for each of the 11 areas of Kronebreen throughout the period. From this graph it is clear to see that the fastest mean retreat starts in mid-July, and continues throughout August before the front stabilises in September. The lines from Areas 9, 10, 11 and 1 have few but large steps, indicating large calving events. After these steps, the front advances. This is not obvious for the other areas, which show a pattern of many smaller steps through the period, and indicates that most of the front undergoes more or less continuous calving from May to September. The cumulative retreat of Area 10 and 11 is caught up by the cumulative retreat of Area 1-3 in August. The total retreat varies from 200 to 419 metres, with a mean of 320 metres.

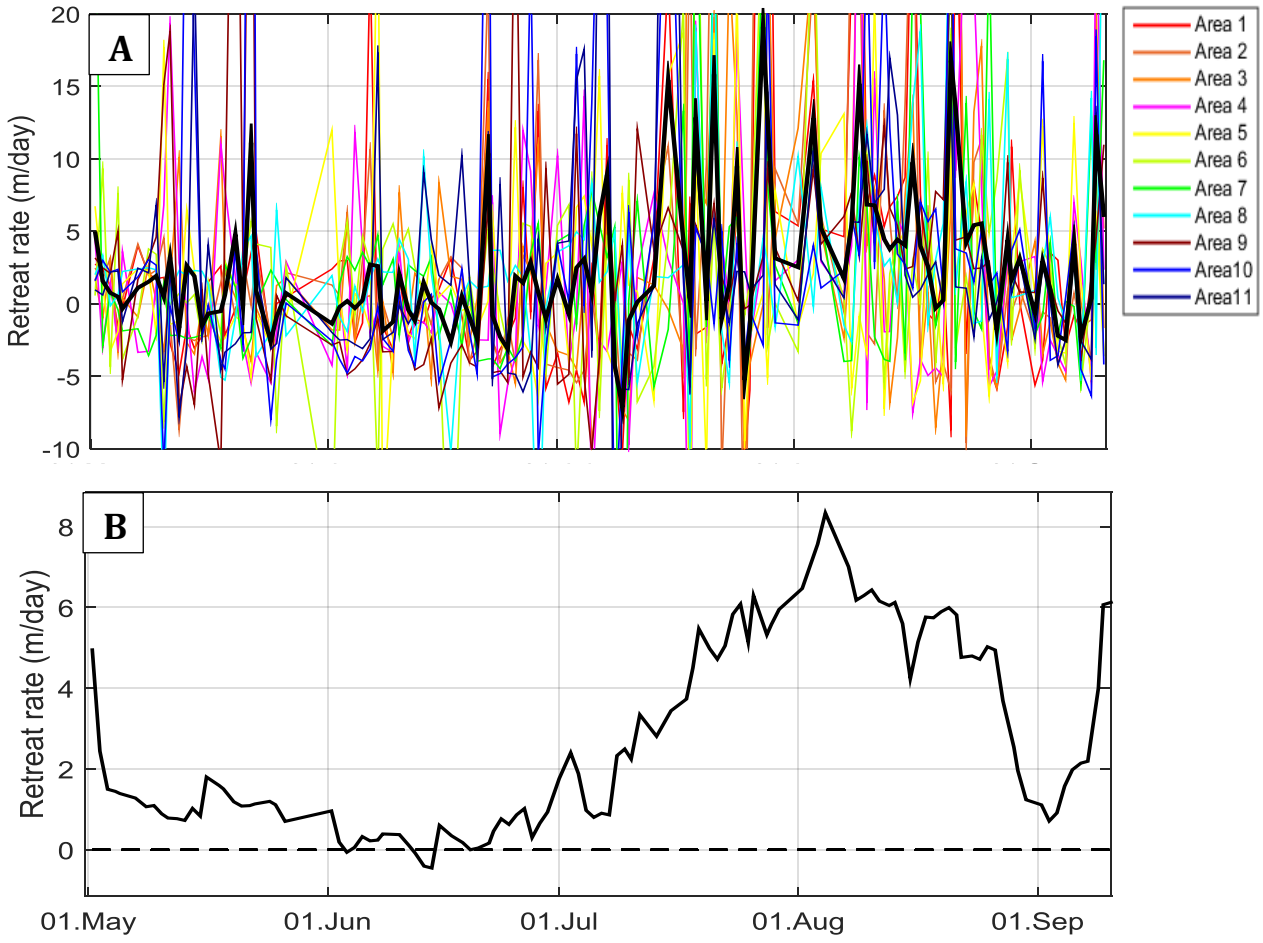

Figure 4.13 ***A*** *shows front retreat rate of Kronebreen from May 1st to September 11th. The coloured lines are the retreat rates from each of the 11 areas (****Figure 3.13****) and the black line shows the mean.* ***B*** *shows mean front retreat rate in m/day of the 11 areas in* ***Figure 3.13*** *from May 1st to Septmber 11th 2014. The signal is smoothed using a moving average filter with a span of 11.*

The front retreat rate through time from May 1st to September 11th is shown in **Figure 4.13 A**. The mean retreat rate varies a lot due to the effect of individual calving events occurring, and the signal needs to be smoothed to show seasonal patterns clearer. **Figure 4.13 B** shows the smoothed front retreat signal using a moving average filter with a span of 11.

4.2.1 Comparing to Cam1

Pixel coordinates of the ice fronts were detected manually for every day of May, and converted to xyz-coordinates using the new camera model for camera 1. All the fronts were plotted together with the fronts of May from the original camera (Cam2). **Figure 4.15** is a plot of the converted front positions from each camera on May 2nd. The difference in the geometry and position is due to different view directions. Particularly the embayment closest to the cameras is projected differently, because it is not possible to see the "end" of the embayment from Cam 2, and therefore not possible to plot the uv-coordinates correctly.

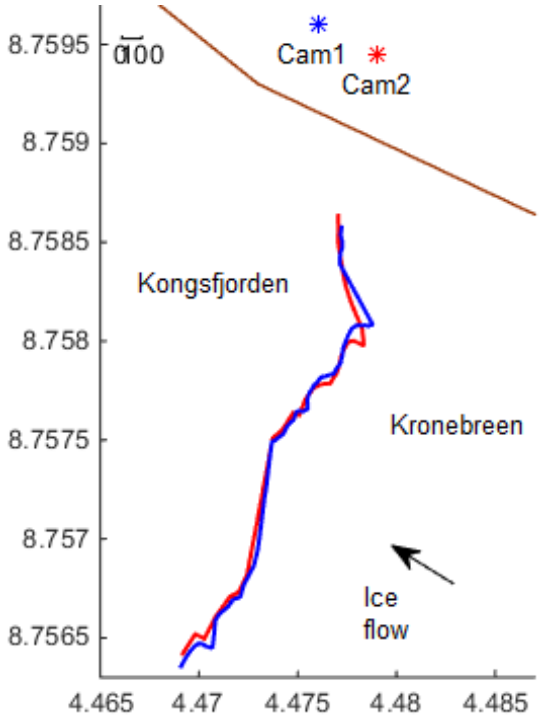

Figure 4.14 *Two clearly separated sets of front positions from May 2nd, generated by converting uv coordinates into xyz coordinates. The red indicate the front generated using camera parameters from Cam 2, and the blue is from Cam 1.The axes are UTM coordinates.*

4.3 Calving rates

Calculation of calving rates was based on the sum of the retreat rate and the velocity for each of the 11 areas, shown in **Figure 4.15 A**. High calving rates occur in May with values of more than 14 m/day on one occasion. Beginning- to mid-June has calving rates of around 3 m/day, before it increases towards the end of the month to values of 10-14 m/day. Early August has the highest calving rates, with several peaks above 20 m/day. September has values around 5 m/day. The last days in the period have a calving rate peak of 15 m/day. The signal is very variable and smoothing of the data is necessary to better show seasonal patterns. **Figure 4.15 B** shows the smoothed calving rate signal using a moving average filter with a span of 11.

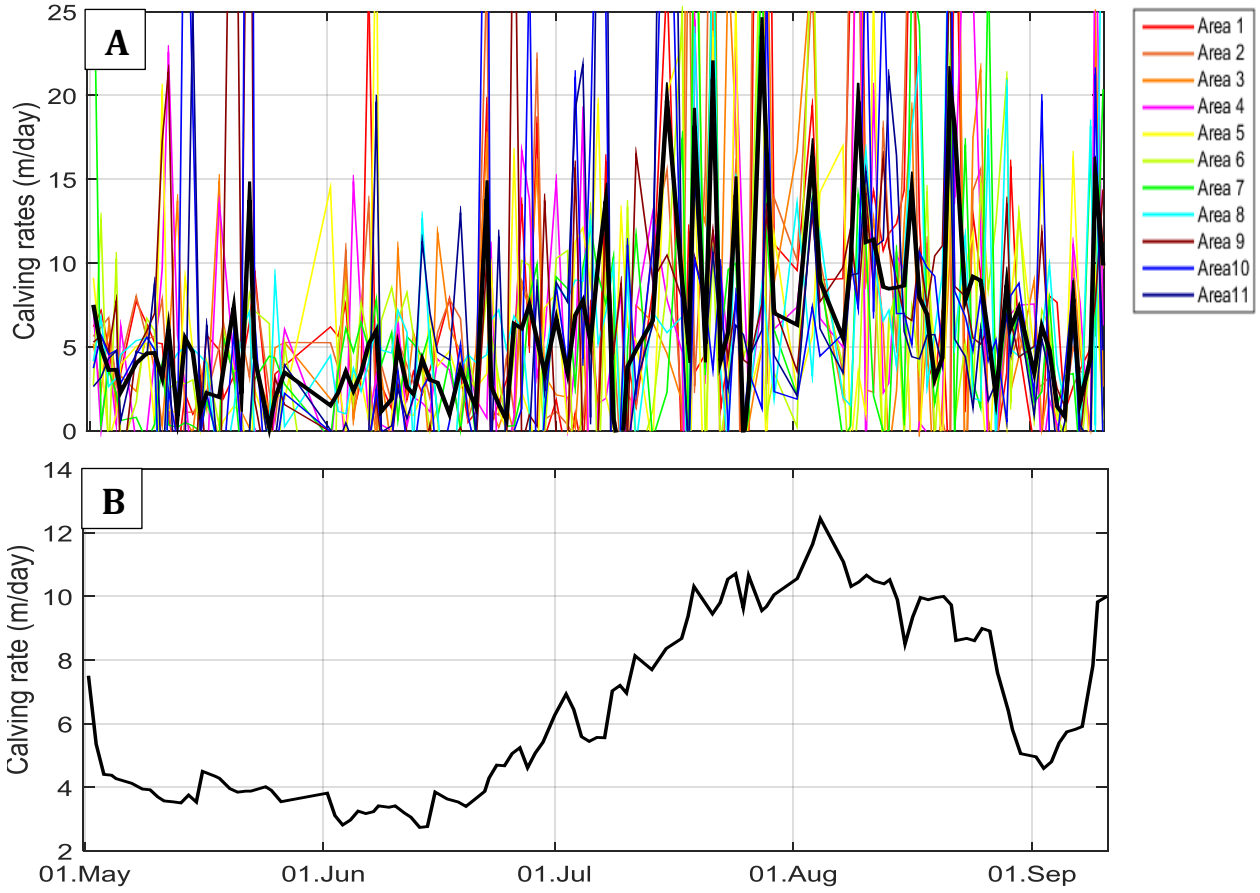

Figure 4.15 ***A*** *shows calving rate from each of the 11 areas based on daily mean velocity and mean front retreat rates for the same 11 areas of Kronebreen from May 1st to September 11th. The black line is the mean calving rate from the 11 values for each day.* ***B*** *shows the smoothed mean calving rate signal using a moving average filter with a span of 11. The x-axes are the same.*

4.4 Individual calving events

To find out more about the nature of the calving at Kronebreen, 6 larger individual calving events were investigated (**Figure 4.16**). They occur from mid-June to mid-August, and all events are located on either side of the embayment where Area 9 is. The first event occurred when the glacier was starting to accelerate, the four next when the highest speeds were measured and the last occurred at the velocity peak in August. All the calving events are sub-aerial and can be predicted from the images immediately prior in the sequence because the blocks of ice are isolated on either side and lose support.

In the five last events melt water plumes are visible in the area due to the reddish colour, and they emerge on either side of where the ice detached. One persistent meltwater plume emerged in the embayment around Area 9 from late June and throughout August. Smaller meltwater plumes emerge on either side of the large plume, but are not that persistent in position along the front. The four first events correlate with peaks in the calving rate graph (**Figure 4.15**), the last two events don't.

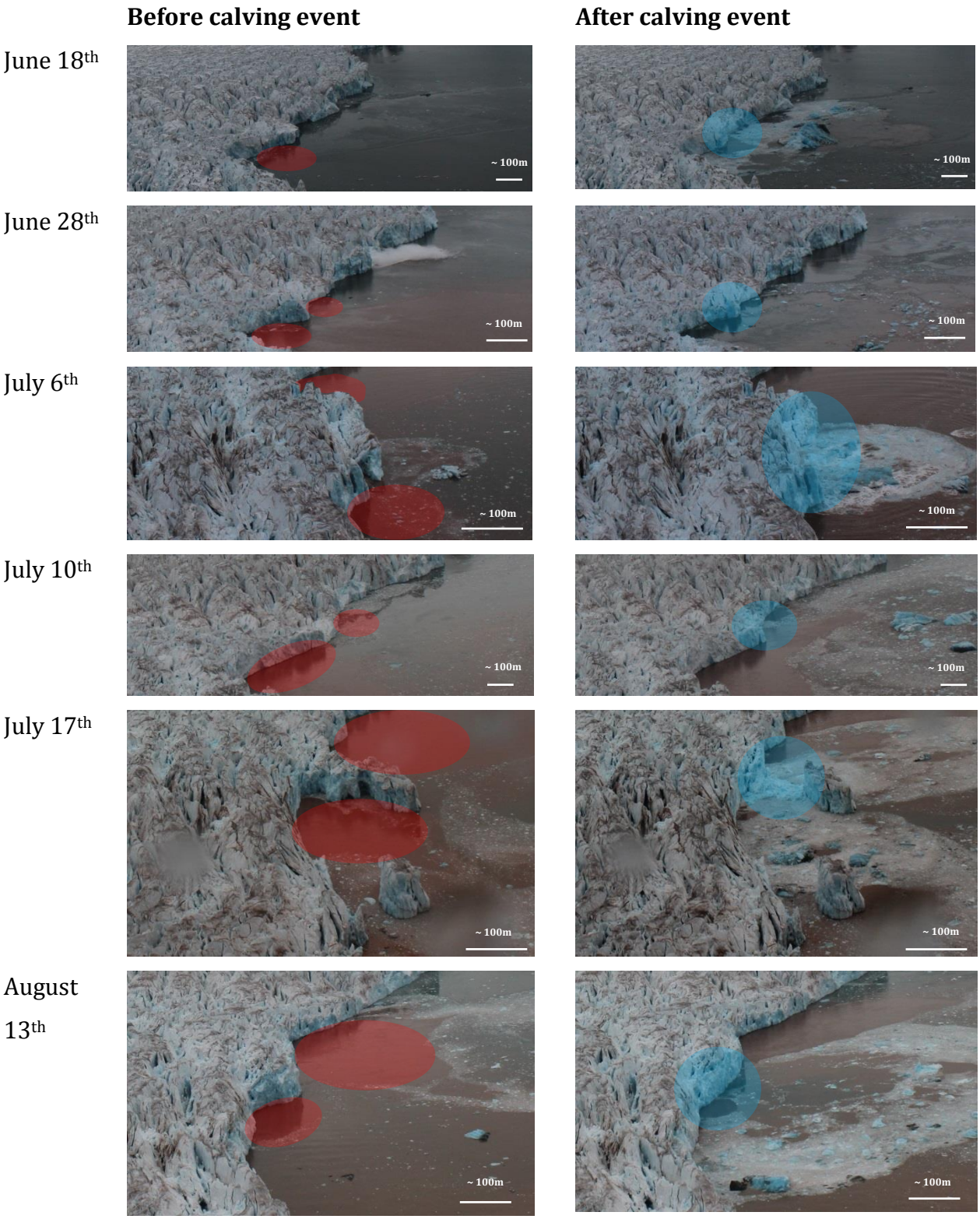

Figure 4.16 *Dates and pictures before and after the six investigated large calving events. The images have an interval of 30 min and the scale is very approximate since it will vary within the image. The blue areas indicate where the ice detached and the red indicate plumes. All the calving events were sub-aerial.*

4.5 Film with results

To present the evolution of both the velocity and the front positions through the period, a movie was made, including the daily spatial velocity distribution in both image and UTM coordinates, and a graph with the velocity and front position over time (**Figure 4.17**). The red dot in this graph indicates the timing of the present velocity map and image, and will therefore move to the right. The same colour-coding used in the image, the velocity graph and the contour map is shown in the colour bar in the upper right corner. The movie shows how well the method works with different images, and where the velocity graph is not as trustworthy.

The movie can be found by following this link:
https://www.dropbox.com/s/ki7mct17ie36j8x/velocityfigure_fast.avi?dl=0

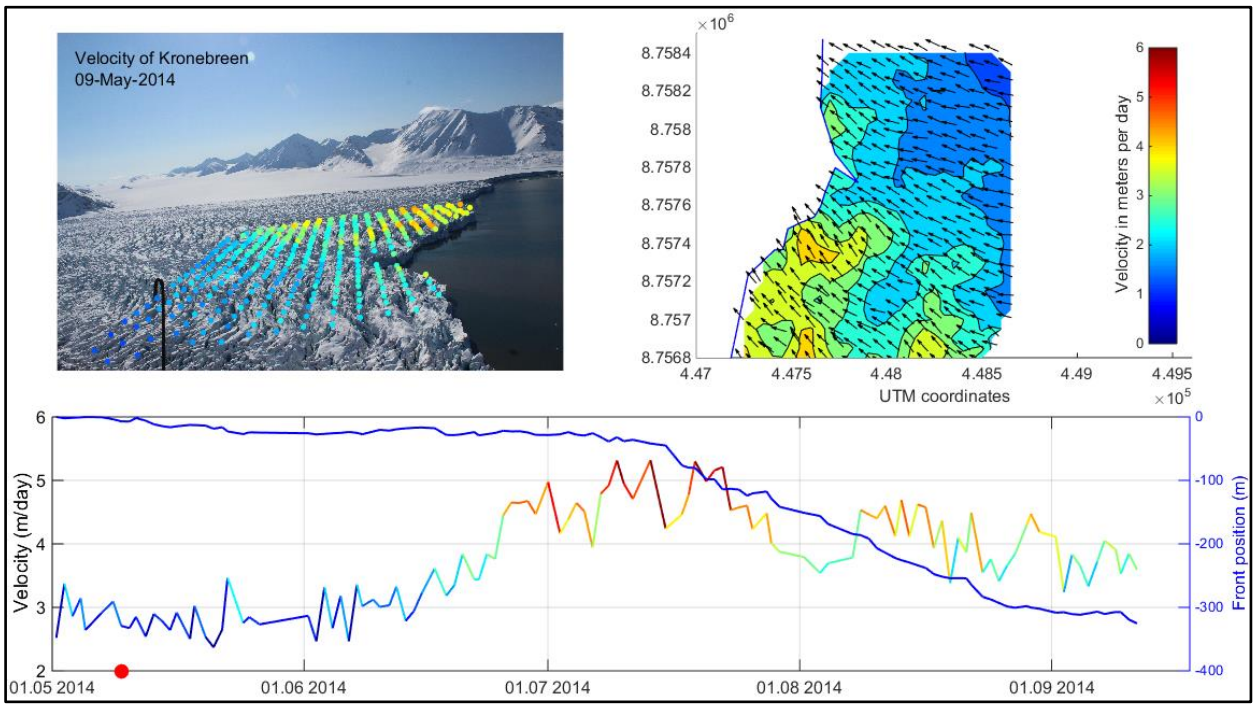

Figure 4.17 *A screenshot from the movie attached to this thesis, including the daily spatial velocity distribution in both image and UTM coordinates, and a graph including the mean frontal velocity and front position over time. The red dot in this graph indicates the timing of the present velocity map and image. The colours in the image, the velocity graph and the contour map belongs to the colour bar in the upper right corner. The actual velocity line has colours that represent the mean velocity for the time period between the two image pairs.*

5 Discussion

This thesis aims to develop techniques to measure glacier surface velocities, front positions and calving rates in more detail, using terrestrial photogrammetry. Daily images from the tidewater glacier Kronebreen were used to describe the nature of calving at this particular tidewater glacier during May to September 2014. The results are evaluated both by comparing them to previous results from the glacier and also corresponding satellite derived results from the same period. The observed patterns are discussed in relation to meteorological data from the same period.

5.1 Velocities

The surface velocity increased throughout June from 3 m/day to almost 5 m/day. Maximum velocities of 5.3 m/day were reached in mid-July, and another peak of 4.7 m/day occurred in mid-August. The spatial pattern was consistent throughout the period, with higher velocities towards the front and the centre of the glacier.

The digital elevation model (DEM) used is not up-to-date, and the magnitude of ablation is uncertain. The sensitivity test of the velocity results by raising and lowering the DEM surface of the glacier by 10 m showed a ± 3 % deviation in velocity from the original DEM. This is more or less exactly as would be predicted given the camera height. The key thing is that the differences are relatively small, consistent and the overall velocity patterns in time and space persist. 7 m of ablation was accounted for, but the actual ablation is not certain. The further ablation during the time-lapse period was not accounted for. In the field campaign in May 2015 it was clear to see surface lowering from the year before.

The cameras have an internal clock, and it is a known phenomenon that they do not necessarily run at exactly the right speed; clockdrift (Welty et al. 2013). The Digisnap timer was programmed to make the cameras take images every 30 min. The first image used in this project was, according to the internal camera clock, taken 01.05. 11:58, and the last 16.09. 12:07 indicating a clock drift of 9 minutes in the period of 139 days, or 3.9 s/ day.

To calculate the velocity, the time difference between the images can be retrieved from the metadata from the image the individual .jpeg files. The observed 3.9s a day clock drift will not cause a significant error, even at high temporal resolution velocities, i.e. short time between images.

In some image pairs the direction of the velocity (shown with black arrows in velocity maps) changes abruptly from day to day maps of velocity. The change is not significant, but it indicates a possible error in the method. One reason for this could be camera motion. The camera shake is resolved for, but an error in this part of the script can due to bad visibility of the mountains induce an apparent change in velocity direction. Another explanation can be tidal effects on the glacier that can affect the height of the glacier surface. Even though most of the velocities calculated are based on imagery taken at the same time every day, the tidal cycle is around 12 hours and 25 minutes which means a shift in the tidal phase or almost 1 hour per day. According to www.sehavniva.no the largest tidal change is 150cm above ocean chart zero. This will induce a maximum underestimation of the velocities of 0.38%, if it is affected at all. However, since the front of Kronebreen is grounded (Sund et al. 2011), the elevation of the frontal part of the glacier surface should not be affected by tidal variations at all.

Velocity measurements are also filtered based on signal-to-noise ratios and averaged spatially, which decreases the errors. A super sampling factor of 3 was used in the template match process to obtain sub-pixel precision. Camera motion was accounted for by template matching of static features in the image view, and lowering of the glacier surface as a result of ablation was also accounted for. A sensitivity test confirms that an error in the DEM surface (ablation) would not affect the velocity results much. Comparison with another terrestrial camera increases the credibility of the method. The velocity graph (**Figure 4.1**) derived in this study shows that all the 11 areas closely follow one another and so therefore also does the mean velocity, which is an indication of high quality results.

The seasonal pattern of average velocities, which increased in June, peaked in July and decreased in August, match very well the overall air temperature during the period. Meteorological data from the station in Ny-Ålesund is freely available from The Norwegian Meteorological Institute. Mean daily air temperature and daily precipitation data was plotted on the same x-axis as the ice velocity calculated, see **Figure 5.2**

The temperature was low and below 0 °C until June, but when temperatures reached above 0 °C most of June, the acceleration of the glacier starts. During the summer, several of the temperature peaks correspond well with velocity peaks, and after big temperature lows there is evidence of short slow-downs of the glacier too. Similarly, most of the rain events through the period correspond with a peak in velocity shortly after or during (see blue areas in **Figure 5.2 B**). This suggests that the velocity has an atmospheric forcing from air temperature and rain events. Higher air temperature and rain result in more water input in the glacier system and the base of the glacier is then potentially lubricated which in turn can lead to less basal friction and higher velocities (Zwally et al. 2002).

The jagged and irregular character of the time-velocity graph may reflect other short term controls on the velocity. The temperature graph has similar jagged appearance, and short term variations may be explained by short term variations in temperature. Another explanation may be the shift in tidal phase of around 1 hour per day. Tidal influence on calving glaciers velocity has been shown by Marsh et al. (2013).

As another evaluation of the results, they were compared to TerraSAR-X results (Luckman et al. in review) from the same time period. The TerraSAR-X imagery has a time interval of 11 days in the image pairs and therefore the results from the daily terrestrial time-lapse imagery were averaged over the same time interval (**Figure 5.3**). A list of the dates of the TerraSAR-X imagery is found in **Appendix 6**.

The velocity results from the two datasets are different in both magnitude and pattern in May. In June both the satellite and terrestrial dataset show a steady increase from 2-3.5 m/day and 3-4.5 m/day respectively. The TerraSAR-X results have one peak occurring in beginning of July and a second larger one in the beginning of August. The terrestrial dataset

has maximum values in mid-July and a smaller peak in mid-August. The largest peak in the satellite dataset coincides with a velocity low in the terrestrial dataset. Both datasets show a decrease at the end of August. The highest velocities calculated are close to 5 m/day in the satellite dataset, and the same for the terrestrial.

The very different intervals between the image pairs used can partly explain the differences in the results. The DEM used is not the same either, which also may results in differences. The results from this thesis are based on 11 flow lines with 100 m spacing along the front. This only makes up 1.3 km of the total 3 km front. The satellite derived results are based on 30 flow lines with 100 m spacing along the front, and result in a better spatial coverage. The differences in the two datasets may indicate a loss of information in the satellite derived results due to low temporal resolution compared to the resolution obtained by the terrestrial results.

Sund et al. (2011) and Eiken and Sund (2012) investigated velocity and the calving front of Kronebreen June 3rd – August 3rd 2008 using two SLR cameras programmed to take photos every 6 hours, located at the same positions as Camera 1 and 2 used in this thesis. They had the opportunity to do both monoscopic and stereoscopic measurements. Due to large error estimates when measuring velocity stereoscopically (short base and long distance), they decided to use only the depth measurements from the stereo view and do the tracking of nine targets to determine velocity using imagery from a single camera. In addition they reduced the errors by averaging their data temporarily. Sund et al. (2011) found daily displacements of 1.4 -3.8 m/day and several velocity peaks correlated with rain and high temperature events. These velocities are smaller in magnitude than the mean velocity results derived in this thesis, but close to the velocities from area 10 and 11. Only 9 points were used to estimate the velocity and they may not be representative for the entire glacier, and this may explain why the results from Sund et al. (2011) do not match the results from this thesis.

Kääb et al. (2005) used image matching techniques on ASTER imagery and calculated maximum speeds of more than 800m/year (2.2 m/day) just above the calving front of Kronebreen around July 2001 (**Figure 2.9**). The time interval between the images used was

40 days. Peak velocities retrieved from the time-lapse data in July are higher than what Kääb et al. (2005) found. Differences can be explained by the very different time interval, the results are from 13 years ago, and this thesis has not measured the entire cross section of the glacier which excludes the slower flowing part towards the other margin.

Svanem (2010) measured velocities of Kronebreen with a 4 day resolution using oblique terrestrial photogrammetry, as part of her master thesis. Velocities of 2.5 m/day were found in May and peak velocities occurred in mid-July and August with values around 6 m/day, which match very well with the velocities retrieved in this thesis. During the same field campaign Rolstad and Norland (2009) used ground-based high-range resolution interferometric radar and calculated velocities of 2.5 m/day in August/ September. This is much lower velocities compared to the time-lapse velocities presented here, and may be explained by the fact that these results are from other places on the glacier surface.

Liestøl (1988) reported velocities up to 4 m/day, which is not far off the peak velocities derived in this thesis.

Köhler et al. (2012) measured the velocity 2 km up from the front position of Kronebreen, averaged over 3 days using a single code based GPS from May to November in 2009 and 2010. In 2009 the velocities were stable around 1.5 m/day in May to mid-June, and then accelerated to 3.5 m/day at the end of July. A peak of 2.3 m/day occurred in late August. In 2010 a similar acceleration occurred in June and the highest velocities were reached early July and another peak in August. Both these years have very similar patterns as the velocity calculated in this thesis, but the magnitudes are smaller. This is expected since the velocities calculated here are much closer to the front, and acceleration towards the front has been shown.

The spatial velocity distribution over the area investigated in this thesis shows more or less the same pattern throughout the period from May to September. The relatively slow north-west corner is the area closest to the margin towards Collethøgda and will naturally be slowed down due to friction; lateral drag. Therefore increasing velocities perpendicular to

the ice flow towards the centreline is also natural. The acceleration towards the front is a common phenomenon on tidewater glaciers, explained by reduced resisting forces when the terminus reaches the water body (Appendix 1; van der Veen 2013; Benn and Evans 2010; Vieli et al. 2004).

The few steep velocity peaks in the north-west corner are caused by template matching of the metal pole in the image. The persistent slow area in the south, closer to the front, can be explained by bed topography forcing the glacier to flow slightly uphill here. This corresponds very well with a bump in the bed DEM (**Figure 5.1**) (Nuth et al. 2015).

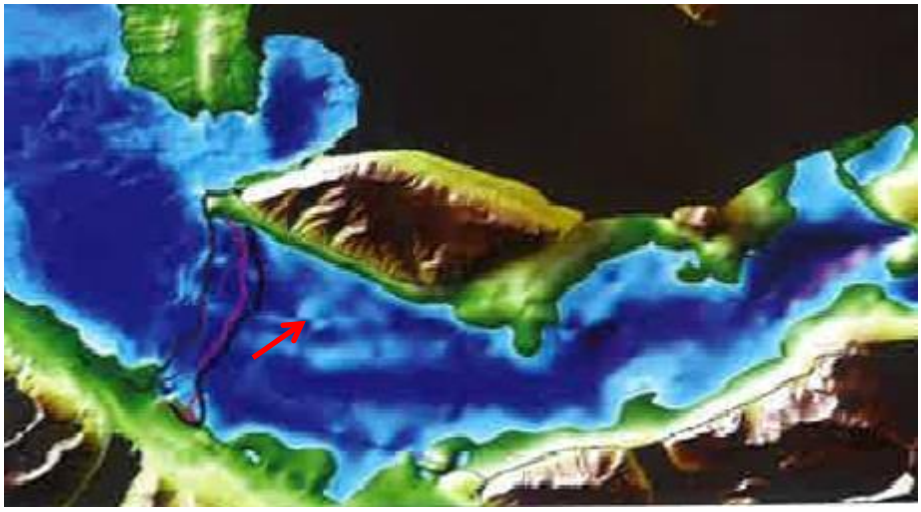

Figure 5.1 *Bed topography under Kronebreen, which shows a bump (red arrow) under the investigated area, corresponding with slow surface velocities (Nuth et al. 2015).*

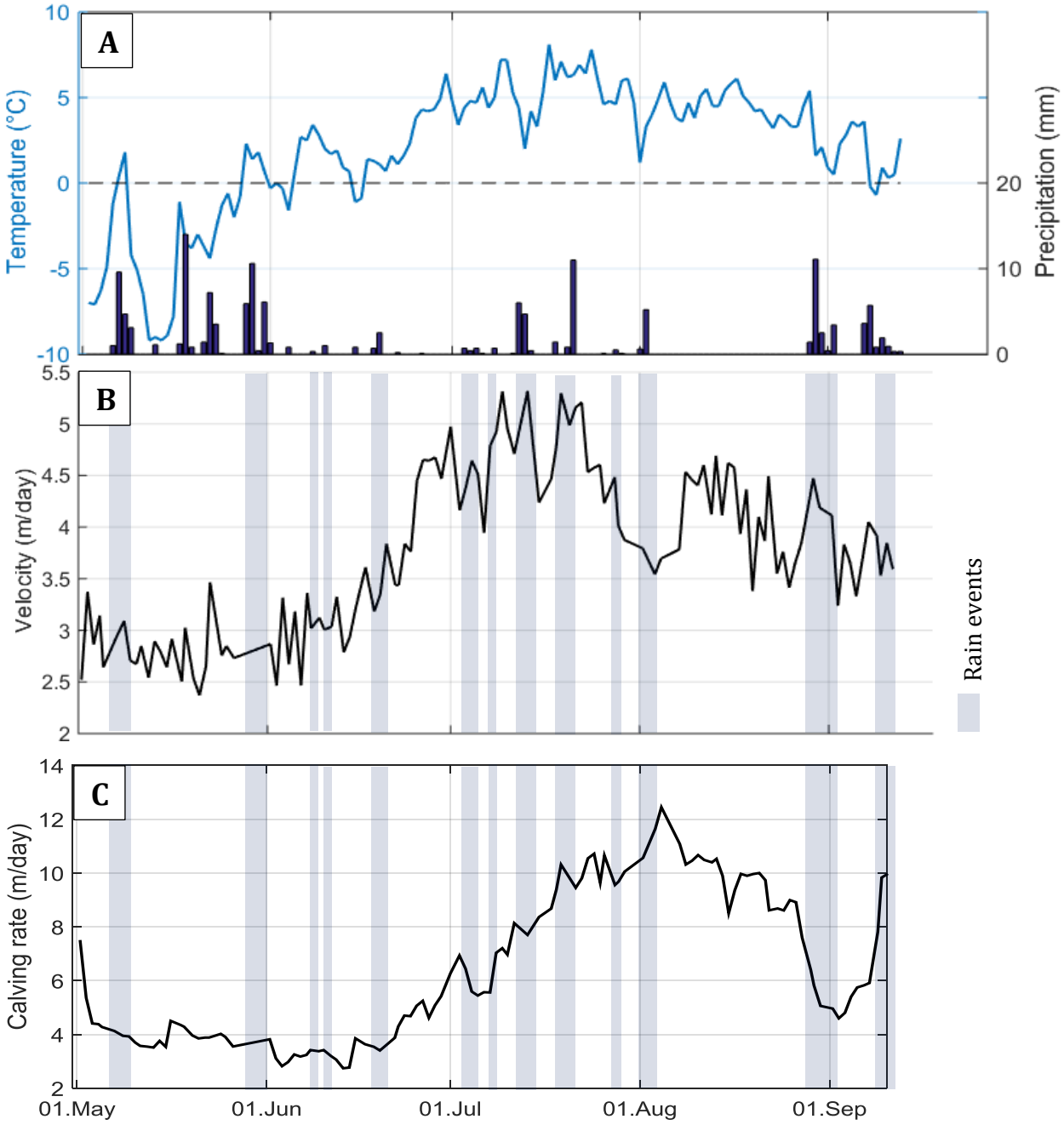

Figure 5.2 *Figure A shows meteorological data from The Norwegian Meteorological Institute station in Ny-Ålesund from May 1st to September 12th 2014.The blue line is the mean daily air temperature(°C), and the bars show the precipitation (mm). Figure B shows the calculated mean velocity from the 11 areas (**Figure 3.13**) with 24 hours interval, with blue areas marking rain events. Figure C shows the calculated and smoothed mean calving rate. The x-axes on all the graphs are the same.*

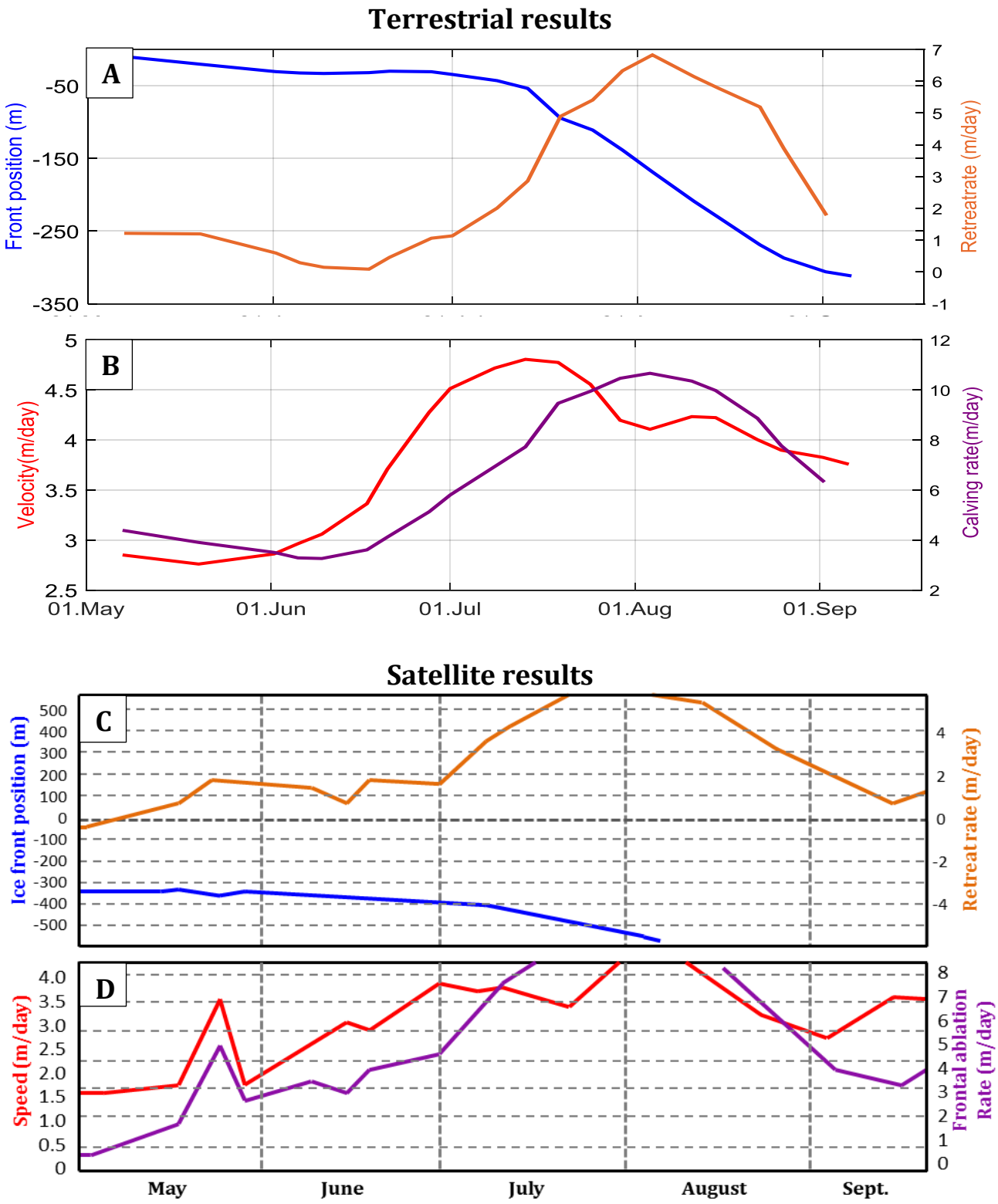

Figure 5.3 *Graph A and B show front retreat rate, front position, velocity and calving rates from May 1st to September 11th 2014, calculated with a 24 hour temporal resolution, smoothed with a moving average filter and then average over the same time intervals as the TerraSAR-X results. Graph C and D are modified from* ***Figure 2.10*** *and show the same parameters as the upper graphs calculated using TerraSAR-X imagery (modified from Luckman et al. in review).*

5.2 Front positions

A total mean retreat of 320 m was observed from May to September 2014, and calculated for the area of the front of Kronebreen investigated in this thesis. Until mid-July, the average front retreat rate was less than 2 m/day, but then increased abruptly to approximately 7 m/day in early August, where after it slowed down again through August and to September. However, the different areas of the front show different retreat patterns.

The orientation of the flow lines used for calculating front position, retreat rate and calving rate are based on the mean direction of velocity from the glacier points. This will not necessary be the true ice flow direction for every day or at every point of the glacier due to internal variations, and this may cause some uncertainties. Ideally the front retreat should be orthogonal to these flow lines to estimate the correct retreat rate. However, since the uncertainty in the manual front mapping is the same for all fronts, it will not have a major effect on the seasonal pattern, also because front retreat rate is a *relative* measurement.

The kink in the front position curve observed in mid-July (**Figure 4.12**) coincides with both a temperature low in the warmest period in **Figure 5.2 A** and a rain event at the same time. High temperatures and rain will, as discussed, trigger higher velocities (Zwally et al. 2002). Water input can trigger deeper penetration of surface crevasses; *hydrofracturing*, which may lead to calving and therefore front retreat (Benn et al 2009). This suggests that the front position may have an atmospheric forcing from rain events.

Comparison to the TerraSAR-X results shows both differences and similarities. The ice front position from the satellite data show a slow retreat of about 50 m during May and June, and the terrestrial results show a similar retreat of 50 m for the same period. Both datasets show an abrupt change in the rate of the front retreat curve in Mid-July indicating a speed-up in the front retreat. From this point to end of July the retreat is 125 m for the satellite results and 100 m for the terrestrial results. The differences can be explained by the fact that the two data sets are looking at different parts of the fronts, and with different

intervals. The satellite data may lose details that the terrestrial results show, but the satellite results cover a larger area of the front.

Lefauconnier et al. (1994) reported receding rates of Kronebreen from zero to 300 m/year, with an average of 200m/year and Kääb et al. (2005) reported a net annual retreat during summer of about 350 m. The calculated 320 m in this thesis fit very well within this range. Sund et al. (2011) also mapped front positions with terrestrial photogrammetry on Kronebreen, and found that during summer of 2008 the front retreated after a series of calving events, but then advanced towards the same position and the cycle started over again. This phenomenon is observed in Area 9 and 10 in the beginning of the period in this thesis (**Figure 4.12**).

Köhler et al. (2012) measured weekly front positions of Kronebreen using terrestrial photogrammetry from May to November in 2009 and 2010. They did not calculate the magnitude of retreat, but a relative retreat to investigate the seasonal patterns. In 2009 the front advanced in June and retreated from early July and through September. In 2010 the front advanced through June and from late-July it retreated throughout November. These seasonal patterns are very similar to what was found in this thesis, with an onset of retreat in July that continued throughout the period.

The front position graph **(Figure 4.12**) indicates that two styles of retreat occurred in the investigated part of the front. Some areas show a retreat with few and large steps, and other areas show a trend of many smaller steps. This may reflect the styles of calving in different parts of the front; either big infrequent events, or more widespread continuous calving. Area 10 and 11 show a trend of having a few large calving events. From May to mid-June Area 9 shows the same pattern with larger events, but throughout the rest of the period smaller and more continuous calving occurred (**Figure 4.12; Figure 4.11 B**). This last period coincides with the time when Area 9 is located at the embayment. The two styles of calving are discussed further in Chapter 5.3.

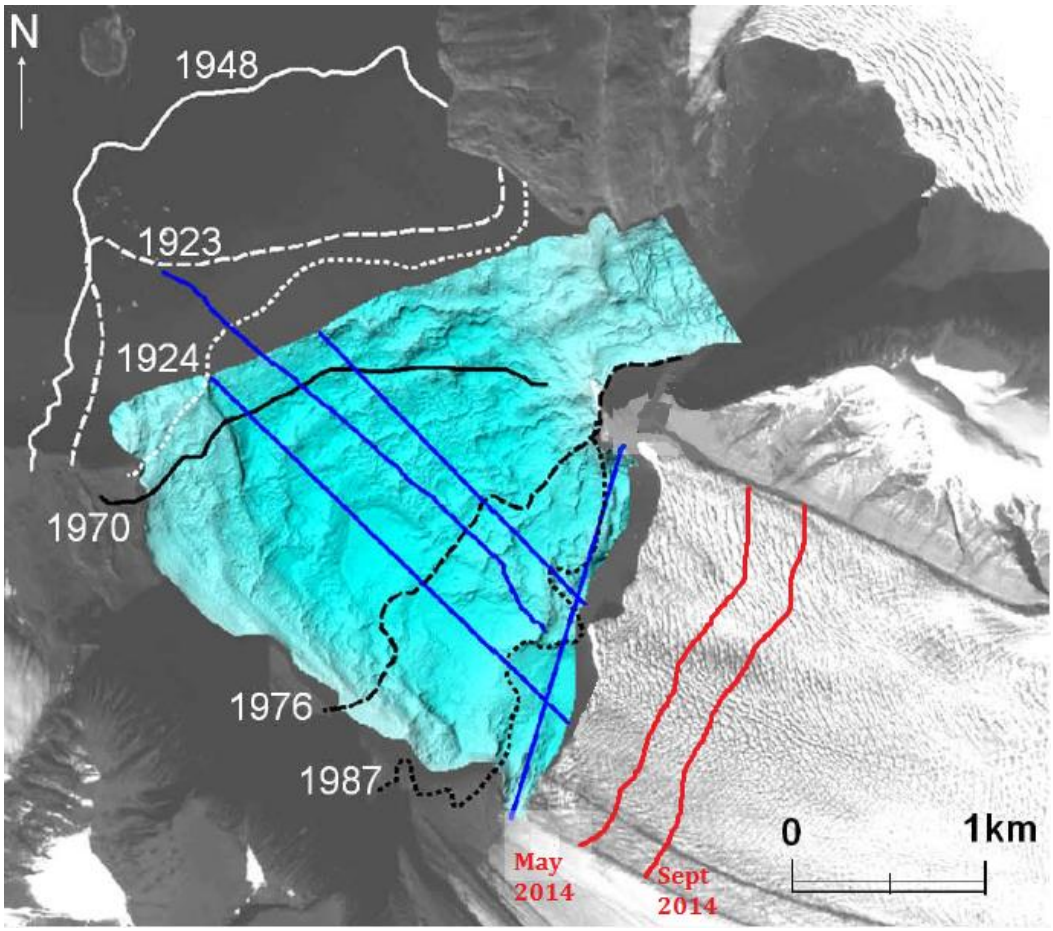

Figure 5.4 *Summer front positions of Kronebreen from 1948 to 2014, mapped onto a spot 5 image from 2007. The blue area shows the fjord bathymetry. The two red lines show the approximate front positions derived in this thesis, modified from Sund et al. (2011).*

Sund et al. (2011) plotted front positions of Kronebreen derrived from Liestøl et al. (1987) on a SPOT 5 image from 2007 (**Figure 5.4**). **Figure 5.4** shows the positions from 1948 to 2007, and the front positions from this thesis are also included. The retreat of Kronebreen after the Kongsvegen surge in 1948 was explained by fjord bathymetry with overdeepenings and pinning points (Sund et al. 2011). The front was stable around the 2007 position for a longer period, explained by a transverese ridge functioning as a pinning point. Sund et al. (2011) predicted a faster retreat after this pinning point due to an overdeepening also seen on the bed DEM in **Figure 5.1**. This may explain the fast retreat calculated here, since 2014 was not a prticularily warm summer (**Figure 2.7**) . Based ono the bed DEM (**Figure 5.1**) the bed bump mentioned at the end of chapter 5.1 may function as a new pining point in the future.

5.3 Calving rates

Calving rates calculated in this thesis had values less than 4 m/day through May and to mid-June. Then they increased through June and July and reached peak values in early August of almost 11 m/day. A decrease in calving rates after this and throughout the period was measured, and in early September the values were down to 5 m/day.

The calving rate signal is very variable due to larger individual calving events that affect the mean calving rate (**Figure 4.15 A**) and averaging the results showed the seasonal pattern more clearly (**Figure 4.15 B**). All the uncertainties and error sources from both velocity results and front positions will propagate and accumulate in the calving rate results, since this is the sum of the velocity and front retreat rate.

In all the 6 individual calving events investigated in this thesis, the ice block detached lost support on either side, and the events were sub-aerial. All events occurred on either side of the embayment (Area 6, 7, 10 and 11), and none in the actual embayment (Area 8 and 9). A melt water plume emerges in the embayment in June, and stays there for the rest of the investigation period. Other plumes emerged in several places between Area 11 to Area 6, but none were as persistent as the one in Area 9.

This formed the basis of the hypothesis where inter-plume areas, between large persistent plumes and smaller plumes emerging from time to time, along the front are dominated by infrequent large calving events, and plume areas are dominated by continuous calving. This is confirmed by looking at **Figure 4.11** where the front points are close together in Area 9 (after June when it is located in the embayment) and Area 8, and more separated in Area 6, 7, 10 and 11. In **Figure 4.12** Area 10 and 11 show a trend of a few large steps, indicating large calving events. Areas 1-5 are located further away from the camera and plume activity here is hard to investigate.

The continuous calving in the plume areas can be explained by undercutting by melt-water erosion and collapse of the sub-aerial part. Luckman et al. (in review) found a linear relationship between calving rates and fjord temperatures, which confirms the importance of undercutting at the front of Kronebreen.

A similar phenomenon to the inter-plume collapse hypothesis has been recognised on the outlet glacier Store in Greenland (Chauché et al 2014). 40% of the calving front was affected by buoyancy-driven plumes which lead to a crenulated terminus with notches where the plumes emerged and headlands in between. These headlands were exposed to mechanical failure and calving, just like the 6 individual calving events investigated in this thesis but in a larger scale. The 6 individual events do not correlate completely with peaks in the mean calving rate. Undercutting and the following isolation of inter-plume areas can be regarded a secondary calving mechanism (Benn et al. 2007a), and therefore not the main control on the calving rate.

Comparing calving rates results to meteorological data shows that the calving rate peaks coincide with a few rain events, but most of them do not. The seasonal pattern of the calving rates is not similar to the temperature trend which has an increase in June, highest values occurring in July, then a decrease and another peak in August before it decreases in September. Calving rates depend on the velocity, and are therefore to a degree controlled by the atmosphere. But since calving rates are dependent on front retreat too, the controls are more complex, which explains why the signal does not correlate as well with the temperature and precipitation signal. Chapuis and Tetzlaff (2014) investigated the nature of single-event calving by continuous visual observations of the front of Kronebreen. Each event was described with type, location, time and size. They found no significant correlations with external factors like temperature and tide and calving activity.

Comparing the results to TerraSAR-X data (Luckman et al. in review) shows that calving rates are a bit higher in the terrestrial dataset with maximum values of 11 m/day occurring in early August. The maximum values of the satellite dataset were around 9-10 m/day and occurred in early August too. The seasonal calving rate pattern and magnitudes are very similar in the two datasets, which increases the credibility in this method.

Strain rates arising from spatial variations in velocity is regarded as a first-order control on calving because they determine the depth and location of surface crevasses; large velocity gradients lead to deep crevasse penetration(Benn et al. 2007a). Chapuis concluded in her PhD (Chapuis 2011) that the local geometry and water depth around Kronebreen are controlling the strain rates, crevasse patterns and ultimately the calving activity.

From **Figure 5.2 B** and **C** it is obvious that the calving rate peak occurred after the velocity peak. Increased velocities may lead to high longitudinal strain rates which in turn leads to formation of transverse crevasses that may trigger calving as they reach the front (Benn et al. 2007a). Calculating longitudinal strain-rates from the velocity results found is unfortunately beyond the scope of this thesis.

Nuth et al. (2012) calculated long-term calving flux from Kronebreen using mass continuity, and estimated it to be −0.14± 0.03 and −0.20± 0.05 km^3 /year from the two time periods 1960-1990/95 and 1990/95-2007. 60 % of the Svalbard glaciers terminate in the ocean which results in a total length of calving fronts of about 860 km (Blaszczyk et al. 2009). The total mass loss from Svalbard has been estimated at 5-10 Gt/year, equivalent to 0.015-0.030 mm sea level rise (Nuth et al. 2015)**.** Calving is responsible for 70% of the annual transfer of mass from the cryosphere to the ocean on a global scale (van der Veen 1998a, 2002).

5.4 Estimating uncertainties

The main source of error is the uncertainty of the GCPs and that they are too few and badly distributed in the image and the outdated DEM. This will in turn propagate to the optimised camera parameters and then in the conversion for 2D to 3D and therefore the velocity, front position and calving rate results. The optimisation root mean square error output was 12.7 pixels and resulted from the mountains 10 km away, the glacier is much closer to the camera and will have a smaller projection error.

To calculate the uncertainty in metres, the uncertainty in pixels needs to be multiplied by the pixel size in the image (how many metres one pixel represents), which varies over the entire glacier surface (**Figure 3.15**). This would be a laborious process, and not very important since *relative* pixel displacements are calculated to retrieve velocities and front retreat rates. Additionally, by calculating the pixel size the projection error will be included again, and the process becomes a vicious circle.

Monte Carlo sampling of the uncertainties from the different sources is a way to estimate the magnitude of the uncertainties that propagate through the script when converting from 2D to 3D is (Messerli and Grinsted 2015). This approach makes it possible to estimate the uncertainties in the velocity in metres, when the pixel uncertainties in for example the GCPs or DEM are known. This assessment would be very useful to include in the script generated in this thesis, but due to lack of time it would be at the expense of investigating and analysing the results. Instead the latter was prioritised and emphasised. Additionally, due to few and poorly distributed GCPs and an outdated DEM the Mote Carlo sampling was give lower priority. Standard deviation of the points within each of the 11 areas could be calculated in the script for image pair. Unfortunately only the mean velocity was saved for each image pair loop and not for each point on the glacier, and it was not possible to calculate this in retrospect.

A summary of the potential error sources is shown in **Table 5.1.** Most error sources are resolved for, by filtering, averaging both spatial and temporal, super sampling and lowering the glacier surface (ablation). Including Monte Carlo sampling of the uncertainties in the script was beyond the scope of this thesis, and instead sensitivity tests, comparison to another camera and TerraSAR-x results from the same period and comparisons to previous results are performed to access the credibility of the results.

Table 5.1 *The main source of error, what it affects and the magnitude. They are all overestimated and considered a "worst case scenario". The actual impact on the results will be smaller and is dependent on place on the glacier.*

Source of error	Impact	Maximum potential magnitude
GCPs precision	2D-3D conversion	12.7 pixels
Front position mapping	Retreat rate, calving rate	5-10 pixels
Ablation	Velocity	< - 3 %
Tidal cycle offset	Velocity	-0.38 %
Template match	Velocity	~ 0
Loss of images	Velocity, front position and calving rate	~ 0
Clock drift	Velocity	~ 0
Orientation of flow lines	Retreat rate, calving rate	Unknown

5.5 Improvement of the method and future work

To improve the method the calibration part should be emphasized more. Fixed lenses and metric cameras could be used. Metric cameras are designed for use in photogrammetry, and built to maintain a stable geometry despite thermal changes. Cameras should be calibrated before being put out in the field, or ideally done in the field when cameras have acclimatized. The parameters would still vary from the in-situ calibration due to thermal changes, and one laborious solution would be to have a temperature logger by the camera in the field and a camera calibration for every temperature in the range. It would be helpful to have some known precise GCPs within the view of the camera and better distributed than the ones used in this thesis. A more recent DEM would also be useful, possibly derived stereoscopically from the two cameras. Also, a larger part of the front could be investigated, making comparison to other dataset more valuable. Another validation for the method could be to calculate velocities from the two cameras and average the results. To better estimate the uncertainties of the results, standard deviation of the 24 points within each 11 area could be calculated.

This thesis did not use stereo photogrammetric techniques for measuring velocity or front positions, but the data for doing this is available and UNIS has now got a 3D lab. Possibilities for further work could be to quantify calving frequency and magnitude of individual calving events. Calculating the calving flux through the period is an opportunity, when the area of the calving front is known (water depth). Calculating velocity gradients and strain rates form the velocity results can be done using this method. More melt-water plume activity investigation could also be done, and correlation of calving activity with water depth, and velocity with wind speed and water-pressure at the bed.

6 Summary and conclusions

The aim of this thesis was to develop the most suitable automated time-lapse techniques related to glacier observation and analyse the relationships and various controls after calculating surface velocity, front positions and calving rates.

The method is very dependent on image pairs with similar illumination and good visibility on both glacier and mountains. Many precise GCPs and a high resolution up-to-date DEM are required to be able to convert 2-D to 3-D coordinates correctly. Velocities, front positions and calving rates of Kronebreen from May to September 2014 were successfully calculated using terrestrial images with a 24 hour interval from a simple camera platform.

Results suggest that seasonal variations in velocity have a forcing from air temperature due to water input in the glacier system. Short term velocity variations may have a forcing from rain events, temperature peaks and tidal changes. Different parts of the front show different styles of retreat, and therefor calving styles. Calving rates depend on the velocity which may be atmospherically controlled, but they depend on front retreat too and internal dynamics, strain-rates caused by velocity gradients, melt-water plumes or fjord temperatures may also play a role.

The investigation of individual calving events and different retreat patterns formed the basis of the hypothesis where inter-meltwater-plume areas are dominated by infrequent large calving events due to isolation and subaerial collapse, and plume areas are dominated by continuous calving caused by subaqueous melting and undercutting.

The results were filtered, sensitivity tested, compared to another terrestrial camera and satellite derived results from the same period. Additionally they fit well to previous results which gave a high confidence that they are correct. The temporal and spatial velocity, front position and calving rate *patterns* calculated in this thesis are fully trusted. Because of few and poorly distributed ground control points and an outdated DEM the actual *magnitude* is not as certain.

The high resolution both spatially and temporally gained using this method makes it possible to capture details and gain information that satellite data are not able to. This information is required for improving the understanding of calving dynamics, to develop models to correctly predict future global sea level changes. Future work may be velocity and calving rate correlations with water-pressure at the bed, tide, water depth at the front and strain-rates.

7 Achievements

How, P. & Smith-Johnsen, S. "*Applications of time-lapse techniques at Kronebreen, Svalbard"*, talk at the Calving and Surging glaciers in Svalbard (CASS) meeting, Utrecht November 2014

Smith-Johnsen, S. How, P. Hulton, N. Benn, D. Luckman, A. *"An evaluation of terrestrial time-lapse techniques for ice velocity analysis of Kronebreen, Svalbard",* poster at the International Glaciological Society, Nordic Branch meeting (NIGS), Iceland November 2014

7.1 Outreach

- Youtube movies from the fieldwork
    - https://www.youtube.com/watch?v=ZRzQqXUh3h0
    - https://www.youtube.com/watch?v=TsskTZ0bepA
    - https://www.youtube.com/watch?v=Llod4k01DCY
- NRK-article about the CRIOS project
    - http://www.nrk.no/troms/se-isbreen-rore-pa-seg-1.12050877
- NRK-filming about me in the ice cave
    - http://www.nrk.no/troms/turiststrommen-til-svalbard-har-eksplodert-1.12258466
- NRK-filming with "mission Nansen" in the ice cave
    - NRK-super TV program 2016
- Lakselv Highschool lecture at UNIS
- Movies in Ny ålesund
    - Italian movies about research in Ny-Ålesund.
- Guiding the Norwegian Crown Prince in the ice cave
    - http://www.kongehuset.no/nyhet.html?tid=126988&sek=26939
- Interview in UiB student newspaper "Studvest"
    - http://www.studvest.no/livet-er-svalbard/
- Interview in Svalbardposten newspaper
    - http://svalbardposten.no/index.php?page=vis_nyhet&NyhetID=5928

8 References

Ahn, Y. and Box, J. E. (2010), 'Glacier velocities from time lapse photos: technique development and first results from the Extreme Ice Survey (EIS) in Greenland', *Journal of Glaciology,* 56 (198), 723-34.

Ahn, Y. and Howart, I. (2011), 'Efficient, Automated Glacier Surface Velocity Measurement from Repeat Images Using Multi-Image/Multi-Chip (MIMC) and Null Exclusion Feature Tracking', *Transactions on Geoscience and Remote Sensing journal*.

Bartholomaus, T. C., Larsen, C. F., and O'Neel, S. (2013), 'Does calving matter? Evidence for significant submarine melt', *Earth and Planetary Science Letters,* 380 (0), 21-30.

Benn, D. I., and Evans, D.J.A (2010), *Glaciers and Glaciation, Second edition* (London: Hodder Education).

Benn, D. I.,Gulley, J. Luckman, A. Adamek, A. & Glowacki, P. (2009). Englacial drainage systems formed by hydrologically driven crevasse propagation. *Journal of Glaciology* 55(191), 513-523.

Benn, D. I., Warren, C. R., and Mottram, R. H. (2007a), 'Calving processes and the dynamics of calving glaciers', *Earth-Science Reviews,* 82 (3–4), 143-79.

Benn, D. I., Hulton, N. R. J., and Mottram, R. H. (2007b), "Calving laws', 'sliding laws' and the stability of tidewater glaciers', *Annals of Glaciology,* 46 (1), 123-30.

Blaszczyk, M., Jania, J. A., and Hagen, J. O. (2009), 'Tidewater glaciers of Svalbard: recent changes and estimates of calving fluxes', *Pol. Polar Res,* 30 (2), 85-142.

Brown, C. S., Meier, M. F., Post, A. (1982), 'Calving speed of Alaska tidewater glaciers, with application to Columbia Glacier', *USGS Professional Paper,* 1258-C.

Chapuis, A. and Tetzlaff, T. (2014), 'The variability of tidewater-glacier calving: origin of event-size and interval distributions', *Journal of Glaciology,* 60 (222).

Chapuis, A. (2011), 'What controls calving? From observations to predictions', PhD thesis, Department of Mathematical Sciences and Technology, Norwegian University of Life Sciences.

Chauché, N., Hubbard, A., Gascard, J. C., Box, J. E., Bates, R., Koppes, M., Patton, H. (2014). Ice–ocean interaction and calving front morphology at two west Greenland tidewater outlet glaciers. *The Cryosphere*, *8*(4), 1457-1468.

Cuffey, K.M. and Paterson, W.S.B (2010), *The physics of Glaciers, fourth edition* (Academic Press) 704.

Debella-Gilo, M. and Kääb, A. (2011), 'Sub-pixel precision image matching for measuring surface displacements on mass movements using normalized cross-correlation', *Remote Sensing of Environment,* (115), 130–42.

Dowdeswell, J. A., Benham, T. J., Strozzi, T., Hagen, J. O. (2008), 'Iceberg calving flux and mass balance of the Austfonna ice cap on Nordaustlandet, Svalbard', *Journal of Geophysical Research: Earth Surface,* 113 (F3), F03022.

Dowdeswell, J.A. (1989), ' On the nature of Svalbard icebergs', *Journal of Glaciology,* 35 (120), 224–34.

Eiken, T. and Sund, M.(2012), 'Photogrammetric methods applied to Svalbard glaciers: accuracies and challenges', *Polar Research,* 31.

Førland, J. and Hanssen-Bauer, I. (2003), 'past and future climate variations in the Norwegian arctic: overview and novel analyses', *Polar Research,* 22, 113-24.

Glasser, N. F. and Hambrey, M. J. (2001), 'Tidewater glacier beds: insights from iceberg debris in Kongsfjorden, Svalbard', *Journal of Glaciology,* 47 (157), 295-302.

Hagen, J. O. and Liestøl, O. (1990), 'Long-Term glacier mass balance investigations in Svalbard 1950.1988', *Ann. Glaciol.*, 14, 102-06.

Hagen, J. O., Liestøl, O. Roland, E. Jørgensen, T. (1993), *Glacier atlas of Svalbard and Jan Mayen* (Oslo: Norsk Polarinstitutt meddelelser nr 129).

Hagen, J. O., Kohler, J. , Melvold, K., Winther, J. G.,. (2003a), 'Glaciers in Svalbard: mass balance, runoff and freshwater flux', *Polar Research,* 22 (2).

Hagen, J. O., Melvold, K., Pinglot, F., Dowdeswell, J. A.. (2003b), 'On the Net Mass Balance of the Glaciers and Ice Caps in Svalbard, Norwegian Arctic', *Arctic, Antarctic, and Alpine Research,* 35 (2), 264-70.

Harris, C. and Stephens, M. (1988), 'A Combined Corner and Edge Detector', *Proceedings of the 4th Alvey Vision Conference*, 147-51.

Heid, T. and Kääb, A. (2012), 'Evaluation of existing image matching methods for deriving glacier surface displacements globally from optical satellite imagery', *Remote Sensing of Environment* (118), 339-55.

Hjelle, A. (1993), *Geology of Svalbard* (Oslo: Norsk Polarinstitutt).

Hooke, R. LeB. (2005), *Principles of Glacier Mechanics* (Cambridge University Press).

Humlum, O., Instanes, A., and Sollid, J. L. (2003), 'Permafrost in Svalbard: a review of research history, climatic backrground and engeneering challenges', *Polar Research,* 22 (2), 191-215.

Ingólfsson, Ó. and Landvik, J. (2013), 'The SvalbardeBarents Sea ice-sheet e Historical, current and future perspectives', *Quaternary Science Reviews,* 64, 33-60.

IPCC (2013), 'Climate Change 2013: The Physical Science Basis. Working group 1 contribution to the Fifth Assessment Report of the Intergovernmental Panel on Climate Change.'.

James, M. 'http://www.lancaster.ac.uk/staff/jamesm/software/pointcatcher.htm'.

James, T.D., Murray, T., Selmes, N., Scharrer, K., Oleary, M. (2014), 'Buoyant flexure and basal crevassing in dynamic mass loss at Helheim Glacier', *Nature Geosci*, 7 (8), 593-96.

Krimmel, R.M. and Rasmussen, L.A. (1986), 'Using sequential photography to estimate ice velocity at the terminus of columbia glacier, Alaska', *Ann. Glaciol.*, 08, 117-23.

Krimmel, R.M. and Vaughn, B. H. (1987), 'Columbia Glacier, Alaska: Changes in velocity 1977–1986', *Journal of Geophysical Research: Solid Earth,* 92 (B9), 8961-68.

Kääb, A., Lefauconnier, B., and Melvold, K. (2005), 'Flow field of Kronebreen, Svalbard, using repeated Landsat 7 and ASTER data', *Annals of Glaciology,* 42 (1), 7-13.

Köhler, A., Chapuis, A., Nuth, C. Kohler, J. & Weidle, C. (2012). 'Autonomous detection of calving-related seismicity at Kronebreen, Svalbard.', *The Cryosphere, 6*(2), 393-406

Köhler, A., Chapuis, A., Nuth, C. Kohler, J. (2011), 'Seasonal variations of glacier dynamics at Kronebreen, Svalbard revealed by calving related seismicity', *The Cryosphere Discussions*.

Lefauconnier, B., Hagen, J. O., and Rudant, J . P. (1994), 'Flow speed and calving rate of Kongsbreen glacier, Svalbard, using SPOT images', *Polar Research,* 59-65.

Liestøl, O. (1988), 'The glaciers in the Kongsfjorden area, Spitsbergen', *Norsk Geografisk Tidsskrift,* 42, 231-38.

Luckman, A., Luckman, A., Benn, D. I., Cottier, F., Bevan, S., Nilsen, F., Innal, M. (in review), 'Calving rates at tidewater glaciers depend linearly on ocean temperature', *Nature*

Marsh, O. J., Rack, W., Floricioiu, D., Golledge, N. R., & Lawson, W. (2013), 'Tidally induced velocity variations of the Beardmore Glacier, Antarctica, and their representation in satellite measurements of ice velocity' *Cryosphere*, *7*(5), 1375-1384.

Meier, M. F. and Post, A. (1987), 'Fast tidewater glaciers', *Journal of Geophysical Research: Solid Earth*, 92 (B9), 9051-58.

Meier, M. F., Lundstrom, S., Stone, D., Kamb, B., Engelhardt, H., Humphrey, N., Dunlap, W. W., Fahnestock, M., Krimmel, R. M., Walters, R. (1994), 'Mechanical and hydrologic basis for the rapid motion of a large tidewater glacier: 1. Observations', *Journal of Geophysical Research: Solid Earth*, 99 (B8), 15219-29.

Melvold, K. and Hagen, J. O. (1998), 'Evolution of a surge-type glacier in its quiescent phase: Kongsvegen, Spitsbergen, 1964–95.', *Journal of Glaciology*, 44 (147), 394-404.

Messerli, A. and Grinsted, A. (2015), 'Image GeoRectification And Feature Tracking toolbox: ImGRAFT', *Geosci. Instrum. Method. Data Syst.*, 4, 23-34.

Moholdt, G. (2010), 'Elevation change and mass balance of Svalbard glaciers from geodetic data.', *PhD*, Department of Geosciences, Faculty of Mathematics and Natural Sciences, University of Oslo

Nick, F. M., van der Veen, C. J., Vieli, A., Benn, D. I. (2010), 'A physically based calving model applied to marine outlet glaciers and implications for the glacier dynamics', *Journal of Glaciology*, 56 (199), 781-94.

Nick, F. M., Vieli, A. Andersen, M. L., Joughin, I., Payne, A., Edwards, T. L., Pattyn, F., van de Wal, R. S. W. (2013), 'Future sea-level rise from Greenland's main outlet glaciers in a warming climate', *Nature*, 497 (7448), 235-38.

NMI (2015), www.eklima.met.no, Norwegian Meteorological institute.

Nuth, C., Moholdt, G., Kohler, J., Hagen, J. O., Kääb, A. (2010), 'Svalbard glacier elevation changes and contribution to sea level rise', *Journal of Geophysical Research: Earth Surface*, 115 (F1)

Nuth, C., Schuler, T. V., Kohler, J., Altena, B., Hagen, J. O. (2012), 'Estimating the long-term calving flux of Kronebreen, Svalbard, from geodetic elevation changes and mass-balance modelling', *Journal of Glaciology*, 58 (207), 119-33.

Nuth, C., Hagen, J. O., Kohler, J., (2015), 'Chapter 4, Glaciers' *In:* Dallman, W. K.(Ed) 'Geoscinence Atlas of Svalbard', Norwegian Polar Institute, Report 148, Tromsø.

Nye, J. F. (1957), 'The distribution of stress and velocity in glaciers and ice-sheets', *Proceedings of the Royal Society*, 239 (1216), 113-33.

O'Neel, S., Echelmeyer, K. A., and Motyka, R. J. (2003), 'Short-term variations in calving of a tidewater glacier: LeConte Glacier, Alaska, U. S. A', *Journal of Glaciology*, 49 (167), 587-98.

O'Leary, M. and Christoffersen, P. (2013), 'Calving on tidewater glaciers amplified by submarine frontal melting', *The Cryosphere*, 7, 119-28.

Otero, J., Navarro, F. J., Martin, C., Cuadrado, M. L., Corcuera, M. I. (2010), 'A three-dimensional calving model: numerical experiments on Johnsons Glacier, Livingston Island, Antarctica', *Journal of Glaciology*, 56 (196), 200-14.

Pelto, M. S. and Warren. C.R. (1991), 'Relationships between tidewater glacier calving velocity and water depth at the calving front', *Annals of Glaciology*, 15, 115-18.

Rignot, E., Casassa, G., Gogineni, P., Krabill, W., Rivera, A., Thomas, R. (2004), 'Accelerated ice discharge from the Antarctic Peninsula following the collapse of Larsen B ice shelf', *Geophysical Research Letters*, 31 (18), L18401.

Rolstad, C. and Norland, R. (2009), 'Ground-based interferometric radar for velocity and calving-rate measurements of the tidewater glacier at Kronebreen, Svalbard', *Annals of Glaciology*, 50 (50), 47-54.

Sand, K., Sand, K., Winther, J.-G., Maréchal, D., Bruland, O., Melvold, K. (2003), 'Regional Variations of Snow Accumulation on Spitsbergen, Svalbard, 1997-99', *Nordic Hydrology*, 34 (1-2), 17-32.

Sund, M. (2011), 'On the dynamics of surge-type and tidewater glaciers in Svalbard', *PhD*.

Sund, M., Eiken, T., and Rolstad, C. (2011), 'Velocity structure, front position changes and calving of the tidewater glacier Kronebreen, Svalbard', *The Cryosphere Discuss.*, 5, 41-73.

Sundal, A. V., Shepherd, A., Van Den Broeke, M., Van Angelen, J., Gourmelen, N., and Park, J. (2013), 'Controls on short-term variations in Greenland glacier dynamics', J. Glaciol., 59 (217), 883–892.

Svanem, M. (2010), 'Terrestrial Photogrammetry for velocity measurement of Kronebreen Calving Front', *Norwegian University of Life Sciences*.

Svendsen, H., Beszczynska-Møller, A., Hagen, J. O., Lefauconnier, B., Tverberg, V., Gerland, S., Ørbøk, J., Bischos, k., Papucci, C., Zajaczkowski, M., Azzolini, R., Bruland, O., Wiencke, C. (2002), 'The physical environment of Kongsfjorden-Krossfjorden, an Arctic fjord system in Svalbard.', *Polar Research*, 21 (1).

Trusel, L. D., Powell, R. D., Cumpston, R. M., Brigham-Grette, J. (2010), 'Modern glacimarine processes and potential future behaviour of Kronebreen and Kongsvegen polythermal tidewater glaciers, Kongsfjorden, Svalbard', *Geological Society, London, Special Publications 2010*, 344, 89-102.

van der Veen, C. J. (1996), 'Tidewater calving', *Journal of Glaciology*, 42 (141), 375-85.

van der Veen, C. J. (1998a), 'Fracture mechanics approach to penetration of surface crevasses on glaciers', *Cold Regions Science and Technology*, 27 (1), 31-47.

van der Veen, C. J. (1998b), 'Fracture mechanics approach to penetration of bottom crevasses on glaciers', *Cold Regions Science and Technology*, 27 (3), 213-23.

van der Veen, C. J. (2002), 'Calving glaciers', *Progress in Physical Geography*, 26 (1), 96-122.

van der Veen, C. J. (2013), *Fundamentals of Glacier Dynamics, Second Edition* (CRC Press).

Vieli, A., Funk, M., and Blatter, H. (2001), 'Flow dynamics of tidewater glaciers: a numerical modelling approach', *Journal of Glaciology*, 47 (159), 595-606.

Vieli, A., Jania, J. A., and Kolondra, L. (2002), 'The retreat of a tidewater glacier: observations and model calculations on Hansbreen, Spitsbergen', *Journal of Glaciology*, 48 (163), 592-600.

Vieli, A., Jania, J. A., Blatter, H., Funk, M. (2004), 'Short-term velocity variations on Hansbreen, a tidewater glacier in Spitsbergen', *Journal of Glaciology*, 50 (170), 389-98.

Welty, E. Z., Bartholomaus, T. C., O'Neel, S., Pfeffer, W. T. (2013), 'Cameras as clocks', *Journal of Glaciology*, 59 (214), 275-86.

Zwally, H. J., Abdalati, W., Herring, T., Larson, K., Saba, J., & Steffen, K. (2002), 'Surface melt-induced acceleration of Greenland ice-sheet flow', *Science, 297*(5579), 218-222

Appendix 1 Driving and resisting forces

Most glaciers move so slowly that acceleration may be neglected, and it follows from Newton's law that the sum of forces acting on the glacier equals zero, in other words the system is in equilibrium (van der Veen 2013). The flow of a glacier is controlled by both driving stresses and resistive stresses, which are close to being in balance. *Driving stress* is induced by gravity and defined as:

$$\tau_d = \rho_i \, g \, H \tan \alpha \qquad \textbf{Eq Ap-1.1}$$

Where ρ_i is density of glacier ice, g is the gravity constant, H is the vertical thickness of the glacier and α is the surface slope of the ice. The *resistive stresses* are *basal drag*, *lateral drag* and *longitudinal stress gradients*. Basal drag is hard to measure directly, but in a few cases it is equal but opposite of the driving stress. Lateral drag is resistance from the margins, and is especially important for valley glaciers and ice streams. The longitudinal stress gradient can be both positive and negative, and is due to compression and tension variations along-flow of the glacier. **Eq Ap-1.2** shows driving stresses balanced by resisting stresses:

$$\rho_i \, g \, H \tan \alpha = \tau_b + \frac{\partial (H \, \sigma xy)}{\partial y} + \frac{\partial (H \, \sigma' xx)}{\partial x} \qquad \textbf{Eq Ap-1.2}$$

The left side is the driving stress, **Eq Ap-1.2**, the first term on the right side is basal drag, the second is lateral drag and the third is resistance from longitudinal stress gradients. σ_{xy} is lateral shear stress and σ'_{xx} is longitudinal stress (Benn and Evans 2010; Cuffey and Paterson 2010; Hooke 2005).

Appendix 2 Calving laws

Water-depth criterion

Brown (1982) found that water depth at the terminus is linearly proportional to the annual average calving rate in m/year of 12 Alaskan tidewater glaciers. They suggested the simple water-depth relation:

$$U_c = c\ D \qquad \textbf{Eq Ap-2.1}$$

Where U_c is the annual average calving rate in metres per year, and D is the water depth at the termini in metres. The best estimate of coefficient c is 27.1 +/-2 a^{-1}. This calving relation does not apply to glaciers regarding seasonal calving rates, and it does not apply for a floating termini.

Meier and Post (1987) suggested a cyclic behaviour for tidewater glaciers, where the terminus go through long lasting steady phases of slow advance and much shorter lasting phases of rapid retreats through a depression in the basal topography. The advance phase lasts perhaps 1000 years with advance rates ranging from 20 -40 m/year, and the retreat phase more variable lasting from decades to centuries, with rates ranging from a few hundred metres to 2km/year. The authors proposed that the linear calving relation only apply to glaciers with a steady state terminus.

Pelto (1991) considered the Alaskan data set in addition to more data from Greenland and Svalbard glaciers, and found a rather different but linear relationship between water-depth at the terminus and mean annual calving rate:

$$U_c = 0.07 + 0.008\ D \qquad \textbf{Eq Ap-2.2}$$

They concluded that “Rates of iceberg calving for both temperate and polar grounded tidewater glaciers are dominantly controlled by the water depth at the terminus over periods of a year or more, for reasons not fully understood at present”.

In addition they proposed that the relationship cannot be a causal one, and may be "…a spurious result, due to limited data?". The conclusion of water-depth calving criterion is that it is valid for some stabile glaciers with slow advances and retreats.

Height above buoyancy calving criterion

In 1996 Van der Veen, inspired by the suggestion of Meier and Post (1987) that the terminus appears to retreat to the point where effective basal pressure approaches zero, suggested a new and different mechanism for calving, focused on the factors that control the position of calving terminus, not the rate of calving. This was based on observations from the extensive Columbia glacier data set; during the retreat the thickness at the terminus remained at about 50m in excess of the flotation thickness, thus suggesting that calving occurs whenever the terminal thickness in excess of flotation becomes less than some critical value (van der Veen 2013). If the glacier terminus thins due to ablation or longitudinal extension, the front would calve back to where the critical value was again satisfied (Benn and Evans 2010) or in simpler terms; the almost floating part of the snout breaks off, because the ice is too weak to support a floating tongue (van der Veen 1996). This critical value is given by:

$$H_c = \frac{\rho w}{\rho i} D + H_0 \qquad \textbf{Eq Ap-2.3}$$

Where ρ_w and ρ_i is the densities of sea water and ice respectively, D is water depth at the terminus and H_0 is the thickness at the terminus in excess of flotation. For Columbia glacier $H_0 \approx 50$ m. van der Veen (1996) thus concluded "This means that the rate of retreat is controlled by the thinning rate of the ice and by local geometry". He stresses the fact that calving rate is a secondary parameter determined by ice velocity, and will increase proportionally with increasing glacier speed with a possible small time delay.

Vieli et al. (2001) proposed a modified flotation criterion were the value H_0 is replaced by a small fraction q of the flotation thickness at the terminus:

$$H_c = \frac{\rho w}{\rho i} (1 + q) D \qquad \textbf{Eq Ap-2.4}$$

As previously mentioned $H_0 \approx 50$ m for Columbia Glacier, which equals a value of q = 0.15. Using this criterion they ran their models and confirmed Meier and Post (1987) concept of rapid retreat and slow advance of a tidewater glacier through a basal depression. During slow advance or retreat, the linear relationship between water depth at the terminus and calving rate is reproduced by the model. Unstable rapid retreats can be explained by prescribing the modified flotation criterion into the model (Vieli et al. 2001). van der Veen (1996) explained the initiation of Columbia Glacier's rapid retreat by thinning of the glacier.

The model of Vieli indicate that whether a retreat or advance is fast or slow, depends not only on water depth but also on whether the bed slopes up or down in ice flow direction. Climate warming and thus thinning of the glacier is just a trigger to rapid retreat, basal topography (whether it slopes up or down in ice flow direction) is a more important parameter. The modification of Vieli still does not allow an ice shelf to form.

Waterline crevasse-depth model

Benn et al. (2007b) wanted to overcome the limitations in former models, and developed a calving criterion based on the downward propagation of transverse surface crevasses formed due to longitudinal strain rates. van der Veen (1998b, 1998a) applied linear elastic fracture mechanics (LEFM) to estimate penetration depth of crevasses on glaciers, but Benn et al. (2007b) simplified it and assumed that crevasses will penetrate to the depth where the tensile stress equals the lithostatic stress and therefore the net longitudinal stress is zero.

Crevasse depth is then given by the formula from Nye (1957):

$$d = \frac{2}{\rho i\, g} \left(\frac{\dot{\varepsilon}*}{A}\right)^{1/n} \qquad \textbf{Eq Ap-2.5}$$

where g is gravitational acceleration, A and n are flow-law parameters and ε̇* is the longitudinal strain rate equal to δU/δx. Crevasses with water will penetrate deeper than dry crevasses predicted by Nyes formula, and the effect of this can be incorporated in the equation:

$$d = \frac{2}{\rho i\, g} \left[\left(\frac{\dot{\varepsilon}*}{A}\right)^{1/n} + \rho_w g d_w\right] \qquad \textbf{Eq Ap-2.6}$$

where d_w is the water depth in the crevasses. Water can come from surface melt, supraglacial ponds or from a free connection from the crevasse to the proglacial water body (Benn et al. 2007b). The authors assumed that where the glacier reaches sea level (or the lake) a connection exists and the crevasses penetrate the full thickness of the ice. The glacier margins is defined by where the glacier freeboards, h, equals the crevasse depth, d. This criterion allows a floating ice shelf to form, if the longitudinal velocity gradient is sufficiently small. This criterion was called waterline crevasse depth model, and the model was tested out in a 3d model by Otero et al. (2010).

Based on observed calving of large tabular icebergs from Greenlandic outlet glaciers, Nick et al. (2010) modified the waterline crevasse-depth model, and defined the calving terminus as the point where both water-filled surface crevasses and basal crevasses penetrate the full glacier thickness. They stressed the fact that the waterline crevasse-depth model still may be applicable to small relatively slow moving glaciers, like many in Svalbard, and that the modified model fit better for large fast-flowing glaciers like those in Greenland. The propagation of basal crevasses is possible when the glacier is floating and stretching rates are big, if the terminus is grounded the propagation of surface crevasses play a bigger role.

Appendix 3 Main MATLAB script

```
%%     Calculating glacier velocities and front retreat rates by feature tracking between
terrestrial image pairs using the ImGRAFT toolbox (http://imgraft.glaciology.net/).

%input:
%#Camera parameters
%#DEM
%#GCPs
%#image pairs

%Output:
  #Mean glacier surface velocities within 11 areas, «Vn»
  #Front retreat rates, «Vn_front»

close all
clear

%% Load everything needed for camera model
datafolder='BØ';
load 'points_static_1892.mat';%points on the mountain
GCP_IMG=imread('IMG_1892.JPG'); %image to do calibration and cam_fullmodel on
dem=load(fullfile(datafolder,'dem'));
gcpA=load(fullfile(datafolder,'gcp1892_nyest.txt'));
f=[4815.95482 4701.271546];%found in computer vision toolbox,
imgsz=[3456 5184];
cameralocation=[447906 8759453 387];
c=[2589.1982 1464.6164];
camA=camera(cameralocation,[3456 5184],[270 -15 0]*pi/180,f,c);
camA.p=([0.01160 -0.001571]);
[camA,rmse,aic]=camA.optimizecam(gcpA(:,1:3),gcpA(:,4:5),'00000111110000000011');

%% START  image pair loop
% preallocating variables
M=struct('cdata',[],'colormap',[]); %saves images for movie
N=struct('cdata',[],'colormap',[]); %saves images for movie
rowmax=300;%number of points in grid generated
uvA=zeros(rowmax,2);          uvB=zeros(rowmax,2);
xyzA=zeros(rowmax,3);         xyzB=zeros(rowmax,3);
V=zeros(rowmax,3);            Vn=zeros(rowmax,1);
frontA=zeros(11,2); %frontpoints from flowlineintersection with front
frontB=zeros(11,2);  %frontpoints from flowlineintersection with front
count=1;%this is used to get a contiues/full M.cdata
signal2noise=zeros(rowmax,1);

for i = [20:22]; %which frames to track
    load('front_july.mat');%this is the fronts for current month, used later
    datafolder = 'BØ/frames_july';
    idA=000 + i; %starting point
    idB=001 + i; % image ids (/file numbers). decides the time gap in pair
if idA < 10
fA=fullfile(datafolder,sprintf('00%1.0f.jpg',idA));
elseif idA >= 10
fA = fullfile(datafolder,sprintf('0%2.0f.jpg',idA));
elseif idA >= 100
fA = fullfile(datafolder,sprintf('%3.0f.jpg',idA));
end

if idB < 8
fB=fullfile(datafolder,sprintf('00%1.0f.jpg',idB));
elseif idB >= 10
fB = fullfile(datafolder,sprintf('0%2.0f.jpg',idB));
elseif idB >= 100
fB = fullfile(datafolder,sprintf('%3.0f.jpg',idB));
end

A=imread(fA); B=imread(fB);
metaA=imfinfo(fA);tA(i)=datenum(metaA.DateTime,'yyyy:mm:dd HH:MM:SS');
metaB=imfinfo(fB);tB(i)=datenum(metaB.DateTime,'yyyy:mm:dd HH:MM:SS');
```

```
%% Load frontA corresponding to image A and front B
j=i+1; %frame interval

front_uv=[point1(i,:);point2(i,:);point3(i,:);point4(i,:);point5(i,:);point6(i,:);point7(i,:);poi
nt8(i,:);point9(i,:);point10(i,:);point11(i,:);point12(i,:);point13(i,:);point14(i,:);point15(i,:
);point16(i,:);point17(i,:);point18(i,:);point19(i,:);point20(i,:)];

frontB_uv=[point1(j,:);point2(j,:);point3(j,:);point4(j,:);point5(j,:);point6(j,:);point7(j,:);po
int8(j,:);point9(j,:);point10(j,:);point11(j,:);point12(j,:);point13(j,:);point14(j,:);point15(j,
:);point16(j,:);point17(j,:);point18(j,:);point19(j,:);point20(j,:)];

front_uv=front_uv(~any(isnan(front_uv),2),:);
front_xyz=camA.invproject(front_uv,dem.X,dem.Y,dem.front); %convert frontA to xyz

%% Determine view direction of camera B.
% # find movement of rock features between images A and B

points1=[4200, 910];
xyo=templatematch(A,B,points1,200,260,0.5,[0 0],false,'PC');
[dxy,C]=templatematch(A,B,points,30,40,2,xyo,[idA idB]);

xyz=camA.invproject(points);
camB=camA.optimizecam(xyz,points+dxy,'00000111000000000000');
DeltaViewDirection=(camB.viewdir-camA.viewdir)*180/pi;

frontB_xyz=camB.invproject(frontB_uv,dem.X,dem.Y,dem.front);
strange=find(frontB_xyz(:,3)~=0);%locate rows with wrong z-values
frontB_xyz(strange)=nan; %give them value nan
frontB_xyz=frontB_xyz(~any(isnan(frontB_xyz),2),:); %deletes all NaNs
%% Generate points to be tracked(xyz-grid/geographical grid based on front position)
rad=deg2rad(45);%degres of flowline, 600 is how far grid is upglacier
[X,Y] = meshgrid(min(front_xyz(:,1)):75:max(front_xyz(:,1))+600*cos(rad),
8.7568*10^6:75:max(front_xyz(:,2)));
Z=interp2(dem.X,dem.Y,dem.Z,X,Y);
xyzA_temp=[X(:),Y(:),Z(:)];

% define polygon over ocean, and take away points in ocean
OX=front_xyz(:,1); OY=front_xyz(:,2);
xIndex = find(OY == max(OY)); maxXValue = OX(xIndex);
oceanX=vertcat(front_xyz(:,1),maxXValue,min(front_xyz(:,1)),min(front_xyz(:,1)));
oceanY=vertcat(front_xyz(:,2),max(front_xyz(:,2))+100,max(front_xyz(:,2))+100,min(front_xyz(:,2))
);
[in,on] = inpolygon(xyzA_temp(:,1),xyzA_temp(:,2),oceanX,oceanY);
xyzA_temp(in,:)=[]; %deletes point IN ocean
[uvAtemp,~,inframe]=camA.project(xyzA_temp); %temp=midlertidig
xyzA_temp=xyzA_temp(inframe,:); %cull points outside the camera field of view.
uvA(1:length(find(inframe>0)),:,i)=uvAtemp(inframe,:);
uvA(:,:,i)=round(uvA(:,:,i));

%% Track points between images.
% accounting for camera shake
camshake=camB.project(camA.invproject(uvA(:,:,i)))-uvA(:,:,i);
showprogress=[idA idB];
wsearch=45;            wtemplate=15;
super=3; %supersample the input images
[dxy,C]=templatematch(A,B,uvA(:,:,i),wtemplate,wsearch,super,camshake,showprogress,'myNCC');
uvB(:,:,i)=uvA(:,:,i)+dxy;
signal2noise(:,1,i)=C(:,1)./C(:,2);

%% georef uv-points and calculate velocity
dem.glacier=dem.glacier-7;
xyzA(:,:,i)=camA.invproject(uvA(:,:,i),dem.X,dem.Y,dem.glacier);
xyzB(:,:,i)=camB.invproject(uvB(:,:,i),dem.X,dem.Y,dem.glacier);
V(:,:,i)=(xyzB(:,:,i)-xyzA(:,:,i))./(tB(i)-tA(i)); % 3d velocity.
Vn(:,:,i)=sqrt(sum(V(:,1:2,i).^2,2)); %this is the velocity
%% Filter out bad points from Vn and V
filter2=signal2noise(:,:,i)<2&C(:,1)<.7; %certain signal2noise ratio
Vn(filter2,i)= NaN;   V(filter2,i)= NaN;
count=count+1; camA=camB; disp('finish pair')
end
```

Appendix 4 IGS Nordic poster

Appendix 5 IGS Nordic Abstract

An evaluation of terrestrial time-lapse techniques for ice velocity analysis of Kronebreen, Svalbard

Silje Smith-Johnsen[1,2], Penelope How [1,3], Nick Hulton [1,3], Doug Benn [1,4], Adrian Luckman [1,5]

1. The University Centre in Svalbard (UNIS) – Norway
2. The University of Bergen - Norway
3. The University of Edinburgh – UK
4. The University of St Andrews -UK
5. Swansea University - UK

We compare the capability of a range of different methods to reliably track glacial features, and to measure ice velocity from terrestrial time-lapse photography. This is explored using oblique mono and stereo imagery from Kronebreen, a fast flowing tidewater glacier in Svalbard, taken from May to September 2014. The project forms part of the CRIOS (Calving Rates and Impact on Sea Level) program whose overall aim is to develop better calving-process models.

Two automated terrestrial digital SLR time-lapse cameras are used to take overlapping oblique photographs of the ice margin every 30 minutes. We consider both stereo- and mono-photogrammetric techniques coupled with the use of a DEM and ground control points. The ideal software for this project would be automated, user-friendly with minimal inputs and capable of tackling illumination changes to reliably measure ice velocity. By comparing the feasibility of several methods, we aim to maximise measurement precision and to augment the production of quantifiable measurements of glacier movement through time.

Appendix 6 Dates for the imagery used

Terrestrial time-lapse imagery:

01-May-2014 11:58:45
02-May-2014 11:58:49
03-May-2014 11:58:53
04-May-2014 11:58:57
05-May-2014 01:58:59
07-May-2014 02:29:07
08-May-2014 11:59:13
09-May-2014 11:59:17
10-May-2014 11:59:21
11-May-2014 07:29:24
12-May-2014 11:59:29
13-May-2014 11:59:33
14-May-2014 11:59:37
15-May-2014 11:59:41
16-May-2014 07:29:45
17-May-2014 22:59:51
18-May-2014 11:59:54
19-May-2014 20:29:59
20-May-2014 20:30:03
21-May-2014 22:00:07
22-May-2014 14:00:10
24-May-2014 12:00:18
25-May-2014 06:00:21
26-May-2014 12:00:26

01-Jun-2014 12:00:50
02-Jun-2014 12:00:54
03-Jun-2014 12:00:58
04-Jun-2014 12:01:02
05-Jun-2014 12:01:06
06-Jun-2014 12:01:10
07-Jun-2014 12:01:14
08-Jun-2014 03:31:17
09-Jun-2014 12:01:22
10-Jun-2014 07:31:26
11-Jun-2014 12:01:30
12-Jun-2014 08:31:34
13-Jun-2014 12:01:39
14-Jun-2014 12:01:43
15-Jun-2014 12:01:47
17-Jun-2014 01:31:53
18-Jun-2014 12:01:59
19-Jun-2014 12:02:03
20-Jun-2014 12:02:07
21-Jun-2014 22:32:13
22-Jun-2014 12:02:16
23-Jun-2014 12:02:20
24-Jun-2014 12:02:24
25-Jun-2014 12:02:28
26-Jun-2014 12:02:31
27-Jun-2014 12:02:35
28-Jun-2014 12:02:39
29-Jun-2014 12:02:43

01-Jul-2014 00:32:49
02-Jul-2014 12:02:55
03-Jul-2014 12:02:59
04-Jul-2014 12:03:03
05-Jul-2014 12:03:07
06-Jul-2014 12:03:11
07-Jul-2014 12:03:15
08-Jul-2014 12:03:19
09-Jul-2014 12:03:23
10-Jul-2014 08:03:26
11-Jul-2014 11:03:31
13-Jul-2014 15:03:39
15-Jul-2014 12:03:47
17-Jul-2014 12:03:55
18-Jul-2014 08:03:58
19-Jul-2014 02:34:01
20-Jul-2014 12:04:06
21-Jul-2014 12:04:10
22-Jul-2014 12:04:15
23-Jul-2014 12:04:18
24-Jul-2014 12:04:22
25-Jul-2014 12:04:26
26-Jul-2014 04:34:29
27-Jul-2014 22:04:36
28-Jul-2014 12:04:38
29-Jul-2014 12:04:42

01-Aug-2014 12:04:54
03-Aug-2014 12:05:02
04-Aug-2014 12:05:06
07-Aug-2014 12:05:18
08-Aug-2014 12:05:22
09-Aug-2014 12:05:26
10-Aug-2014 12:05:30
11-Aug-2014 12:05:34
12-Aug-2014 18:35:39
13-Aug-2014 12:05:42
14-Aug-2014 12:05:45
15-Aug-2014 12:05:49
16-Aug-2014 12:05:53
17-Aug-2014 12:05:57
18-Aug-2014 12:06:01
19-Aug-2014 12:06:05
20-Aug-2014 12:06:09
21-Aug-2014 12:06:13
22-Aug-2014 02:36:15
23-Aug-2014 12:06:21
24-Aug-2014 12:06:25
25-Aug-2014 12:06:29
26-Aug-2014 12:06:33
27-Aug-2014 12:06:37
28-Aug-2014 22:06:42
29-Aug-2014 10:36:44
30-Aug-2014 12:06:48

01-Sep-2014 12:06:56
02-Sep-2014 12:07:00
03-Sep-2014 12:07:04
04-Sep-2014 12:07:08
05-Sep-2014 12:07:12
06-Sep-2014 14:37:16
07-Sep-2014 12:07:19
08-Sep-2014 21:07:25
09-Sep-2014 12:07:27
10-Sep-2014 12:07:31
11-Sep-2014 12:07:35
12-Sep-2014 12:07:39

Dates for TerraSAR-x imagery

Track 005	Track 013
20140502_20140513	20140509_20140531
20140513_20140524	20140531_20140611
20140524_20140604	20140611_20140622
20140604_20140615	20140622_20140703
20140615_20140626	20140703_20140714
20140626_20140707	20140714_20140725
20140707_20140718	20140725_20140805
20140718_20140729	20140805_20140816
20140729_20140809	20140816_20140827
20140809_20140820	20140827_20140907
20140820_20140831	20140831_20140911

Appendix 7 Acronyms

CASS	Calving and Surging Glaciers in Svalbard (workshop)
CRIOS	Calving Rates and Impact On Sea Level (project)
DEM	Digital Elevation Model
GCP	Ground Control Points
GPS	Global Positioning System
IGS	International Glaciological society
ImGRAFT	Image georectification and feature tracking toolbox
IPCC	Intergovernmental panel on climate change
LEFM	Linear Elastic Fracture Mechanics
NCC	Normalized Cross Correlation (similarity algorithm)
NPI	Norwegian Polar Institute
NRK	Norsk rikskringkasting AS
PC	Phase Correlation (similarity algorithm)
RGB	red green blue
RMSE	root-mean-square-error
SLR	Single lens reflector (camera)
SAR	Synthetic Aperture Radar
UAV	Unmanned aerial vehicle
UNIS	University Centre in Svalbard
UTM	Universal Transverse Mercator (map projection)